TAMPEREEN TEKNILLINEN YLIOPISTO
TAMPERE UNIVERSITY OF TECHNOLOGY

Diego Torres Lobera

Modeling and Analysis of the Operation of PV Power Generators under Varying Atmospheric Conditions

Julkaisu 1248 • Publication 1248

Tampere 2014

Tampereen teknillinen yliopisto. Julkaisu 1248
Tampere University of Technology. Publication 1248

Diego Torres Lobera

Modeling and Analysis of the Operation of PV Power Generators under Varying Atmospheric Conditions

Thesis for the degree of Doctor of Science in Technology to be presented with due permission for public examination and criticism in Tietotalo Building, Auditorium TB109, at Tampere University of Technology, on the 17th of October 2014, at 12 noon.

Tampereen teknillinen yliopisto - Tampere University of Technology
Tampere 2014

ISBN 978-952-15-3366-2 (printed)
ISBN 978-952-15-3382-2 (PDF)
ISSN 1459-2045

ABSTRACT

Photovoltaic (PV) technology permits us to harness and transform solar radiation into electricity. However, PV power generators are still a minor share in the global power generation capacity. One of the main reasons for it is that PV systems are greatly dependent on the atmospheric conditions affecting their operation. Furthermore, series connection of PV cells is prone to power losses when the electrical characteristics of the cells are dissimilar or the cells operate under non-uniform operating conditions. Especially during changing atmospheric conditions, the operation and control of PV generators is complicated and there is a demand for improvement since today's inverters do not reach their best performance.

In this thesis, a state of the art inclusive thermal and electric simulation model of PV generators is proposed and validated with data measured at the Tampere University of Technology (TUT) solar PV power station research plant. The dynamic thermal and electric behaviors of the PV modules are first modelled separately theoretically based on previous authors' work. Subsequently, these models are further improved by analyzing module temperature measurements and the electric behavior of the PV modules operating under varying meteorological conditions. All the relevant climatic and site specific parameters, heat transfer mechanisms and parasitic resistive effects are considered without major simplifications to obtain the highest possible accuracy. Finally, the separate thermal and electric models are integrated and the result is a comprehensive simulation model that predicts the thermal and electric performance of PV generators operating under varying atmospheric conditions. This simulation model is intended, among other things, to assist in the inverter design and development of maximum power point (MPP) tracking algorithms, especially to improve their efficiency and operation under non-ideal and fast changing environmental conditions.

Partial shading affects the electrical characteristics of PV generators, causing them to operate away from their MPP and thus complicating the task to reach the maximum power production. This task is normally carried out by the power electronic converters interfacing the PV generators. Furthermore, partial shading conditions generally cause mismatch losses too. In this thesis, a method to generate a spatial irradiance map from a set of irradiance measurements is proposed and utilized to analyze the effect of moving clouds on the mismatch losses on several PV generator configurations and layouts. The mismatch losses are studied for several sizes of generators in which both series and parallel connection of PV modules are considered. The results indicate that the mismatch power losses caused by non-uniform operating conditions due to moving clouds can be reduced by locating PV modules of the generator as close to each other as possible. Furthermore, parallel connection of PV modules should be favored with respect to series connection.

PREFACE

The research and experimental work for this thesis were performed at the Department of Electrical Engineering (DEE) at Tampere University of Technology (TUT) during the years 2011-2014. The main contributors to the funding of the research were TUT and ABB Ltd. Additional financial support was provided by Fortum, Ulla Tuominen and Walter Ählström Foundations in the form of personal grants, deserving my special thanks.

I want to express my gratitude to Prof. Seppo Valkealahti to whom I thank for supervising my thesis and providing guidance throughout my academic career as a researcher. Moreover, I want to thank Prof. Teuvo Suntio who helped and encouraged me towards a faster completion of the doctoral degree. I also want to thank my colleagues and members of our former research group, Dr. Tech. Anssi Mäki, Dr. Tech. Jari Leppäaho, Dr. Tech. Juha Huusari, Dr. Tech. Joonas Puukko, Dr. Tech. Lari Nousianen, M. Sc. Tuomas Messo, M. Sc. Juha Jokipii, M. Sc. Kari Lappalainen and M. Sc. Jukka Viinamäki for providing professional support as well as creating an exceptional working atmosphere and making me feel like at home during these years.

I am grateful to Prof. Christopher Underwood and Prof. William Gerard Hurley for examining my thesis and their constructive comments that helped me to improve the quality of this manuscript. Further, I would like to thank Merja Teimonen and Terhi Salminen for providing valuable assistance regarding practical matters of the everyday work. The rest of the staff of the DEE also deserves my thanks for various sport activities and creating a good atmosphere at the department during these years.

I specially thank my parents Amparo and Ricardo and my brother Jorge for all their support, encouragement and patience throughout my academic career. Also, I am grateful to the rest of my family and my closest friends who showed me their support in every trip home. Finally, I want to thank my dear Núria for her love and support during these years.

Barcelona, August 2014

Diego Torres Lobera

TABLE OF CONTENTS

LIST OF SYMBOLS AND ABBREVIATIONS

ABBREVIATIONS

AC	Alternative current
CC	Constant current
CdTe	Cadmiun telluride
CIGS	Copper indium gallium diselenide
CO_2	Carbon dioxide
CV	Constant voltage
DC	Direct current
EU	European Union
EVA	Ethylene vinyl acetate
IGBT	Insulated gate bipolar transistor
LH	Long-horizontal (layout)
LV	Long-vertical (layout)
MPP	Maximum power point
MPPT	Maximum power point tracking
NREL	National Renewable Energy Laboratory
NOCT	Nominal operating cell temperature
NRMSE	Normalized root mean square error
NSC	Normalized sensitivity coefficient
p.u.	Per unit value
PV	Photovoltaic
PWM	Pulse width modulation
RMSE	Root mean square error
Si	Silicon
STC	Standard test conditions
SH	Short-horitzontal (layout)
SV	Short-vertical (layout)
TPES	Total primary energy source
TUT	Tampere University of Technology
USA	United States of America
WMO	World Meteorological Organization

GREEK CHARACTERS

α	Absorptivity
β	Tilt angle of the PV module

ΔG	Increment of irradiance
ΔP	Increment of power
ΔT	Temperature difference
ΔX	Increment of parameter X
ε	Emissivity
$\varepsilon_{\text{back}}$	Emissivity of the back of the PV module
$\varepsilon_{\text{front}}$	Emissivity of the front of the PV module
λ	Wavelength
ρ	Density
σ	Stefan-Boltzmann constant
τ	Time step

LATIN CHARACTERS

a	Diode ideality factor
a_{r}	Roof absorptivity coefficient
A	Area of the PV module
c	Speed of light
C_{mod}	Heat capacity of the PV module
C_{p}	Specific heat
E	Energy
E_{g}	Band gap energy
F_{br}	View factor from the back to the roof
F_{bs}	View factor from the back to the sky
F_{fr}	View factor from the front to the roof
F_{fs}	View factor from the front to the sky
G	Irradiance
G_{d}	Diffuse incoming solar radiation on a horizontal plane
G_{h}	Total incoming solar radiation on a horizontal plane
G_{max}	Maximum irradiance
Gr_{L}	Grashof number
h	Planck's constant
h_{conv}	Convection heat transfer coefficient
h_{forced}	Forced convection heat transfer coefficient
h_{free}	Free convection heat transfer coefficient
H	Height of the PV module
I	Current
I_{ph}	Photocurrent, i.e. current generated via photovoltaic effect
I_{o}	Dark saturation current of the PV cell or module
I_{o1}	Dark saturation current in the quasi-neutral regions

I_{o2}	Dark saturation current in the depletion region
I_{SC}	Short-circuit current
k	Boltzmann constant
k_d	Fraction of diffuse radiation
k_t	Thermal conductivity
K_i	Temperature coefficient of the short-circuit current
K_v	Temperature coefficient of the open-circuit voltage
L	Characteristic length
ML	Mismatch losses
N_s	Number of series-connected PV cells in a module
$NRMSE_P$	NRMSE between the measured and simulated P-V curves
NSC_P	Normalized sensitivity coefficient for power
Nu_{conv}	Nusselt number for convection
Nu_{forced}	Nusselt number for forced convection
Nu_{free}	Nusselt number for free convection
P	Power
P_m	Measured P-V characteristic of a PV generator
P_{max}	Maximum power in the measured P-V characteristic
P_s	Simulated P-V characteristic of a PV generator
Pr	Prandtl number
q	Elementary charge
q_{conv}	Heat loss due to convection
q_{in}	Incoming shortwave solar radiation
q_{loss}	Heat transfer losses
q_{lw}	Heat loss due to long-wave radiation
$q_{lw,back}$	Heat flux from the back of the PV module
$q_{lw,front}$	Heat flux from the front of the PV module
R_s	Internal series resistance of a photovoltaic generator
R_{sh}	Internal shunt resistance of a photovoltaic generator
Ra_L	Rayleigh number
Re	Reynolds number
$RMSE_T$	RMSE between the measured and simulated module temperatures
$RMSE_P$	RMSE between the measured and simulated P-V curve
SS	Shading strength
T	Temperature of the PV cell
T_{air}	Air temperature
T_{film}	Film temperature
T_m	Measured temperature of the PV module
T_{mod}	Temperature of the PV module
T_s	Simulated temperature of the PV module

T_{sky}	Sky temperature
T_{roof}	Roof temperature
v	Kinematic viscosity
v_{w}	Wind speed
V	Voltage
V_{OC}	Open-circuit voltage
V_{t}	Thermal voltage
w_{a}	Wind speed adjustment coefficient
W	Width of the PV module

1 INTRODUCTION

The social and economic development of the human society has been historically bound to the exploitation of the energy sources available. Nowadays, our consumer society depends strongly on the energy supply, requiring a reliable and continuous supply of it to satisfy the current welfare and standard of living (Mattick et al., 2010). According to the International Energy Agency (2013), the world total energy consumption was roughly 103800 TWh in 2011 which is approximately twice the energy that was consumed in 1973. This gives an idea of the growth experienced during the last decades and the outlooks indicate that the energy consumption will continue to increase in the foreknown future (U.S. Energy Information Administration, 2013).

Since the industrialization, the main sources of energy have been the fossil fuels in the form of coal, oil and gas. However, there are limited supplies of fossil fuels on our planet and their utilization generates environmental pollution and global warming as it is widely recognized (Bose, 2010). The overall conclusion of the International Panel of Climate Change (2013) is the following: "Warming of the climate system is unequivocal, and since the 1950s, many of the observed changes are unprecedented over decades to millennia. The atmosphere and ocean have warmed, the amounts of snow and ice have diminished, sea level has risen, and the concentrations of greenhouse gases have increased." Therefore, the only viable future is based on a revolution of the current energy usage and power production shifting to a paradigm of usage of only renewable energy sources in a sustainable way. The aggressive research in renewable energy sources and the solid increase in wind and solar photovoltaic power production capacity during the last decade witness that this process is already ongoing (Barroso et al., 2010; Renewable Energy Policy Network for the 21st Century, 2013).

Renewable energy sources encompass hydropower, biofuels, geothermal, wind and solar energies of which biofuels, wind and solar power are directly originated from the energy received from the Sun. According to the Renewable Energy Policy Network for the 21st Century (2013), renewable energy sources already "play a major role in the energy mix" in many countries around the globe as the price of their technologies continues to fall. Furthermore, investments in renewable energy expanded significantly in many developing countries in 2012 which had a positive effect on the installed capacity despite of the decrease in the global investment with respect to 2011. The solar and wind power

stand out amongst the rest of the renewable energy sources as their annual growth rates of installed capacity worldwide have been over 30 % on average during the decade 2000-2010 (Frost & Sullivan, 2009). According to World Energy Council (2013), the total capacities of wind power and solar PV were 238.1 GW and 68.9 GW in 2011. In 2012, capacities of approximately 12 GW of wind power in the EU and 31 GW of solar PV power worldwide were installed (European Photovoltaic Industry Association, 2013; European Wind Energy Association, 2013).

Solar energy reaches our planet vastly, in form of electromagnetic radiation emitted by the Sun, sustaining life and driving Earth's climate. The total amount of solar power reaching Earth's surface, i.e., available for solar collectors, is roughly 85000 TW (Mendoza, 2005) which represents over 7000 times the world's energy consumption of approximately 12 TW. As Thomas Edison stated in 1931, "I'd put my money on the sun and solar energy. What a source of power!" (Newton, 1989). Furthermore, the rest of the renewable energy sources make up less than 1 % of the available solar power (Abbott, 2010). It can be stated that the solar energy is the key energy source for the future and the efforts of humankind need to be focused on it.

Photovoltaic (PV) solar technology converts solar radiation into electricity in accordance with the photovoltaic effect. This phenomenon was first observed by the physicist Alexandre-Edmond Becquerel in 1839 and later explained by Albert Einstein in 1905. Over a century later, in 2012, the cumulated installed PV capacity was 102 GW comprising 1.8 % of the global power production capacity according to National Renewable Energy Laboratory (2012). The solar PV share of the total power production capacity experienced an increase of 1.5 % during the past three years. At this rate, PV will cover 10 % of the global power production capacity before 2030 which agrees with the most recent forecasts of the International Energy Agency on renewable energy market trends and projections. In fact, PV solar is already the leading technology regarding the installed new power production capacity in the European Union with a share of 46 % in 2012 (European Photovoltaic Industry Association, 2013).

A substantial increase of PV solar power generators has taken place in recent years as a result of the improvement in the conversion efficiency of the PV technology and its manufacturing techniques. This has reduced the price of PV systems and made them more attractive (Barroso et al., 2010). PV generators are composed of PV modules connected in series and parallel to achieve the power levels required (Häberlin, 2012). PV modules are, in turn, normally composed of series connected PV cells. Nowadays, most of the installed PV generators are designed as grid-connected systems and utilize power inverters as interfaces between the generator and the grid (Eltawil and Zhao, 2010). Solar inverters play a central role in the PV systems by converting the DC power produced by the PV modules to AC power for the electrical grid (Teodorescu et al., 2011). There are

several PV generator topologies for grid connected systems based on different inverter concepts developed during the last decades as will be reviewed in Chapter 2.

Despite of the large new PV power capacity installed during the last years, the key barrier against high PV penetration is the large variability of the output power (Bosch et al., 2013). PV systems are greatly dependent on the atmospheric conditions affecting their operation. Furthermore, series connection of PV cells is prone to power losses when the electrical characteristics of the cells are dissimilar or the cells operate under non-uniform operating conditions (Alonso-García et al., 2006; Chamberlin et al., 1995). These losses can additionally lead to irreversible damage of the cells by hot spotting. Especially during changing atmospheric conditions, the operation and control of PV generators is complicated and there is a demand for improvement since today's inverters do not reach their best performance. There is extensive literature on the modeling of PV cells and modules but not many authors have approached the complex topic of model PV generators operating under real changing conditions and inclusively analyzed the dynamic thermal and electric behavior of PV modules.

Partial shading conditions, regarding PV power generators, are a particular case of non-uniform operating conditions in which the PV cells and modules composing the generator operate under different solar radiation levels (and generally different cell temperatures as well) due to the shading caused by objects. These objects can be either static, e.g., trees, building structures, other PV modules, snow, dust, etc., or dynamic, e.g., moving clouds. The effects of partial shading on the operation of PV generators have been shown to cause major power losses and to decrease their efficiency considerably (Mäki, 2013). Partial shading affects the electrical characteristics of PV systems and may cause the PV generators to operate away from their maximum power points (MPP). The maximum power point tracking (MPPT) is generally carried out by the power electronic systems interfacing the PV generators, most likely by the inverter. Therefore, an additional problem inherent to the operation of PV systems under partial shading conditions is that they may lead to reliability issues of the power electronic converters caused by a malfunction of the MPPT algorithm (Petrone et al., 2008).

The main aim of this thesis is to develop, implement and evaluate the performance of a state of the art inclusive thermal and electric simulation model for the TUT Solar PV Power Station Research Plant which is accurate enough for research purposes. Additionally, the objective of this thesis is to analyze the effects of partial shading on PV generators.

1.1 Objectives and Scientific Contribution

The main objective of this thesis is to develop an integrated thermal and electric simulation model to analyze the operation of PV systems operating under varying atmospheric

conditions. To achieve this, a necessary system to analyze the operation of PV generators needs to be designed and built first. Subsequently, the dynamic thermal and electric models of a PV module will be considered theoretically and then implemented and developed further by analyzing temperature and power measurements. Finally, both models can be integrated together into a comprehensive simulation model to predict the instantaneous I-V characteristics and operating temperatures of PV modules and strings based on atmospheric measurements.

An additional objective of this thesis is to develop an irradiance map generation tool and utilize a systematic approach to study the effects of partial shading conditions caused by dynamic objects, i.e., moving clouds, on PV generators. These effects comprise the appearance of mismatch losses and multiple maximum power points in the P-V curve of PV generators. In this thesis, the effect of partial shading conditions caused by moving clouds on mismatch losses in case of several different PV power generator sizes and configurations are studied.

This thesis attempts to reach the above-mentioned objectives by implementing the simulation models in Matlab and Simulink software. The models take into account the most important parameters and heat transfer processes affecting the PV modules without major simplifications and include site-specific parameters required to improve the accuracy of the models. The measurement systems designed in this thesis consist of the atmospheric and electric measurement systems as well as the data-acquisition and storage systems needed to register the operating conditions affecting the performance of the PV modules of TUT solar photovoltaic power station research plant. The sampling frequency of these systems is required to be high enough to detect even the fastest phenomena related to power generation with PV power plants.

The main scientific contributions of this thesis can be summarized as follows:

- Design and implementation of the measurement systems required to analyze the thermal and electrical characteristics of PV modules with a fast enough sampling frequency.

- Comprehension of the dynamic thermal and electric behavior of PV modules and module strings operating under non-ideal varying operating conditions.

- Development and verification of a state of the art inclusive dynamic thermal and electric simulation model for PV modules and strings.

- Comprehension of the effects of partial shading conditions and the mismatch losses caused by moving clouds in different PV power generator areas and configurations.

1.2 Structure of the Thesis

The rest of the thesis is organized as follows. The background of grid connected solar photovoltaic generators is provided in Chapter 2. A brief introduction to renewable energy sources and solar energy will be reviewed. The main characteristics and history of photovoltaic electricity will be presented jointly with the fundamental operation of PV generators and the effects of the most important operating conditions on their performance. Finally, the different possible electrical configurations of grid connected PV generators will be discussed.

Chapter 3 familiarizes the reader with the facilities and measurement equipments of TUT solar PV power station research plant installed at Tampere University of Technology. The layout of the PV facility, the measurement, data-acquisition and database systems will be overviewed and their design specifications justified.

Chapter 4 guides the reader through the theory behind the modeling of PV modules. The first part of Chapter 4 presents a dynamic state of the art thermal model of PV modules which considers the thermal mass of the module in addition to all relevant climatic and site-specific conditions and heat transfer mechanisms. The second part of Chapter 4 presents the electric simulation model. This model is based on the well-known one-diode model which considers the parasitic effects of the series and shunt resistances and includes the effects of the protection bypass diodes so that the simulation of series-connected PV modules can be easily implemented.

Chapter 5 includes the experimental verification of the proposed dynamic thermal, electrical and integrated simulation models. The thermal model will be adapted and further developed from the previous work of other authors in the first part of Chapter 5. The accuracy of the simulation model will be tested with the measured data for ninety-one consecutive days during summer 2012. In the second part of Chapter 5, the electric model will be implemented and its operation will be assessed by the deviation between the measured and simulated P-V curves. The model will be further developed improving its accuracy during operation at low irradiance conditions through a sensitivity analysis of the parameters of the model. Finally, the electric simulation model will be tested under static operating conditions for a single PV module and a PV string of six series-connected modules. In the third part of Chapter 5, the operation of the integrated simulation model will be implemented, tested and validated with climatic and I-V curve measurements conducted in the TUT solar PV power station research plant.

A method to generate a spatial irradiance map from a set of seventeen irradiance measurements by using the natural neighbor interpolation method is proposed in Chapter 6. This method will be used to analyze the effect of partial shading caused by moving clouds on the irradiance conditions and mismatch losses on several PV generator configurations and layouts.

Finally, the main conclusions of this thesis are presented in Chapter 7 jointly with recommendations for further research.

2 BACKGROUND OF THE THESIS

This Chapter introduces the background of the research topics discussed in this thesis on a general level and clarifies the motivation for the conducted research to the reader. Firstly, a brief introduction to the renewable energy sources and solar energy in the energy production framework is given. Subsequently, the main characteristics and history of photovoltaic (PV) electricity are presented jointly with the fundamental operation of PV generators and the effects of the most important operating conditions on their performance. Finally, the different possible electrical configurations of grid connected PV generators are discussed.

2.1 Renewable Energy Sources and Solar Energy

The global energy consumption has increased beyond any possible forecast since the Industrial Revolution during the last two and a half centuries and the growth seems to continue in the foreknown future. Initially, industrialization led to the usage of coal as the primary source for generating energy in the 18^{th} century. Afterwards, coal use was surpassed by oil at the beginning of the 19^{th} century motivated by the invention and expansion of the internal combustion engine. Nowadays the fossil fuels are still the main energy source of the worldwide economy. In 2010, 87 % of total energy consumed was generated from fossil fuels, 7 % was coming from renewable energies and 6 % from nuclear plants (Bose, 2010).

Unfortunately, as it is widely known, the usage of fossil fuels shall not be a permanent solution for mankind due to the limited supplies of fossil energy sources on our planet. On top of that, a major concern has grown in the last decades regarding the environmental pollution and climate change due to CO_2 emissions. These issues have led to a genuine interest in the utilization of alternative abundant, cheaper and cleaner energy sources: the renewables (Bose, 2010; Liserre and Sauter, 2010; Valkealahti, 2011). Once they are implemented, the usage of renewable energy sources generates little or zero emissions of the aforementioned CO_2 gases (Bull, 2001).

Renewable energy sources are conventionally considered to include biofuels, wind power, geothermal energy, hydropower and solar energy. To date, biofuels are the most utilized renewable energy source covering a 10 % of the world total primary energy supply (TPES) in 2011 (International Energy Agency, 2013). Hydropower, the second

largest renewable energy source nowadays, covered a 2.3 % of the world TPES in 2011. Harnessing large amounts of water by building dams is a well-established and commonly adopted method worldwide to generate electricity (Abbott, 2010). In 2012, hydropower production rose to 990 GW (Renewable Energy Policy Network for the 21st Century, 2013). Wind and solar energies have constantly shown increasing growth rates in the last years. The capacity of wind power is widely known and has been subject of major investments. In 2012, 11985 MW of wind power was installed in the European Union which represents a 26.5 % of the new power production capacity installations, the second biggest share after solar PV (European Wind Energy Association, 2013). Solar PV is the fastest growing renewable energy source at the moment with over 40 % of annual increase in the installed capacity during the decade of the 2000s (Barroso et al., 2010; Kroposki and Margolis, 2009). Furthermore, according to European Photovoltaic Industry Association (2013), 2011 and 2012 witnessed record growths of solar PV installed capacity with 30.4 and 31.1 GW respectively.

From mankind's point of view, the Sun is an endless source of energy whose power on the surface of the Earth can be forecasted depending on the location on the planet and the relative position between the Earth and the Sun, i.e., the time of year. It is estimated that in less than an hour, Earth receives the amount of energy from the Sun that mankind consumes in one year (Kroposki and Margolis, 2009). Abbott (2010) remarks that it is vital to adopt dominant focus on research and investment in solar energy since the competing renewable energy sources produce less than 1 % of what is achievable with solar. However, Abbott (2010) observes that the medium-term future of energy production will consist of an amalgam of existing technologies with increasing shares of renewable energies. Valkealahti (2011) estimates that renewable energies, which already have a growing role in the energy sector currently, will carry a major relevance in the global energy generation by 2050.

The energy coming from the Sun is originated from the fusion reactions taking place in the core of the star and then carried away as electromagnetic radiation, i.e., photons through the space (Luque and Hegedus, 2011). When these photons arrive to the Earth's atmosphere, the irradiation is approximately the solar constant: 1361 W/m^2 (Gueymard, 2004; Kopp and Lean, 2011). The atmosphere reflects part of the incoming solar radiation back to space and absorbs and scatters part of the remaining photons traveling through it. As a result, the amount of solar radiation reaching the sea level on a plane perpendicular to the incoming solar radiation on a clear sky day is approximately 1000 W/m^2.

2.2 Characteristics of Photovoltaic Electricity

Solar technologies permit us to harness and transform solar energy into electricity or heat. Amongst them, solar photovoltaic (PV) energy is one of the most developed and

broadly implemented technologies. Its scientific foundation is the photovoltaic effect which describes the property of certain materials to generate free charge carriers, i.e. electrical current when exposed to electromagnetic radiation.

The history of PV goes back to the 19$^{\text{th}}$ century when, in 1839, the French physicist Alexandre-Edmond Becquerel discovered that certain materials were able to generate electrical current when exposed to light. The first functional PV device was manufactured in 1883 by Fritts (1883). Fritts noted that "the current, if not wanted immediately, can be either stored where produced, in storage batteries," ... "or transmitted a distance and there used," foreseeing today's PV technology and applications more than a hundred years ago. These findings stimulated Albert Einstein to explain this observed phenomenon during his "miraculous year" of 1905. In 1921 Einstein was awarded the Nobel Prize in Physics for his explanation of the photoelectric effect.

The photovoltaic effect is conveniently described using the energy band structure. PV devices are made of semiconductor materials which have weakly bonded electrons occupying a band of energy called valence band. These valence electrons cannot move within the material unless they receive enough energy to break their atomic bonds to move up into in a new energy band called the conduction band. Free electrons in the conduction band are separated from the valence band by the band gap energy (E_{G}). When single electrons move freely within the atomic structure, electrical current is observed on a larger scale, i.e., electricity flows through the material. Furthermore, when an electron is excited into the conduction band, the valence band is left with an empty vacancy generating a positive charge, i.e., a hole.

Photons are particles of electromagnetic radiation which contain a certain amount of energy

$$E = \frac{hc}{\lambda}, \tag{2.1}$$

where E is the energy of the photon, h the Planck's constant, c the speed of light and λ the wavelength of the photon. The amount of energy required to excite a valence electron to the conduction band depends on the band gap energy of the material.

Pure semiconductor materials are characterized by the recombination of their free electrons after a certain time. This means that the electrons lose their energy and return to the valence band resulting in the elimination of the electron-hole pair. This phenomenon motivates that, to be able to extract electrical energy from them, PV cells need to be made of two different types of semiconductors, one containing additional negative charges (n-type) and the other with extra positive charges (p-type). The union of these two types of semiconductor materials, known as pn-junction, is characterized by the generation of an electric field which separates the created electron-hole pairs and enables the

free electrons for the production of electrical energy. Around 1950, Shockley developed the theory of semiconductor pn-junctions and transistors (Shockley, 1949; Shockley et al., 1951) of which he was awarded, jointly with John Bardeen and Walter Houser Brattain, the Nobel Prize in Physics in 1956.

The modern era of PV started in 1954 when researchers at Bell Laboratories accidentally discovered that pn-junction diodes generated a potential difference when the artificial lights in the room were on. Within a year, they produced a silicon (Si) pn-junction solar cell with an efficiency of 6 % (Chapin et al., 1954). From the 1950s, the development of different types of PV cells and manufacturing processes rapidly translated into a vast improvement in the efficiency of single PV cells; but there is still room for improvement. According to Luque and Hegedus (2011), the theoretical limit for single-junction Si PV cells is approximately 48 % while nowadays their efficiency is around 20 to 25 %. Moreover, Silicon, one of the most abundant materials on our planet, is the semiconductor material used for 90 % of the PV applications today (Kroposki and Margolis, 2009). However, other types of PV cells have been developed too, such as thin-film cadmium telluride (CdTe) or copper indium gallium diselenide (CIGS) cells which commonly have lower efficiencies than Si cells. Multijunction PV cells are able to absorb a bigger part of the spectrum of solar radiation compared to conventional single-junction cells and, therefore, achieve better efficiencies (Wenham and Green, 1996). Some emerging technologies must also be noted such as dye-sensitized and organic cells with confirmed cell efficiencies of 11.9 % and 10.7 %, respectively (Green et al., 2013).

The evolution of the cell efficiencies according to the National Renewable Energy Laboratory (2013) is shown in Figure 2.1. Even though the efficiency of some PV cell technologies have not increased during the last decades, indicating that their development may have reached an efficiency limit, multijunction and organic PV cells appear to have room for development in the future. The highest efficiencies reported in 2013 are 37.8 % and 44 % for multijunction cells operating under non-concentrated and concentrated solar radiation, respectively. From the economical perspective, the cell types shown in Figure 2.1 can be classified into two main groups which aim to reduce the cost of the produced power by two different approaches. The first group includes monocrystalline silicon cells, multijunction cells and cells operating under concentrated illumination. These technologies focus on high operational efficiencies achieved with complex structural solutions that result in high manufacturing costs. The second group gathers multicrystalline and amorphous silicon cells, thin-film cells and the previously mentioned emerging technologies which try to minimize the manufacturing costs resulting in lower cell efficiencies.

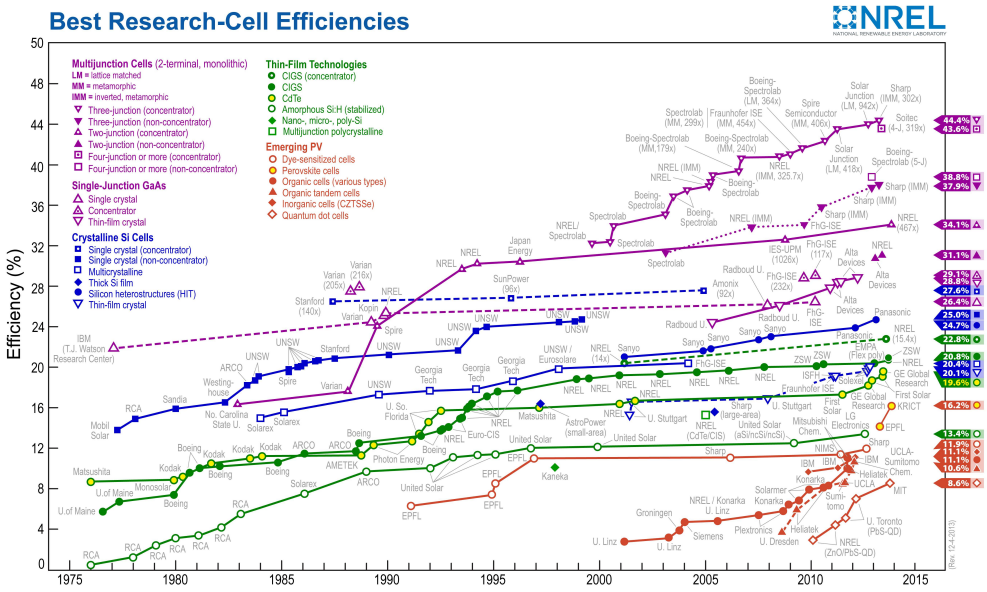

Figure 2.1: Development of the solar cell technologies according to National Renewable Energy Laboratory (2013).

2.3 Photovoltaic Cells and Modules

Essentially all PV cells present similar electrical characteristics regardless of their specific manufacturing technology. Therefore, a general electric model, i.e., a mathematical expression that models the electrical behavior of a PV cell can be derived based on the extensive knowledge of semiconductor physics. The general expression for the current of an ideal PV cell can be formed according to Equation 2.2, where, V is the voltage, k is the Boltzmann constant, q is the elementary charge, T is the cell temperature, I_{o1} and I_{o2} are the dark saturation currents due to recombination in the quasi-neutral regions and in the depletion region of the pn-junction, respectively, and I_{ph} is the photocurrent which describes the fundamental source of the produced power due to generation of charge carriers by the photovoltaic effect (Luque and Hegedus, 2011).

$$I = I_{ph} - I_{o1}\left[exp\left(\frac{qV}{kT}\right) - 1\right] - I_{o2}\left[exp\left(\frac{qV}{2kT}\right) - 1\right], \tag{2.2}$$

Equation 2.2, however, neglects the internal semiconductor junction parasitic effects typically associated with real PV cells: the series and shunt resistances. The series resistance (R_s) is included to consider the losses introduced by the physical connections

of the cell, whereas the shunt resistance (R_{sh}) tries to model the losses produced by atomic non-idealities of the structure of the cell (Messenger and Ventre, 2003). The electrical model of a complete real PV cell is illustrated in Figure 2.2 including the effect of the parasitic resistances. Adding these to Equation 2.2 results into

$$I = I_{\mathrm{ph}} - I_{\mathrm{o1}}\left[exp\left(\frac{V + IR_{\mathrm{s}}}{\frac{kT}{q}}\right) - 1\right] - I_{\mathrm{o2}}\left[exp\left(\frac{V + IR_{\mathrm{s}}}{2\frac{kT}{q}}\right) - 1\right] - \frac{V + IR_{\mathrm{s}}}{R_{\mathrm{sh}}}. \quad (2.3)$$

This model is widely used in the literature (Chamberlin et al., 1995; Galiana et al., 2008; Gow and Manning, 1999; Sandrolini et al., 2010; Silvestre et al., 2009).

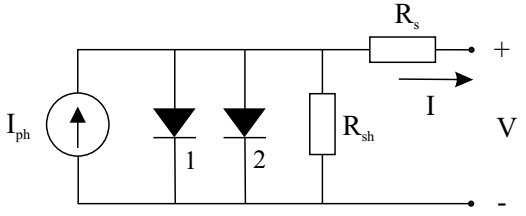

Figure 2.2: Electrical equivalent circuit of a two-diode-based model of a PV cell.

However, the dark saturation currents are given by rather complex expressions that depend on the solar cell structure, material properties, and the operating conditions (Luque and Hegedus, 2011). This motivates Equation 2.3 to be simplified by combining the effects of both diodes into a single diode with an ideality factor a yielding

$$I = I_{\mathrm{ph}} - I_{\mathrm{o}}\left[exp\left(\frac{V + IR_{\mathrm{s}}}{a\frac{kT}{q}}\right) - 1\right] - \frac{V + IR_{\mathrm{s}}}{R_{\mathrm{sh}}}, \quad (2.4)$$

where I_{o} is the dark saturation current of the PV cell. The ideality factor typically has a value between 1 and 2 and depends on the materials comprising the pn-junction. This one-diode model is extensively used in the literature (Liu and Dougal, 2002; Lo Brano et al., 2010; Nema et al., 2009; Nousiainen et al., 2013; Villalva et al., 2009b).

Equation 2.4 is a non-lineal implicit equation that requires numerical computation methods to find the values for the cell current and voltage at a certain operating point. By doing it, the characteristic current-voltage (I-V) curve can be obtained as shown in Figure 2.3. In it, the cell current-voltage and power-voltage characteristics are represented using per units values. The voltage, current and power base values utilized to calculate the per unit values correspond to the maximum power point (MPP) voltage, current and power of the cell operating under Standard Test Conditions (STC), i.e., incident irradiance of 1000 W/m^2 and cell temperature of 25 °C. It can be observed that the generated power

reaches its maximum for a specific voltage and current, also known as maximum power point voltage and current. Furthermore, this MPP point which is the aimed operating point regarding energy production purposes, acts as the border point between two distinct defined regions: the constant current (CC) and the constant voltage (CV) regions. At the CC region, located at lower voltages than the MPP voltage, the current remains almost constant regardless of changes of the cell voltage, whereas at the CV region, for higher voltages than the MPP voltage, the voltage stays relatively constant regardless of current changes. According to Shmilovitz and Singer (2002), the PV cell can be considered to be a non-ideal current source with a limited output power.

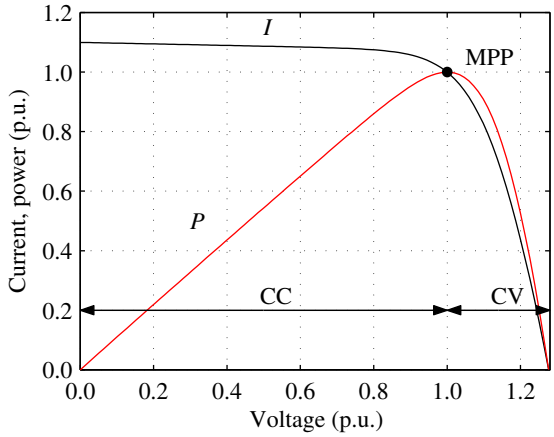

Figure 2.3: Current-voltage and power-voltage characteristics of a typical PV cell represented utilizing per unit values. The voltage, current and power base values utilized to calculate the per unit values correspond to the MPP voltage, current and power of the cell operating under STC.

The effects of the parasitic resistances on the I-V characteristic are shown in Figures 2.4 and 2.5. The series resistance has an effect on the voltage in the CV region, i.e, on the width of the CV region. Additionally, if series resistance is big enough, the short circuit current I_{SC} decreases with increasing R_{s}, whereas it has no effect on the open circuit voltage V_{OC}. On the contrary, the shunt resistance affects the current in the CC region and reduces the V_{OC}, whereas it has no effect on the I_{SC} as can be seen in Figure 2.5.

The typical electrical parameters of silicon PV cells are I_{SC} from 3 to 8 A and V_{OC} from 0.5 to 0.7 V. The I_{SC} depends principally on the physical area of the cell whereas the V_{OC} is dependent on the used material (Luque and Hegedus, 2011). The MPP voltage and current are typically found at the 80 % of the V_{OC} and 90 % of the I_{SC}, respectively (Esram and Chapman, 2007).

Electrical series connection of PV cells is commonly utilized to enable adequate power

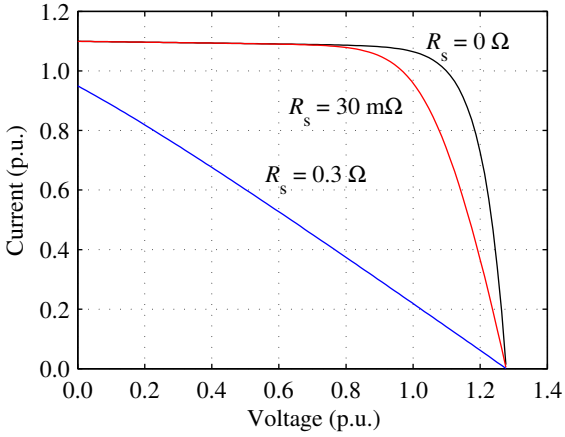

Figure 2.4: Effect of the series resistance on the I-V characteristic of a typical PV cell when R_{sh} is assumed to be infinite.

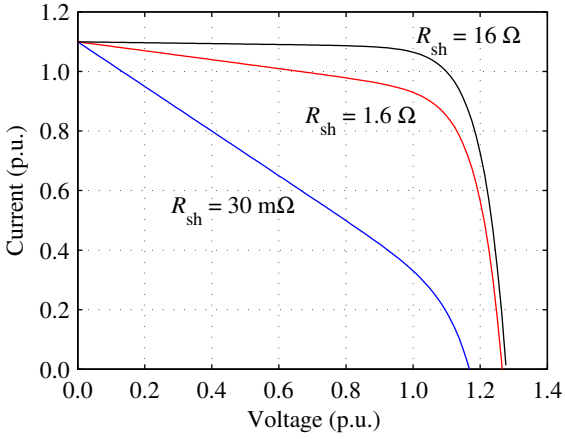

Figure 2.5: Effect of the shunt resistance on the I-V characteristic of a typical PV cell when R_{s} is assumed to be zero.

supply (Häberlin, 2012). By connecting the cells in series, the total output voltage results from adding up the voltages generated by each serparate cell which also implies an increase in the power produced. Series connected PV cells form PV modules that are the basic building blocks of any practical PV system regardless of its size. Commercial PV modules are typically composed of 30 to 60 cells with nominal MPP powers in the order of 80 W to 240 W.

The physical structure of typical PV modules comprises a series of layers that isolate and protect the cells from the environment in which they are used. These normally

include a front surface, an encapsulate for the cells, a rear surface and the frame of the module. For silicon based PV modules, the front surface material is typically tempered low iron glass with a high transmission of light. The encapsulate is used to provide adhesion between the solar cells and should be stable at elevated temperatures and high radiation exposure. The rear surface, normally made of Tedlar, must have low thermal resistance and the frame is usually made out of aluminum.

Furthermore, commercial PV modules usually include protection bypass diodes too. Due to the series connection, the total current flowing through the module is limited by the smallest current produced by any of the cells. This can happen due to several reasons such as difference between the electrical characteristics of the cells or shading of part of the cells, among others. Moreover, under such scenarios the limiting cells will become reverse biased and start acting as loads dissipating the extra power produced by the rest of the cells which may lead to irreversible damage by hot spotting (Lashway, 1988). To overcome this problem, PV modules are divided into segments and bypass diodes are connected in anti-parallel to the cells to protect each of the segments (Silvestre et al., 2009). Thus, if any cell is producing less current than other cells in a segment and the rest of the segments generate the nominal current, the difference between this nominal current and the current generated by the segment with limiting cell will be diverted into the corresponding bypass diode.

The optimal number of bypass diodes connected in a PV module has been studied by many authors (Silvestre et al., 2009; Ubisse and Sebitosi, 2009). The parameter defining the maximum number of cells per bypass diode is the breakdown voltage of the PV cells. Thus, no cell should operate at reverse bias with negative voltage close to the breakdown voltage.

2.4 Effect of the Environmental Conditions on the Operation of PV Cells

The environmental conditions have a significant influence on the operation of PV cells and modules. Their electrical performance is affected directly via incident solar radiation and indirectly via operating cell temperature which depends upon other factors such as ambient temperature, incident solar radiation, wind speed and direction, and the physical properties of the PV cell or module. The effect of irradiance on PV cells is illustrated in Figure 2.6. As can be observed, the short circuit current of the cell is proportional to the irradiance absorbed by the cells. Moreover, the level of irradiance also affects the open circuit voltage, but the effect is minor compared to the short circuit current. The reason for this is that the open circuit voltage is logarithmically dependent on the irradiance (Luque and Hegedus, 2011). Needless to say, any reduction in either I_{SC} or V_{OC} translates into a decrease in the power produced by PV cells.

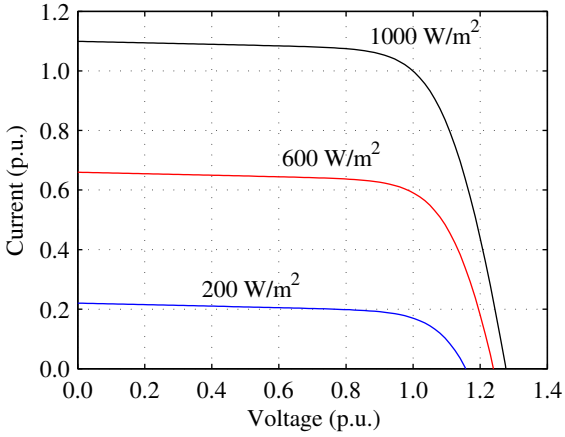

Figure 2.6: Effect of varying the incident irradiance on the I-V characteristic of a typical PV cell under different irradiances relative to STC conditions at 1000 W/m^2.

The operating temperature plays an important role in the PV energy conversion (Skoplaki and Palyvos, 2009). As can be seen in Figure 2.7, the open circuit voltage of the cell decreases with increasing temperature. This voltage drop is a consequence of the reduction of the band gap energy of the semiconductor materials when their temperature rises. For silicon PV cells the temperature coefficient is approximately -2.3 mV/°C (Wenham, 2007). Accordingly, higher cell voltages and, thereby, powers are obtained at low temperatures. On the contrary, the operating temperature has an increasing effect on the short circuit current. This effect is, however, minor compared to the voltage reduction as the short circuit current remains almost unaffected to changes in temperature (Figure 2.7).

As noted in Section 2.3, commercial PV modules typically comprise a number of series connected PV cells due to practical issues. However, series connection of PV cells is highly susceptible to power losses if the cells do not have identical properties, if they are not equally mounted or if the environmental operating conditions are non-identical for the complete group of PV cells (Alonso-García et al., 2006; Chamberlin et al., 1995). In other words, a PV generator operating at its own maximum power point forces its cells to operate at points different from their own individual MPP under such scenarios. Mismatch losses (ML) generally comprehend the power losses due to these causes. However, in this thesis ML are defined as the power losses in a PV power generator caused only by the mismatch operating conditions affecting to its interconnected cells, e.g., partial shading conditions.

Partial shading conditions refer to all conditions in which the cells of a PV generator receive non-uniform irradiance levels. These kinds of operating conditions can occur due

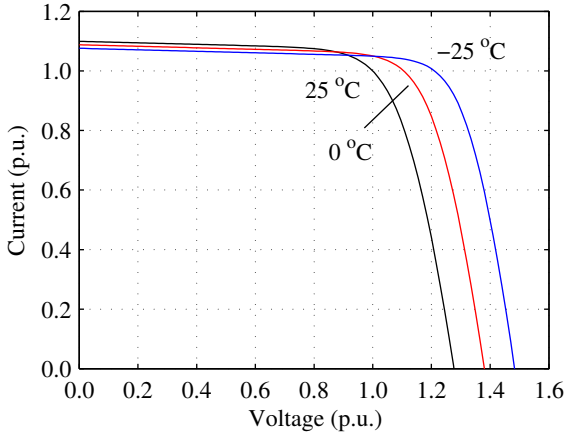

Figure 2.7: Effect of varying the cell temperature on the *I-V* characteristic of a typical PV cell under different operating temperatures relative to STC conditions at 25 °C.

to various reasons such as buildings, trees, clouds, etc. Shadings caused by static objects are characterized by their sharp shadow edges which advance gradually as the Earth spins around its axis. Shadows caused by clouds, in contrast, are random in shape and shading strength and move rapidly compared to the former. Furthermore, partial shading is one of the reasons why PV modules include bypass diodes as introduced in Section 2.3. However, bypass diodes indirectly shape the nominal *I-V* characteristics under partial shading conditions as analyzed in the following.

Under uniform irradiance conditions a PV module or system has a unique MPP, whereas under non-uniform conditions there can be as many MPPs as is the number of bypass diodes connected in the system. For instance, a system comprising three PV cells connected in series with a bypass diode protecting each of the cells and receiving three different levels of irradiance will present three local MPP points as illustrated in Figure 2.8. In this case, the global MPP occurs at approximately 60 % of the V_{OC} compared to the nominal 80 %, but there are cases and systems in which the MPP can be found at 25 % of the V_{OC} or less. The desired operating point from the power generation perspective is the global MPP, maximizing the generation of power. This is a challenge to MPP-tracking algorithms as the global MPP of PV generators is constantly changing due to varying environmental and partial shading conditions.

2.5 Photovoltaic Power Systems

Photovoltaic power generators are generally divided into two main groups: stand-alone and grid-connected PV systems. According to Kazmerski (2006), the vast majority of PV systems installed before 1990 were designed for stand-alone applications. However,

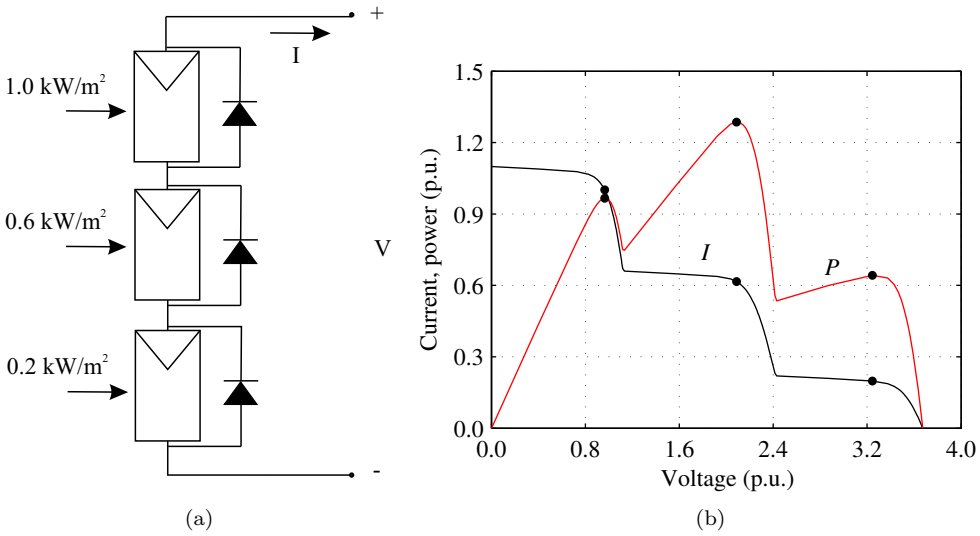

Figure 2.8: (a) A PV generator of three series connected PV cells protected with three bypass diodes and (b) electrical characteristics of the generator when each PV cell receives different irradiances. MPPs are marked with black dots.

this tendency has changed over the last 25 years and nowadays most of the installed PV power systems are designed as grid-connected systems (Eltawil and Zhao, 2010).

Stand-alone PV systems are characterized by operating independent of the electric utility grid. They are generally designed and sized to supply a certain amount of direct current (DC) or alternate current (AC) power to a load. Unless designed to operate only during times when the solar radiation is sufficient, in order to ensure the supply of power also during times with very low radiation or no radiation at all, e.g. during strong cloud cover conditions or at night time, stand-alone systems usually integrate energy storage systems. Moreover, stand-alone systems can be implemented with the PV generator as the only energy source or with auxiliary energy sources. These kinds of systems are the so-called hybrid systems and include complementary power production employing fossil fuels or other renewable energy sources.

Grid-connected PV systems are characterized by being connected to the electrical utility grid interfaced by a suitable inverter which transforms the DC power produced by the PV modules into AC that circulates through the electrical grid. These types of systems offer the possibility to generate significant amounts of electrical energy near the consumption point, thus reducing transmission and distribution losses. Grid-connected systems operate essentially in parallel with the existing electrical grids, allowing the exchange of electricity to and from the grid. Generally, small PV systems do not have important effects on the power quality of the grid, load on lines, etc. However, for a

larger share of PV in low-voltage grids, these aspects need to be taken into account. From the energy production perspective, grid-connected PV systems can be subdivided into decentralized and central grid-connected PV systems.

Decentralized grid-connected PV systems generally include generators with a small power range that are installed on top of buildings or integrated into building facades. Therefore, the energy produced at the PV generator can be used to e.g. power up the building appliances and any excess energy will be injected into the grid. In this case, the inverter must adapt the voltage to the grid level and synchronize with the frequency of the grid. Energy storage systems are not necessary since the building can be powered from the grid during periods without solar radiation to satisfy the power demand. Central grid-connected PV systems, in contrast to the former, have larger installed powers which can be up to the range of gigawatts. Such PV generators permit direct connection to medium or high voltage electrical grids. Central PV systems generally occupy large field areas but they can also be designed to be integrated in large buildings and factories.

Power inverters are an essential component of PV systems in which, as mentioned previously, their main function is to convert DC power into AC power. Furthermore, as interfacing devices in PV power systems, inverters also perform other important tasks such as maximum power point tracking (MPPT) and islanding detection in addition to safety and monitoring functions (Teodorescu et al., 2011). In grid-connected PV applications, particularly, various technological inverter concepts have been developed during the last decades from centralized inverters to AC-module technology as illustrated in Figure 2.9 (Kjaer et al., 2005).

The central inverter concept, widely utilized in the past, is characterized by having a single inverter interfacing a large number of PV modules (Figure 2.9(a)). The modules are first connected in series forming strings to reach high voltages so that further amplification is not required. The PV strings, protected with string diodes, are subsequently connected in parallel to achieve generators with high power levels. This type of system presents serious restrictions which penalize the mass production of energy. These restrictions are, e.g., the need of high-voltage DC cabling and non-flexible system design. Moreover, PV systems with central inverter concept experience power losses due to the centralized MPPT, mismatch losses between the numerous amount of PV modules and losses in the string diodes. The grid-connected stage of central inverters is normally implemented with thyristors which introduce high current harmonics and involve poor power quality (Kjaer et al., 2005).

The string inverter technology is a reduced version of the central inverter concept as can be seen in Figure 2.9(b). This approach, commonly utilized nowadays, consists of an inverter interfacing a single PV string to the grid. It requires a small amount of PV modules connected in series (roughly 16) to avoid further voltage amplification, but the

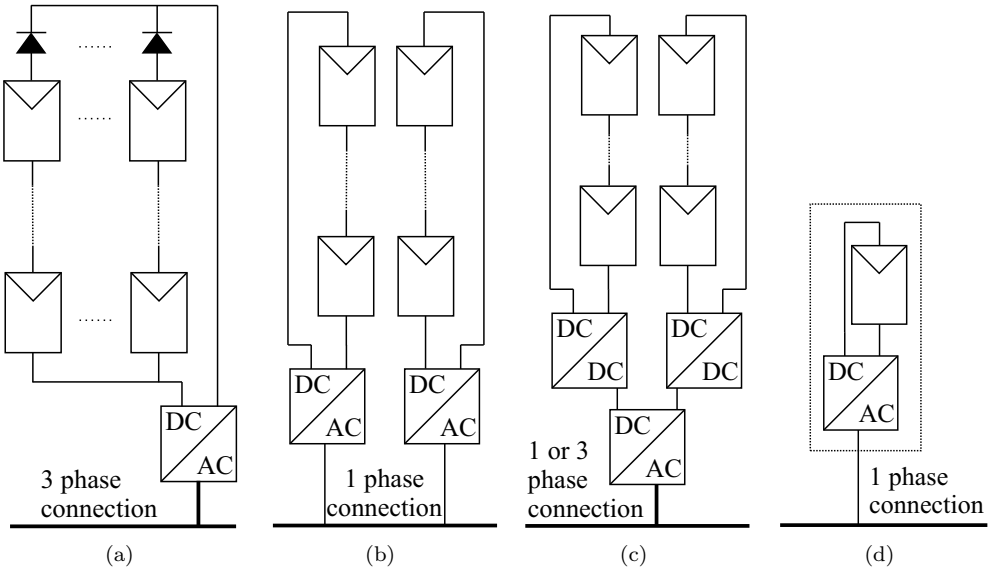

Figure 2.9: PV inverter concepts: (a) central inverter technology, (b) string inverter technology, (c) multi-string inverter technology and (d) AC-module technology.

possibility of using fewer modules exists if, e.g., a DC-DC converter is utilized. According to Kjaer et al. (2005), the power losses are reduced in string inverter technology since there are no losses associated with string diodes and a separated MPPT can be implemented to each string. This increases the overall efficiency compared to central inverter technology. In addition, string inverter-based systems are more modular and flexible which benefits mass production of energy if the systems are upgraded to higher power levels.

The multi-string inverter concept, depicted in Figure 2.9(c), results from further developing the string inverter technology. In this case, every PV string is interfaced with a DC-DC converter to a common larger inverter. This approach combines the benefits of both string and central inverter concepts as every string can be controlled individually by its DC-DC converter, while the power rating of the inverter is high with higher efficiencies than in the string concept. Furthermore, more flexible systems are achieved since new PV strings with their DC-DC converters can be plugged into the existing platform (Kjaer et al., 2005).

The AC-module technology is illustrated in Figure 2.9(d) and consists of the integration of the PV inverter and module into one electrical device. This inverter concept prevents mismatch losses completely at a module or string level (only mismatch losses at a cell level remain) and permits a high accuracy in MPPT. According to Kjaer et al. (2005), its modular structure allows the system to become a “plug-and-play” device. However, the required voltage amplification to meet the grid requirements translates into lower

efficiency of the inverter compared to inverters with higher power ratings that normally present higher efficiencies.

3 TUT SOLAR PV POWER STATION RESEARCH PLANT

The purpose of the third Chapter is to familiarize the reader with the facilities, instruments and measurement setups, i.e. the TUT solar PV power station research plant and its measurement systems used to analyze the operation of PV power plants and to experimentally verify the performance of the simulation models developed in this thesis. The PV facility and its location through the rooftop of the building are presented first. Following, the measurement systems included in the research plant, i.e., climatic measurement, electrical measurement and data-acquisition systems, as well as the SQL-based database are described and details regarding their design justification are given. Additionally, the selection of the sampling frequency, as a critical parameter of the system, is determined based on short-circuit current measurements of a PV module to permit detecting even the fastest phenomena related to power generation with PV power plants. The content of this Chapter has been presented earlier in (Torres Lobera et al., 2013).

3.1 PV Power Generator

The solar PV power station research plant consists of 69 PV modules model NAPS NP190GKg with a total peak power of 13.1 kWp. Each PV module consists of 54 polycrystalline silicon solar cells connected in series, physically located as 6 horizontal rows, and encapsulated in ethylene vinyl acetate (EVA) with a 4 mm iron tempered glass as top cover. The PV module's electrical performance is included in Table 3.1 under Standard Test Conditions.

Table 3.1: Electrical performance of the NP190GKg PV module under STC.

Parameter	Value
P_{MPP} (W)	190.00
V_{MPP} (V)	25.80
I_{MPP} (A)	7.36
V_{OC} (V)	33.00
I_{SC} (A)	8.00

The PV modules, designed for grid connected PV applications, include 3 protection bypass diodes connected in parallel to the cells. Each diode protects a group of 18 PV cells (2 horizontal rows) preventing them from hot-spotting by driving the current if any of the cells is shaded, damaged, etc.

In the basic configuration, the TUT PV system is composed of 3 series connected strings of 17 PV modules and 3 strings of 6 modules with MPP voltages of 440 V and 155 V at STC, respectively. Actually, all possible electrical configurations with the 69 modules can be set and utilized. The location of PV strings has been selected to avoid complete shading of strings during any time of the day or year. However, several groups of modules are partially shaded during different seasons of the year at different times of the day as seen in Figure 3.1. This characteristic permits us to undertake research on different environmental aspects such as MPPT in cases of partial shading due to building structures (Mäki and Valkealahti, 2012b).

Figure 3.1: Example of partial shading of a PV string due to a building structure on a sunny day in spring 2012.

The layout of the TUT solar power station research plant is illustrated in Figure 3.2. It shows the PV strings and modules located through most of the rooftop of the Department as well as the location of the different sensors of the measuring systems, which will be further described in the following sections. The modules are mounted with a tilt angle of 45°, thus maximizing the annual power production. More details and schemes regarding the specifications of all the equipment included in TUT Solar PV Power Station Research Plant can be found in (Torres Lobera, 2011).

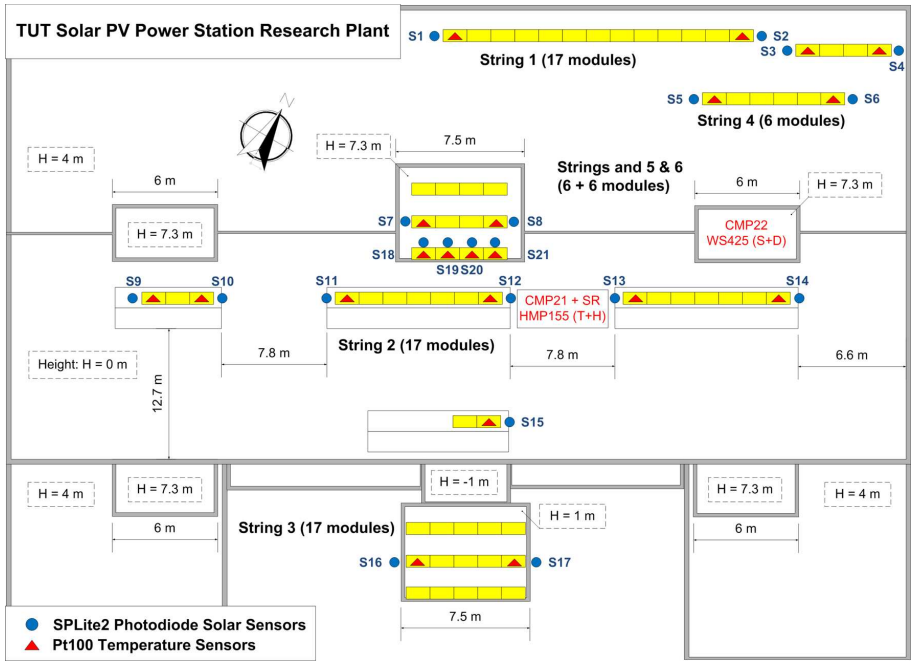

Figure 3.2: Layout scheme of the TUT solar PV power station research plant including its climatic measuring system. The location of the PV modules is shown with yellow rectangles.

3.2 Measurement Systems

3.2.1 Atmospheric Measurements

The atmospheric conditions measurement system is composed of an inclusive state of the art weather station and a mesh of irradiance and PV module temperature measurements. The sensor mesh is positioned throughout the PV power facility and records the operating conditions of every PV module string of the plant. The novelty of the climatic measuring systems comes from the data-acquisition system which collects measurements continuously from all sensors with a 10 Hz sampling frequency. This means that even the fastest dynamical phenomena affecting the operation of the PV power plant are noticed.

The automatic weather station (World Meteorological Organization, 2008) measures the global atmospheric conditions under which the PV facility is operating. It includes measurements of ambient temperature, relative humidity, wind speed and wind direction, as well as incoming global and diffuse solar radiation on the horizontal plane. The weather station measures global solar radiation with the pyranometer CMP22 (Kipp&Zonen) and diffuse component of the radiation with the pyranometer CMP21 (Kipp&Zonen) combined with a shadow ring CMC121 (Kipp&Zonen), blocking the direct solar radiation.

Wind speed and direction are measured with an ultrasonic wind sensor WS425 (Vaisala), and ambient temperature and humidity with the sensor HMP155 (Vaisala).

The weather station comprises equipment in two different locations of the roof. The CMP21 pyranometer mounted with the shadow ring, the $HMP155_t$ ambient temperature sensor and the $HMP155_h$ relative humidity sensor are located on the lower rooftop for accessibility and safer adjustment of the shadow ring, especially during winter when the roof is covered with snow and ice. The CMP22 pyranometer and the WS425 wind sensor are located at the highest point of the rooftop to measure the overall solar radiation and the wind profile at the power plant with minimum disturbance due to the building structures.

The mesh of irradiance and module temperature sensors is composed of 21 pairs of SPLite2 photodiodes (Kipp&Zonen) and Pt100 temperature sensors. These pairs are located at the ends of every PV string, thus providing detailed information on the operating condition at string and module levels. The photodiodes are mounted with the same tilt angle as the PV modules, and the Pt100 sensors are attached to the back-plates of the solar modules. The location of these sensors in the PV plant is shown in Figure 3.2 and their installation in Figure 3.3.

(a) (b) (c)

Figure 3.3: (a) WS425 wind sensor and CMP22 pyranometer, (b) HMP155 sensors with temperature and humidity probes equipped with radiation shields and CMP21 pyranometer combined with the CMC121 shadow ring, and (c) SPLite2 photodiode sensor attached to a PV module.

The large amount of data recorded continuously to the database from the climatic and radiation sensors can be utilized in various ways. As is commonly known, the available output power of a PV generator depends not only on the received solar radiation, but also on the operation temperature of the modules with a thermal coefficient of the

order of -0.5 %/°C. PV module temperature follows with a delay as radiation changes depending on various heat transfer processes. It also depends on various climatic variables (Torres Lobera and Valkealahti, 2013a).

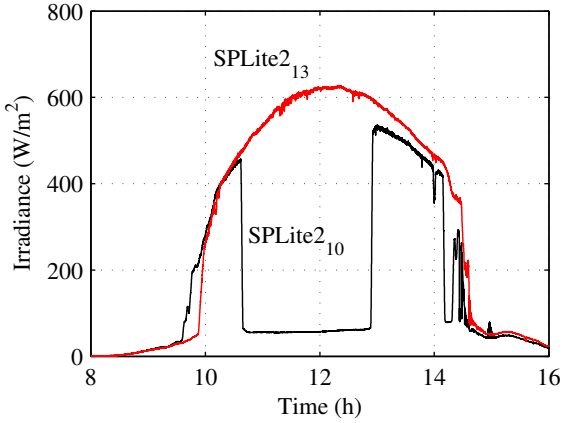

(a)

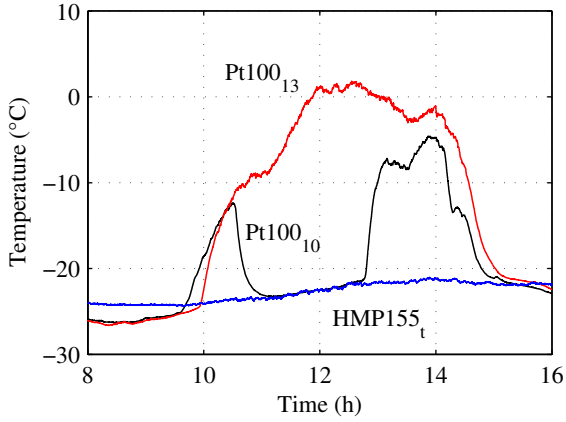

(b)

Figure 3.4: Irradiance and climatic data measured on a sunny day of February 2nd, 2012. (a) Irradiances received by two PV modules equipped with sensors $SPLite2_{10}$ and $SPLite2_{13}$ (see Figure 3.2). (b) Corresponding module temperatures measured by sensors $Pt100_{10}$ and $Pt100_{13}$ together with the ambient temperature measured with sensor $HMP155_t$.

In Figure 3.4, the measured environmental parameters are shown during a clear sunny day on February 2nd, 2012 for two PV modules of the power plant to illustrate the applicability of the measurements system. A typical strong overall correlation exists between the module temperature and the incoming irradiance. The PV module equipped

with sensors S13 (Figure 3.2) receives solar radiation during the whole day without any major shading and the module temperature follows radiation changes with certain delay. This delay is directly related to the heat capacity of the module and to the heat transfer between the module and the environment. The PV module equipped with sensors S10 receives solar radiation after sunrise and before sunset, but is shaded by a building structure in the middle of the day so that only diffuse radiation is received. Although incident radiation changes rapidly, changes in temperature are slow, due to the thermal mass of the modules. The ambient temperature changed only slightly during the day, having minimal effect on changes in the module temperature. Also humidity stayed practically constant during the day as shown in Figure 3.5.

Changes in temperature primarily follow changes in irradiance in Figure 3.4, but temperature fluctuations around eleven o'clock and at half past one do not directly correlate with irradiances. This demonstrates that also other environmental variables affect the module temperature in addition to solar radiation. The higher wind speed before eleven o'clock (Figure 3.5(a)) obviously cools down the modules more effectively in the morning than at noon. In the afternoon at around half past one, there is a period of low wind speed causing the heating of the modules before two o'clock. Also sensor 13 seems to have a better shelter from the wind than sensor 10 during this day due to building structure. Overall, the measured PV module temperatures deviate up to 10 °C from the assumed module temperatures based on direct correlation with the incident radiation. Accordingly, an error of 5 % in the estimated electric energy yield of the module can be expected if only incident solar radiation is used to estimate the module temperature. Therefore, a more advanced dynamic thermal model is needed to model the electrical behavior of PV modules and generators reliably (Armstrong and Hurley, 2010; Jones and Underwood, 2001; Mattei et al., 2006; Skoplaki et al., 2008; Torres Lobera and Valkealahti, 2013a).

The sun rises only slightly above the horizon in southern parts of Finland in the midwinter. Therefore, PV modules with a tilt angle of 45° receive much higher irradiance than pyranometers measuring irradiances on a horizontal surface (Figure 3.5(b)). The irradiance received by the PV modules increases sharply after the sun becomes visible and decreases as sharply in the afternoon during sunset. Before the sunrise and after the sunset there is a two-hour period of considerable diffuse irradiance. Even at midday, diffuse radiation constitutes nearly 40 % of the global radiation. This is mostly due to reflection of solar radiation from snow. It also explains part of the high irradiance received by the PV modules, because they are more exposed to diffuse radiation from the snow than the pyranometers facing the sky.

During summer, the sun sets in Finland only slightly below the horizon for few hours, leaving a weak intensity of light. Daytime solar irradiance is of course higher than in

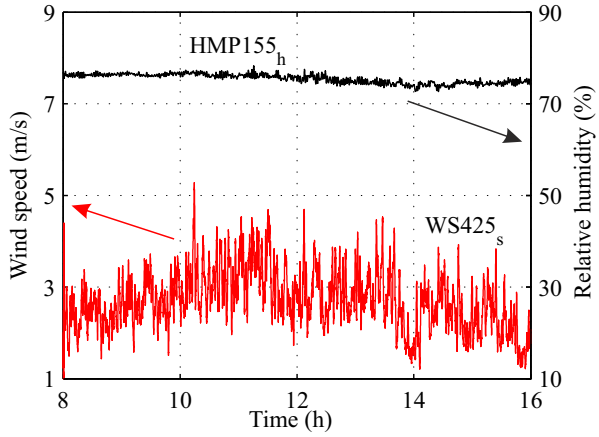

(a)

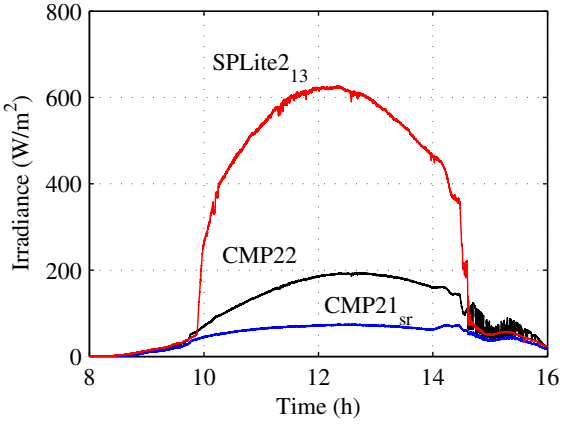

(b)

Figure 3.5: Irradiance and climatic data measured on a sunny day of February 2nd, 2012. (a) Wind speed and relative humidity measured by sensors $WS425_s$ and $HMP155_h$, respectively. (b) Irradiance received by the PV module equipped with sensor $SPLite2_{13}$ together with the global and diffuse irradiances at the research plant measured by pyranometers CMP22 and $CMP21_{sr}$, respectively.

winter time, but the difference is not dramatic. On the other hand, daytime in summer is up to 20 hours, leading to much higher daily energy yield than in the winter time. Both global and direct solar radiation received by the PV modules are considerably high in summer during periods of clear sky. Also diffuse component of radiation is considerable during long periods from sunrise until the sun faces the PV modules and, accordingly, in the evening until the sun sets again.

3.2.2 Current-Voltage Curve Tracing System

The experimental setup for measuring the *I-V* characteristics of the PV generator is composed of four parallel-connected high-power IGBT modules (1200 V and 200 A), the gate drive circuitry, and a high-speed oscilloscope to record the current and voltage data. The setup was designed to enable an *I-V* sweep from a string of 17 PV modules with a peak power of 3.2 kW. The measuring setup operates as follows: the IGBT modules act as regulating resistors (the channel resistance) which are used to realize an adjustable load resistor for the PV generator. Using an external microprocessor, a variable-duty PWM signal is generated and fed to the gate drivers which are then low-pass filtered to supply linear gate voltage ramps to the IGBTs. As the filtered gate voltages exceed the threshold voltage of the IGBTs, the conductivities of the channels increase, forcing the operation point of the PV generator from open-circuit to short-circuit, and thereby enable the *I-V* curve measurement. The *I-V* curve tracer scheme is shown in Figure 3.6 and the designed tracer prototype in Figure 3.7.

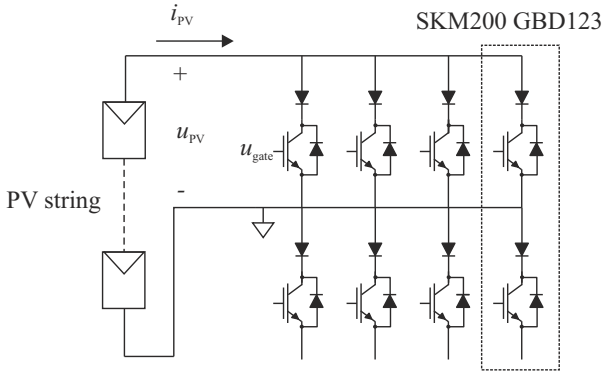

Figure 3.6: Scheme of the *I-V* curve measurement tracer for PV power systems.

The TUT solar PV power station research plant provides excellent conditions to study the operation PV power plants under varying climatic and environmental conditions. Especially the comprehensive measurements around the power plant with high sampling frequency make it possible to study the effects of even the fastest phenomena affecting the electrical operation of the plant. To demonstrate these abilities the effects of partial shading and reflections of solar radiation due to building structures and snow on PV modules and strings have been analyzed by means of the measured electrical *I-V* and *P-V* characteristics (Figure 3.8).

The effect of partial shading on the electrical characteristics of a single PV module is clearly seen in Figure 3.8, where the operation under partial shading conditions on February 3rd, 2012 is compared to the operation under homogeneous conditions on Au-

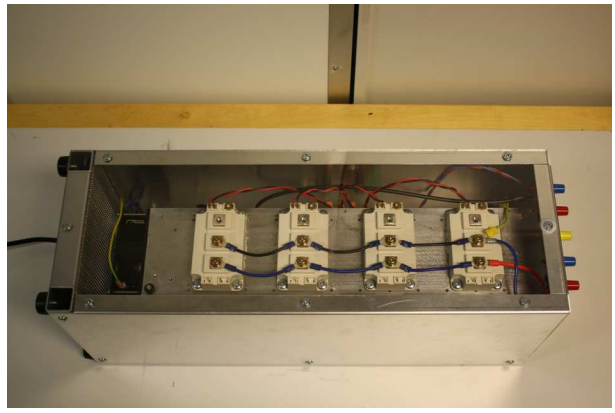

Figure 3.7: Picture of the IGBT modules, cooler and protection box.

gust 31st, 2011. The most important environmental parameter values measured at the instant when the electrical measurements were taken are included in Table 3.2. In this case, the partial shading is caused by a thin layer of ice covering the lower row of PV cells and, thereby, filtering the solar radiation received by them. While the rest of the cells on the upper rows receive sunlight directly at an irradiance level of 430 W/m^2, the row of cells covered by ice received approximately two thirds of the incoming irradiance.

Table 3.2: Environmental conditions of the PV module equipped with radiation and temperature sensors S19 at the moments, when curves in Figure 3.8 were measured.

Date	Time	Irradiance (W/m^2)	Mod. Temp. (°C)
August 31st, 2011	12:04 h	450.8	32.42
February 3rd, 2012	11:19 h	429.5	-12.10

Operation of the PV module under two different irradiance levels leads to two local MPPs in contrasts with the typical operation under homogeneous irradiance level, which produces one unique global MPP as can be seen in Figure 3.8(b). Disparity between the open circuit voltages of the two measurements is due to the different operating temperatures. This textbook level example demonstrates how simple partial shading condition and difference in ambient temperature are seen on a module level in real measurements. This kind of shading is typically caused also by building structures which can be analyzed systematically from the measured data.

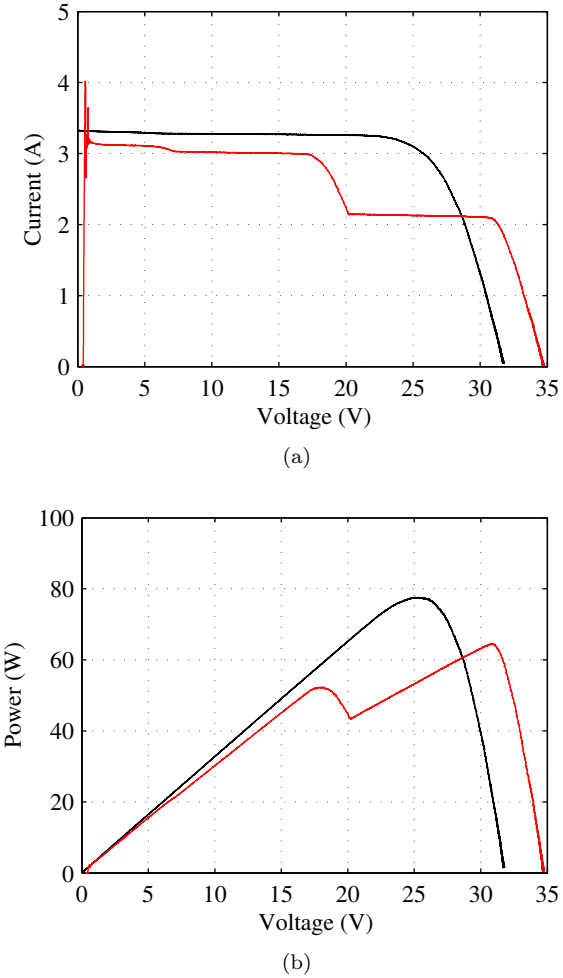

Figure 3.8: Measured (a) *I-V* and (b) *P-V* characteristics of the PV module equipped with irradiance and temperature sensors S19 under homogeneous irradiance on August 31st, 2011 at 12:04 h (blue lines) and under partial shading conditions on February 3rd, 2012 at 11:19 h (red lines).

3.2.3 Synchronized Data Acquisition System

All the climatic data are acquired, transmitted and recorded continuously in a database making them accessible for later analysis. The data acquisition system is based on CompactRio data acquisition cards from National Instruments enabling a flexible and economical system that uses specific swappable I/O modules to connect the sensor outputs. After collecting the data from the sensors, these cards transmit the data to a PC through Ethernet cable without interference or noise problems.

The database is based on PostgreSQL system, an open-source database management system available for several platforms including Linux, Mac OS X and Microsoft Windows. This system enables information modification and extraction without blocking the storage process. The data is accessed using SQL queries from any computer connected to local area network of the department.

The sampling frequency of climatic measurements is a key parameter since the database will continuously store data acquired from 48 sensors. It has to be fast enough to detect even the fastest phenomena affecting the electrical operation of the PV system, but simultaneously be as long as possible because of the vast amount of data to be processed as well as the storage needs. Among the climatic variables to be acquired, solar radiation has the highest and fastest variations, e.g., there can be changes of over 700 W/m^2 within seconds on days with moving clouds. Therefore, it was essential to find out the sampling frequency required to detect even the fastest phenomena related to power generation with PV power plants. The simplest way to achieve this information was to use a PV module as a solar radiation sensor, and evaluate the effect of sampling frequency from the measurements.

The measured short-circuit current I_{SC} of a single PV-module is illustrated in Figure 3.9 during seven hours on July 1st, 2010 with a sampling frequency of 25 Hz. When the PV module is short-circuited it acts as a solar radiation sensor with its output current linearly changing with the incoming irradiance. A sampling frequency of 25 Hz was considered to be high enough to detect even the fastest changes in irradiance causing an effect on the PV module. A partially cloudy day with moving clouds was chosen to provide the climatic conditions needed to evaluate such effects.

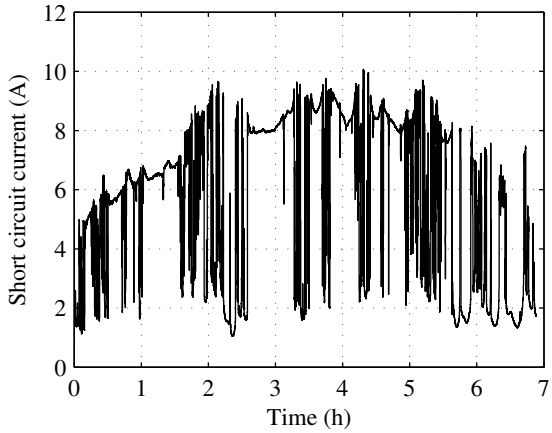

Figure 3.9: Measured I_{SC} of a single PV module during July 1st, 2010 with a sampling frequency of 25 Hz.

In Figure 3.9, values of I_{SC} can be found from 1.05 to 10.06 A, which correspond to irradiance levels between 131 and 1255 W/m^2, respectively. Changes of I_{SC} up to 0.56 A happened between two consecutive measurements (71 W/m^2), which is roughly 5 % of the maximum current during the measurement period. A change of 5 % might not yet have a drastic effect on the electrical characteristic of the PV module, but with this rate of change the current easily goes from minimum to maximum value in a second or vice versa. Such fast climatic changes demonstrate the need of high sampling frequency.

Taking the 25 Hz measurements as reference and down-sampling the acquisition frequency permits us to evaluate the effect of sampling frequency on the accuracy of the solar radiation measurements. The standard deviation error of the measured solar radiation is shown as a function of the sampling frequency in Figure 3.10.

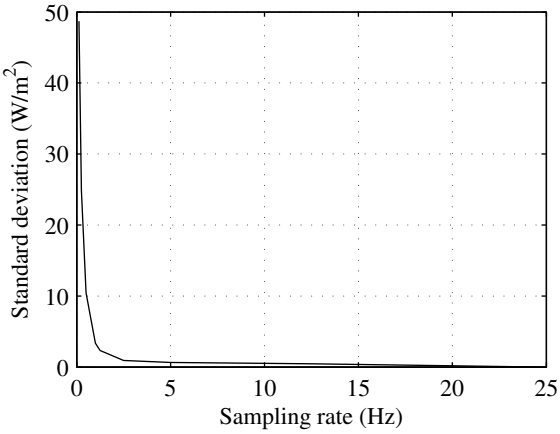

Figure 3.10: Standard deviation error of the incoming solar radiation as a function of the sampling frequency on a single PV module during a period of 7 hours on July 1st, 2010.

In Figure 3.10, an inverse exponential behavior of the standard deviation error can be seen with increasing sampling rate at low sampling rates as expected. The standard deviation error starts to grow considerably when sampling frequency goes below 5 Hz, and increases up to 48.7 W/m^2 at 0.125 Hz. Sampling frequencies over 5 Hz result in small standard deviation of incoming radiation below 1 W/m^2. Therefore, a sampling frequency of 10 Hz was considered to be sufficient for detecting even the fastest phenomena related to power generation with PV power plants.

4 MODELING OF THE OPERATION OF PV GENERATORS

This Chapter presents the theory behind the dynamic thermal and electric simulation models implemented in this work. They will be integrated together and experimentally validated in Chapter 5. The dynamic thermal model is based on the total energy balance in the module in which all essential heat transfer mechanisms between the module and the environment are modeled theoretical. The electric model is based on the well-known one-diode model and a method is introduced to derive the unknown parameters from the manufacturer's information datasheet. The content of this Chapter has been presented earlier in the theoretical sections of (Torres Lobera and Valkealahti, 2013a) and (Torres Lobera and Valkealahti, 2014a).

4.1 Introduction

The electrical performance of PV modules is affected by climatic conditions directly via incident solar radiation and indirectly via operating temperature which depends on other factors such as ambient temperature, incident radiation, wind speed and direction, and the physical properties of the module material (Nagae et al., 2006; Torres Lobera and Valkealahti, 2013a). The operating cell temperature plays, in fact, an important role in the photovoltaic conversion process. The output voltage of the PV module decreases considerably with increasing temperature which leads to a significant reduction in the produced power (Skoplaki et al., 2008). There is extensive literature on the modeling of the non-linear electric characteristics, i.e. current-voltage curve, of PV cells and modules. Some authors have presented two-diode electric models (Gosh et al., 1980) or even three-diode models (Nishioka et al., 2007) which intend to increase the accuracy of the fitted I-V curves. The implementation of these models, however, implies a high computational cost which does not balance with the increased accuracy. Due to this reason, most of the authors have opted for a simplified and more practical one-diode model with five unknown parameters which provides enough accuracy (Gow and Manning, 1999; Liu and Dougal, 2002; Tsai and Tsai, 2012; Villalva et al., 2009b).

Previous work in modeling the temperature of PV modules has focused on obtaining correlations to predict the module temperature by assuming steady-state conditions

(Chenni et al., 2007; Durisch et al., 2007; Franghiadakis and Tzanetakis, 2006; Krauter, 2004; Malik and Damit, 2003; Mattei et al., 2006; Nordmann and Clavadetscher, 2003; Schott, 1985; Servant, 1985; Topic et al., 2007) or by extrapolating from a known reference state, such as the nominal operating cell temperature (NOCT) (Skoplaki et al., 2008; Skoplaki and Palyvos, 2009). However, a steady-state model of the PV module temperature cannot be justified during periods of rapid irradiance fluctuations (Jones and Underwood, 2001). The thermal mass of the module becomes significant during such unstable conditions and the aforementioned temperature correlations can lead to errors of over 20 °C in the predicted module temperatures.

Almost all authors have focused on either the electric or the thermal modeling of PV cells and modules. Only in (Tsai and Tsai, 2012) an integrated thermal and electrical model can be found where the authors presented and verified a complete model which takes into consideration both temperature and electrical characteristics. However, Tsai and Tsai (2012) used some simplifications in the design of the thermal model. Moreover, the voltage of the PV module needed to be known in their model to simulate the instantaneous generated current. In this work, a state of the art integrated simulation model for PV modules is proposed. The simulation model is comprised by the developed dynamic thermal and electric models.

4.2 Dynamic Thermal Model

The module temperature is calculated considering the thermal energy exchange of the module with its environment through the main heat transfer mechanisms indicated in Figure 4.1. Establishing the total energy balance on the PV module leads to the following expression:

$$q_{\text{in}} - P - q_{\text{loss}} - C_{\text{mod}} \frac{dT_{\text{mod}}}{dt} = 0, \tag{4.1}$$

where q_{in} is the incoming shortwave solar radiation reaching the front surface of the PV module, P is the electric power produced by the module, q_{loss} includes the heat transfer losses from the PV module to the environment and vice versa, C_{mod} is the heat capacity of the PV module, T_{mod} is the module temperature, and t is time.

The effective incoming solar radiation reaching the front surface of the PV module can be calculated as

$$q_{\text{in}} = \alpha G A, \tag{4.2}$$

where G is the incoming solar irradiance on the tilted PV module, α the absorptivity and A the area of the PV module.

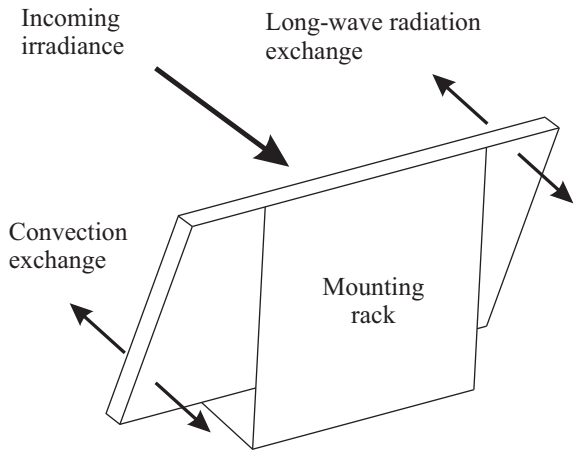

Figure 4.1: Diagram of the mounting configuration of the PV module with its mounting rack. The heat transfer processes are indicated with arrows.

The output power can be extracted directly from the electrical current-voltage characteristic of the PV module as

$$P = IV, \tag{4.3}$$

where I is the produced current and V the voltage.

The main mechanisms of heat loss from the PV module to the environment are conduction, convection and radiation. However, the contact area between the PV module and its mounting rack is small and the conduction losses can be neglected leading to

$$q_{\mathrm{loss}} = q_{\mathrm{conv}} + q_{\mathrm{lw}}, \tag{4.4}$$

where q_{conv} is the heat loss due to convection, and q_{lw} due to long-wave radiation.

Heat capacity refers to the energy transfer required to change the temperature of an object. In the case of the PV panel, which is a multi-layer laminate, the module heat capacity has been calculated traditionally as a composite of the heat capacities of layers in the laminate:

$$C_{\mathrm{mod}} = \sum_{\mathrm{i}}^{\mathrm{N}} A d_{\mathrm{n}} \rho_{\mathrm{n}} C_{\mathrm{p,n}}, \tag{4.5}$$

where d_{n} is the thickness, ρ_{n} the density and $C_{\mathrm{p,n}}$ the specific heat of layer n and N is the number of layers in the module.

Because exact heat capacity of the studied PV modules or material parameters of

module layers were not available, the values in Table 4.1 served as first approximation to obtain the heat capacity. In Chapter 5 the value of heat capacity is adjusted based on experimental measurements to its optimal value by a sensitivity analysis. If actual material parameters of the PV module were known, the final heat capacity could be calculated directly in line with the first approximation.

Table 4.1: Parameter values used to calculate the heat capacity of the studied PV module NP1900Gkg (Armstrong and Hurley, 2010; Jones and Underwood, 2001). The surface area of the module is A = 1.32 m^2.

Layer	d_n (m)	$C_{p,n}$ (J/kgK)	ρ_n (kg/m^3)	$Ad_nC_{p,n}\rho_n$ (J/K)
Glass	0.00400	500	3000	7920
EVA	0.00100	2090	960	2648
PV cells	0.00020	677	2330	416
Rear contact	0.00001	900	2700	32
Rear cover	0.00400	1250	1200	7920
Total				18936

4.2.1 Convective Loss

Convective heat transfer occurs between the PV module surface and the surrounding layer of air. The convective mechanisms for PV modules are free convection and forced convection due to wind. In practice, it is problematic to model convective mechanisms and, therefore, empirical functions have usually been used for approximating the convection losses (Notton et al., 2005). Therefore, only the forced convection component has traditionally been considered when modelling the PV module operating temperature. However, in this model, both free and forced convection mechanisms are considered to more accurately reproduce the heat exchange between the PV module and the surrounding air in line with (Incropera, 2007).

According to Newton's law of cooling, the convective losses are proportional to the overall temperature difference between the surface and the fluid. For the PV module they are defined as

$$q_{conv} = Ah_{conv}\left(T_{mod} - T_{air}\right), \tag{4.6}$$

where h_{conv} is the convection heat transfer coefficient and T_{air} is the ambient air temperature. The convection heat transfer depends on the physical situation, e.g. the mounting of the module, and the wind conditions.

For obtaining h_{conv} both the free and forced convection heat transfers must be calculated. This is conventionally done by applying air properties in the vicinity of the surface. Because the temperature differences in the vicinity of the PV module surface

are reasonable, the average of the PV module surface temperature T_{mod} and the ambient air temperature T_{air}

$$T_{\text{film}} = \frac{T_{\text{mod}} + T_{\text{air}}}{2} \tag{4.7}$$

is adequate to calculate air properties. The air properties needed are the specific heat C_{p}, density ρ, kinematic viscosity v, thermal conductivity k_{t}, and Prandtl number Pr. These values are obtained by interpolating the values found in the tables of air properties (Weast, 1984), or by finding the best curve fit of the values in the tables and using the obtained equations to evaluate the air properties at the film temperature.

The characteristic length L of the object, needed to calculate free and forced convective heat transfer coefficients, is obtained as follows

$$L = \frac{A}{2\,(H + W)}, \tag{4.8}$$

where H is the height and W the width of the PV module. The free convection heat transfer coefficient is defined as

$$h_{\text{free}} = \frac{Nu_{\text{free}} k_{\text{t}}}{L}, \tag{4.9}$$

where Nu_{free} is the Nusselt number for free convection. The most commonly used empirical correlation for external free convection flows in a plate inclined less than 60 ° is (Incropera, 2007):

$$Nu_{\text{free}} = 0.68 + 0.67\,(Ra_{\text{L}}\Psi)^{\frac{1}{4}}\,, \tag{4.10}$$

when the Rayleigh number Ra_{L} is in the range $0 < Ra_{\text{L}} < 10^9$. Ψ is a function dependent on the Prandtl number and is defined as (Incropera, 2007)

$$\Psi = \left(1 + \left(\frac{0.492}{Pr}\right)^{\frac{9}{16}}\right)^{-\frac{16}{9}}. \tag{4.11}$$

The Rayleigh number is defined as (Incropera, 2007)

$$Ra_{\text{L}} = Gr_{\text{L}} Pr = \frac{9.81\cos(\psi)\,|T_{\text{mod}} - T_{\text{air}}|\,L^3}{T_{\text{film}} v^2} Pr, \tag{4.12}$$

where Gr_{L} is the Grashof number and ψ is the angle of the PV module to the vertical direction.

Sparrow and Tien (1977) proposed an empirical method of calculating the forced

heat transfer coefficient and showed that it can be calculated regardless of the module orientation. This method has already been utilized in (Balog et al., 2009) and it defines the forced heat transfer coefficient as

$$h_{\text{forced}} = \frac{0.931 \rho v C_{\text{p}} Re^{\frac{1}{2}}}{L Pr^{\frac{2}{3}}}, \tag{4.13}$$

where Re is the Reynolds number. It is defined as

$$Re = \frac{L}{\rho v} v_{\text{w}}, \tag{4.14}$$

where v_{w} is the local wind speed. The Nusselt number for forced convection can be calculated as

$$Nu_{\text{forced}} = \frac{h_{\text{forced}} L}{k_{\text{t}}}. \tag{4.15}$$

Both free and forced convection mechanisms are combined into one convective mechanism by the approximation (Incropera, 2007)

$$Nu^3_{\text{conv}} = Nu^3_{\text{free}} + Nu^3_{\text{forced}}, \tag{4.16}$$

such that

$$h_{\text{conv}} = \frac{Nu_{\text{conv}} k_{\text{t}}}{L}. \tag{4.17}$$

The proposed approach to obtain the convection coefficients intends to achieve a good accuracy in the prediction of module temperature with a necessary simple approach to reduce the computational cost of estimating the module temperature by the second during long periods of time as will be discussed in Chapter 5. However, it is noteworthy that deducing the convection coefficients utilizing computational fluid dynamics (CFD) can provide a much higher level of accuracy and help analyzing the thermal dynamics of the PV modules in more detail.

4.2.2 Black-Body Radiation Losses

The rate of long wave electromagnetic energy radiation (black body radiation) per unit area of a body at a surface temperature T is given by the Stefan-Boltzmann law:

$$q_{\text{lw}} = \sigma \varepsilon T^4, \tag{4.18}$$

where σ is the Stefan-Boltzmann constant and ε is the emissivity of the surface.

Thus the heat flux from the front and back sides of a PV module standing freely on the roof of a building are, respectively:

$$\begin{aligned} q_{\text{lw,front}} &= A\left[\sigma\varepsilon_{\text{front}}F_{\text{fs}}\left(T_{\text{mod}}^4 - T_{\text{sky}}^4\right) + \sigma\varepsilon_{\text{front}}F_{\text{fr}}\left(T_{\text{mod}}^4 - T_{\text{roof}}^4\right)\right], \\ q_{\text{lw,back}} &= A\left[\sigma\varepsilon_{\text{back}}F_{\text{bs}}\left(T_{\text{mod}}^4 - T_{\text{sky}}^4\right) + \sigma\varepsilon_{\text{back}}F_{\text{br}}\left(T_{\text{mod}}^4 - T_{\text{roof}}^4\right)\right], \end{aligned} \tag{4.19}$$

where $\varepsilon_{\text{front}}$ and $\varepsilon_{\text{back}}$ are the emissivities of the front and back surfaces, respectively, and F_{fs}, F_{fr}, F_{bs} and F_{br} are the view factors from the front-to-sky, front-to-roof, back-to-sky and back-to-roof, respectively. T_{mod} is the module temperature, T_{sky} the sky temperature, and T_{roof} the temperature of the roof.

The emissivity of the front and back surfaces of the PV module is typically considered to be between 0.9 and 1 (Balog et al., 2009). The view factor is the fraction of radiation which leaves a surface and reaches another surface Holman (2002). For a PV module mounted with a tilted angle $0 \leq \beta \leq \pi$ the view factors are calculated as:

$$\begin{aligned} F_{\text{fs}} &= \frac{1}{2}\left(1 + \cos\beta\right), \; F_{\text{bs}} = \frac{1}{2}\left(1 + \cos\left(\pi - \beta\right)\right), \\ F_{\text{fr}} &= \frac{1}{2}\left(1 - \cos\beta\right), \; F_{\text{br}} = \frac{1}{2}\left(1 - \cos\left(\pi - \beta\right)\right). \end{aligned} \tag{4.20}$$

For the case of a PV module mounted with a mounting rack covering the back-plate as illustrated in Figure 4.1, the heat flux of long wave radiation on the back of the module takes place mostly between the module and the mounting rack with a view factor of 1. Accordingly, the radiation heat fluxes on the front and on the back are

$$\begin{aligned} q_{\text{lw,front}} &= A\left[\sigma\varepsilon_{\text{front}}F_{\text{fs}}\left(T_{\text{mod}}^4 - T_{\text{sky}}^4\right) + \sigma\varepsilon_{\text{front}}F_{\text{fr}}\left(T_{\text{mod}}^4 - T_{\text{roof}}^4\right)\right], \\ q_{\text{lw,back}} &= A\sigma\varepsilon_{\text{back}}\left(T_{\text{mod}}^4 - T_{\text{rack}}^4\right), \end{aligned} \tag{4.21}$$

where T_{rack} is the temperature of the mounting rack. It can be approximated to be equal to the ambient air temperature since the mounting rack is normally under the shadow of the PV module for most of the time and perpendicular to the roof. The roof temperature T_{roof} is more complicated to approximate since it depends on the roof material and the warming up of the construction material itself. According to measurements, a black surfaced roof can reach temperatures over 50 °C higher than the ambient air temperature.

The measurement of the sky temperature is complex and scarcely available, which has motivated some authors to either utilize the ambient temperature as the sky temperature (Tsai and Tsai, 2012) or to neglect the contribution of the black-body radiation losses from the PV module to the environment in the overall losses. There is extensive literature about the topic and various formulas have been utilized for the sky temperature (Hegazy, 2000; Jones and Underwood, 2001; Kudish et al., 2002; Notton et al., 2005; Schott, 1985;

Swinbank, 1963). Out of these, the formula given by (Schott, 1985)

$$T_{\mathrm{sky}} = T_{\mathrm{air}} - \delta T,\ \delta T = \left\{ \begin{matrix} 20\ K\ (clear\ sky) \\ 0\ K\ (overcast) \end{matrix} \right\} \tag{4.22}$$

provides the most accurate prediction for calculating the module temperature. This approach considers two possible sky conditions, clear sky and overcast, which implies the need of knowing the sky condition.

The cloud amount is defined as the amount of sky estimated to be covered by clouds and it can be measured using ceilometers (World Meteorological Organization, 2008). However, such a degree of accuracy is not required in this study. Just an index of overcast vs. clear sky is needed. This can be achieved in several ways such as comparing the incoming global solar radiation with the theoretical clear-sky radiation (clearness index (Wong and Chow, 2001)), with a camera recording the sky and analyzing the image or by evaluating the fraction of diffuse radiation from the incoming solar radiation (Wong and Chow, 2001):

$$k_{\mathrm{d}} = \frac{G_{\mathrm{d}}}{G_{\mathrm{h}}}, \tag{4.23}$$

where G_{d} is the diffuse and G_{h} the global incoming solar radiation on the horizontal plane. This parameter represents the ratio of diffuse radiation of the total amount of solar radiation being close to 0 under clear sky conditions, and approaching 1 under overcast conditions. The k_{d} distribution over a year during daytime is illustrated in Figure 4.2 measured at the TUT solar PV power station research plant with a sampling rate of 1 Hz (Torres Lobera and Valkealahti, 2012). The peak near 0.95 corresponds to overcast conditions and around 0.18 to clear sky conditions. The range from 0.3 to 0.7 corresponds to periods of sky partially covered by clouds or during sunrise and sunset. Therefore, it is possible to set a limit value for k_{d} to discriminate between overcast and clear sky conditions.

It is noteworthy that other more sophisticated methods estimate the sky temperature with higher accuracy. However, Schott's approach has been chosen in this work due to its simplicity. It provides very good accuracy for the module temperature of TUT Solar PV Power Station Research Plant.

4.2.3 Calculation Method

According to Section 4.2.2, the module temperature T_{mod} is a nonlinear, time-varying equation without analytical solution. Therefore, it must be solved numerically. Substi-

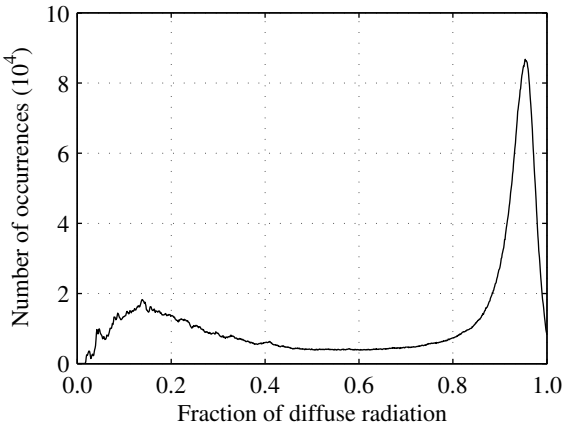

Figure 4.2: Distribution of diffuse fraction of solar radiation k_d over a year during daytime in Tampere, Finland, calculated with solar radiation data measured with a sampling rate of 1 Hz.

tuting Equations 4.2, 4.3, 4.6 and 4.21 in Equation 4.1 yields

$$\begin{aligned}\frac{dT_\mathrm{mod}}{dt} =& \frac{A\alpha G - P - Ah_\mathrm{conv}\left(T_\mathrm{mod} - T_\mathrm{air}\right) - A\sigma\varepsilon_\mathrm{front}F_\mathrm{fs}\left(T_\mathrm{mod}^4 - T_\mathrm{sky}^4\right)}{C_\mathrm{mod}} \\ & - \frac{A\sigma\varepsilon_\mathrm{front}F_\mathrm{fr}\left(T_\mathrm{mod}^4 - T_\mathrm{roof}^4\right) + A\sigma\varepsilon_\mathrm{back}\left(T_\mathrm{mod}^4 - T_\mathrm{rack}^4\right)}{C_\mathrm{mod}}.\end{aligned} \tag{4.24}$$

Then, the module temperature T_mod at time $t + \tau$ can be solved based on the value at time t using Equation 4.24 by the Euler method as

$$T_\mathrm{mod}\left(t + \tau\right) = T_\mathrm{mod}\left(t\right) + \tau\frac{dT_\mathrm{mod}}{dt}, \tag{4.25}$$

where τ is the time step. τ must be small enough to ensure stability of the solving method, which will increase the computational costs in long-term simulations. However, extrapolation of the time used for the simulations included in (Torres Lobera and Valkealahti, 2013a) indicated that annual simulations would require a couple of minutes to be completed. Therefore the computational costs related to the operation of this thermal model should not be a concern.

Measured module temperatures exhibit changes of over 10 °C within a minute. To properly model such fast phenomena, the data required for simulations must be in time series of, at least, 1-second measurements. The parameters needed to develop and test the simulation method based on Equations 4.24 and 4.25 are the incident irradiance in the plane of the PV module, ambient temperature, module temperature, horizontal global

solar radiation, horizontal diffuse solar radiation, wind speed, and module output power. In this work, all parameters are selected in accordance with the characteristics of the PV modules installed at the TUT solar PV power station research plant. The dynamic thermal simulation model of a PV module is developed and tested using measurements collected with the climate and electrical measuring systems of the TUT solar PV power station research plant (Torres Lobera et al., 2013). The response time constants of the measuring instruments have been evaluated and considered to be fast enough to accurately measure the real operating conditions.

4.3 Electric Model

An ideal PV cell can be represented as a current source and a Shockley diode connected in parallel (Villalva et al., 2009a). Such simplification, however, does not represent the real *I-V* characteristic of a PV module. PV modules are usually composed of a number of series-connected PV cells which include parasitic effects. They are normally taken into account by applying series and parallel resistances in the equivalent circuit of a PV module.

The equivalent circuit of a PV module is illustrated in Figure 4.3 including the parasistic restistances. The corresponding electrical characteristic is mathematically described by:

$$I = I_{\mathrm{ph}} - I_{\mathrm{o}} \left[exp\left(\frac{V + IR_{\mathrm{s}}}{aV_{\mathrm{t}}} \right) - 1 \right] - \frac{V + IR_{\mathrm{s}}}{R_{\mathrm{sh}}}, \tag{4.26}$$

where I is the current of the module, V the voltage of the module, I_{ph} the light-generated current, I_{o} the dark saturation current, R_{s} the parasitic series resistance, R_{sh} the parasitic shunt or parallel resistance and a the ideality factor. V_{t} is the thermal voltage and it is calculated as

$$V_{\mathrm{t}} = \frac{N_{\mathrm{s}} kT}{q}, \tag{4.27}$$

where N_{s} is the number of series-connected PV cells comprising the module.

The simulation model used in this work has been developed based on the model presented and validated by Villalva et al. (2009b). It is commonly known as the five parameters model because there are five unknown parameters governing Equation 4.26: I_{ph}, I_{o}, R_{s}, R_{sh} and a. In (Villalva et al., 2009b), the authors detailed the procedure to extract the unknown parameters from three know points of the electrical characteristic of the PV module provided by the manufacturer in STC: Open-circuit voltage V_{OC}, short-circuit current I_{SC} and maximum power point (MPP) current I_{MPP} and voltage V_{MPP}. A modified version of the procedure to define the five parameters is described in the following.

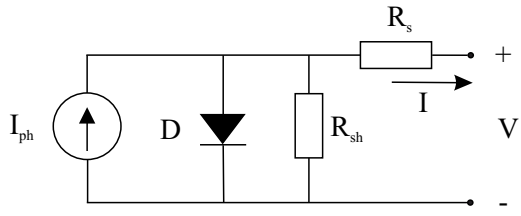

Figure 4.3: Electrical equivalent circuit of a one-diode-based model of a PV module including the series and parallel resistances.

It is noteworthy that several other procedures can be found in the literature to extract the five parameters (De Soto et al., 2006; Lo Brano et al., 2010; Mermoud and Lejeune, 2010). In these, the five parameters are obtained using data provided by the manufacturer and the operating conditions together with a set of semi-empirical equations. In (Laudani et al., 2013), the five parameters model proposed by De Soto is reduced to a two-parameter model, which improved the efficiency of the solution algorithm. Latest, Blair and Dobos (2013) presented a comparison of different photovoltaic model options and the results obtained with them. Out of all these procedures, Villalva's model was the one chosen to be used in this work since it predicts the electrical characteristics with good accuracy for the studied PV modules and the model is simple enabling fast computation when simulating *I-V* curves with real measurements registered at a high sampling rate during long periods of time.

The light-generated current is closely proportional to the absorbed radiation and can be extracted from the short-circuit point of the PV module *I-V* characteristic in STC by adding the effect of temperature and irradiance on the current as

$$I_{\mathrm{ph}} = \left(I_{\mathrm{SC,STC}} + K_{\mathrm{i}}\Delta T\right)\frac{G}{G_{\mathrm{STC}}}\left(1 + \frac{R_{\mathrm{s}}}{R_{\mathrm{sh}}}\right), \tag{4.28}$$

where $I_{\mathrm{SC,STC}}$ is the short-circuit current in STC, K_{i} the short-circuit temperature coefficient for current, ΔT the module temperature difference with respect to STC, G the absorbed irradiance and G_{STC} the absorbed irradiance in STC.

The dark saturation current depends on the structure and material of the PV cells and can be obtained in open circuit condition by adding the effect of temperature on the voltage. It is defined as

$$I_{\mathrm{o}} = \frac{\left(I_{\mathrm{SC,STC}} + K_{\mathrm{i}}\Delta T\right) - \frac{V_{\mathrm{OC,STC}} + K_{\mathrm{v}}\Delta T}{R_{\mathrm{sh}}}}{exp\left(\frac{V_{\mathrm{OC,STC}} + K_{\mathrm{v}}\Delta T}{aV_{\mathrm{t}}}\right) - 1}, \tag{4.29}$$

where $V_{\mathrm{OC,STC}}$ is the open circuit voltage in STC and K_{v} the open-circuit temperature

coefficient for voltage.

Villalva et al. (2009b) stated that the ideality factor should be a constant value which may be initially picked out between 1 and 1.5 and later adjusted to improve the fitting of the model. Several authors (Carrero et al., 2007; Walker, 2001) have discussed methods to estimate the correct value of a. A value of 1.3 has been found to provide accurate results for the NAPS190GKg PV modules and has been used in this work. This has been concluded based on a comparison of simulation results with a large amount of measurements under different operating conditions. However, it is worth to note that the value of a depends on cell technology which has been empirically analyzed by Dobos (2012).

Two parameters still remain unknown in Equation 4.26: R_s and R_sh. There are several studies which propose iterative mathematical solutions to obtain the series and shunt resistances for the model. However, only one pair of R_s and R_sh guarantees that the maximum power $P_\mathrm{MPP,STC}$ is reached at the MPP voltage $V_\mathrm{MPP,STC}$ and current $I_\mathrm{MPP,STC}$ given by the manufacturer in STC. It is possible to obtain the right set of values for R_s and R_sh from a system of two equations. The MPP power is obtained as

$$P_\mathrm{MPP,STC} = V_\mathrm{MPP,STC} I_\mathrm{MPP,STC}, \tag{4.30}$$

which serves as the first equation. Substituting $I_\mathrm{MPP,STC}$ obtained by Equation 4.26 in Equation 4.30 results in

$$\begin{aligned} \frac{P_\mathrm{MPP,STC}}{V_\mathrm{MPP,STC}} =& I_\mathrm{ph,STC} - I_\mathrm{o,STC}\left[exp\left(\frac{V_\mathrm{MPP,STC} + I_\mathrm{MPP,STC}R_\mathrm{s}}{aV_\mathrm{t}}\right) - 1\right] \\ & - \frac{V_\mathrm{MPP,STC} + I_\mathrm{MPP,STC}R_\mathrm{s}}{R_\mathrm{sh}}, \end{aligned} \tag{4.31}$$

where $I_\mathrm{ph,STC}$ is the light generated current and $I_\mathrm{o,STC}$ the dark saturation currents in STC. The second equation can be obtained from the derivative of power with respect to voltage:

$$\frac{dP}{dV} = I + V\frac{dI}{dV}. \tag{4.32}$$

At the MPP given by the manufacturer, the derivative of power must be zero. Further, by substituting the derivative of the current and the current in STC in Equation 4.32 at

the MPP results into

$$\begin{aligned} &V_{\mathrm{MPP,STC}}\left[\frac{I_{\mathrm{o,STC}}}{aV_{\mathrm{t}}}exp\left(\frac{V_{\mathrm{MPP,STC}}+I_{\mathrm{MPP,STC}}R_{\mathrm{s}}}{aV_{\mathrm{t}}}\right)+\frac{1}{R_{\mathrm{sh}}}\right] \\ &=I_{\mathrm{MPP,STC}}\left[\frac{R_{\mathrm{s}}}{R_{\mathrm{sh}}}+\frac{R_{\mathrm{s}}I_{\mathrm{o,STC}}}{aV_{\mathrm{t}}}exp\left(\frac{V_{\mathrm{MPP,STC}}+I_{\mathrm{MPP,STC}}R_{\mathrm{s}}}{aV_{\mathrm{t}}}\right)+1\right]. \end{aligned} \tag{4.33}$$

It is easy to notice that it is not possible to obtain an expression of R_{s} from neither Equation 4.31 nor Equation 4.33. However, two expressions for R_{sh} can be obtained from them in which the only unknown parameter is R_{s}:

$$R_{\mathrm{sh}}=\frac{V_{\mathrm{MPP,STC}}+I_{\mathrm{MPP,STC}}R_{\mathrm{s}}-I_{\mathrm{SC,STC}}R_{\mathrm{s}}+\left(I_{\mathrm{SC,STC}}R_{\mathrm{s}}-V_{\mathrm{OC,STC}}\right)C1}{I_{\mathrm{SC,STC}}\left(1-C1\right)-\frac{P_{\mathrm{MPP,STC}}}{V_{\mathrm{MPP,STC}}}}, \tag{4.34}$$

$$R_{\mathrm{sh}}=\frac{\left(V_{\mathrm{MPP,STC}}-I_{\mathrm{MPP,STC}}R_{\mathrm{s}}\right)\left[1+\left(I_{\mathrm{SC,STC}}R_{\mathrm{s}}-V_{\mathrm{OC,STC}}\right)C2\right]}{I_{\mathrm{MPP,STC}}+\left(I_{\mathrm{MPP,STC}}R_{\mathrm{s}}-V_{\mathrm{MPP,STC}}\right)I_{\mathrm{SC,STC}}C2}, \tag{4.35}$$

where

$$C1=\frac{exp\left(\frac{V_{\mathrm{MPP,STC}}+I_{\mathrm{MPP,STC}}R_{\mathrm{s}}}{aV_{\mathrm{t}}}\right)-1}{exp\left(\frac{V_{\mathrm{OC,STC}}}{aV_{\mathrm{t}}}\right)-1} \tag{4.36}$$

and

$$C2=\frac{1}{aV_{\mathrm{t}}}\frac{exp\left(\frac{V_{\mathrm{MPP,STC}}+I_{\mathrm{MPP,STC}}R_{\mathrm{s}}}{aV_{\mathrm{t}}}\right)}{exp\left(\frac{V_{\mathrm{OC,STC}}}{aV_{\mathrm{t}}}\right)-1}. \tag{4.37}$$

Therefore, finding a value of R_{s} which results in the same value of R_{sh} for both expressions provides a pair of values so that the model meets the specifications given by the manufacturer.

It is important to remark that the selected value of the ideality factor is strongly related to the pair of values R_{s} and R_{sh}, consequently I_{ph} and I_{o} too, and may influence the results of the model. This is demonstrated in Figure 4.4, where the variation of the series and shunt resistances with respect to the ideality factor a is shown for the NAPS NP190GKg PV modules. It can be observed that selecting values of a larger than 1.38 results into incorrect solutions since R_{sh} obtains negative values. More detailed analyses on the extraction of the simulation model parameters and on the sensitivity of the predicted I-V curves on small differences in the model parameters can be found in (Cubas et al., 2014; Li et al., 2013).

Bypass diodes are separate and independent components of the PV module and they need to be modeled separately. The effect of the bypass diodes used to protect the cells

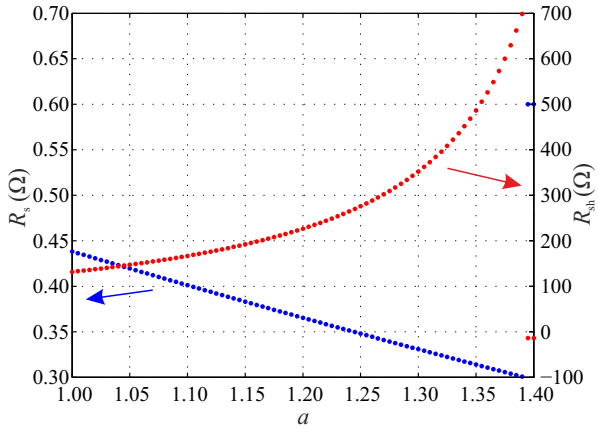

Figure 4.4: Variation of series and shunt resistances with respect to the ideality factor for the NAPS190GKg PV module.

against hot spotting in the PV modules can be modeled by assuming the *I-V* characteristics of the diodes to obey Equation 4.26, when R_{sh} is considered to be infinite and I_{ph} to be zero. The rest of the parameters can be obtained by means of fitting Equation 4.26 to the measured *I-V* curve characteristics of a Shottky diode (Mäki et al., 2012).

Once the parameters of the electric model of the PV module are defined and the model is complete, the *I-V* characteristics can be obtained under given operating conditions (irradiance and module temperature) by driving the voltage from zero to the open circuit voltage and solving Equation 4.26 numerically to get the generated current at each voltage point. Alternatively, it is possible to drive the current from zero to the short-circuit current and solve the voltage for each current value numerically. In series-connected modules, the same current flows through all the modules while the total voltage produced by the PV string results from adding up the voltages produced by each PV module. Therefore, in case of series-connected PV modules, it is practical to drive the same current on all the modules simultaneously and obtain the voltage generated by each module at the specific operating conditions. Then, it is only needed to add up the voltages to obtain the voltage of the PV string for each current value.

4.4 Conclusions

Temperature of the PV module has a major impact on the voltage and, accordingly, on the produced electric power of the module. In addition, increase in the operating temperature is related to several failure or degradation modes of PV modules. Accurate prediction of PV module temperature is thus important to understand performance, reliability and lifetime of PV modules.

A dynamic thermal model of PV modules has been proposed in this Chapter which considers the thermal mass of the module besides of all relevant climatic and site-specific conditions and heat transfer mechanisms. The thermal model is based on the non-steady state equation obtained by considering the total energy balance in the PV module. The main mechanisms of energy exchange between the PV module and its environment are modelled according to their first principle considerations, resulting in a time varying differential equation of the module temperature.

The thermal model proposed can be considered as a "lumped parameter" module heat balance. Such model has been chosen instead of a "distributed parameter" model in which both space and time form independent variables as it provides enough accuracy to conduct the research intended with TUT Solar PV Power Station Research Plant. Additionally, a "distributed parameter" model could not achieve any higher accuracy than the proposed model considering the current measurement system detailed in Chapter 3.

The electric simulation model presented is based on the well-known one-diode model that considers the parasitic effects of the series and shunt resistances. The model includes five parameters governing the mathematical equation that describes the I-V characteristic of PV modules. Furthermore, the effects of the protection bypass diodes have been considered so that the simulation of series-connected PV modules can be easily implemented.

A state of the art dynamic thermal model of PV modules has been developed and presented in this Chapter. However, several input parameters of the model cannot be exactly defined, which might introduce some inaccuracy to the results. Therefore, the accuracy of this model has been tested in the next Chapter jointly with a sensitivity analysis of the model on the input parameters to further improve it.

5 EXPERIMENTAL VERIFICATION OF THE SIMULATION MODELS

The fifth Chapter discusses the experimental verification of the previously presented simulation models as well as the inclusive thermal and electric simulation model. First, the accuracy of the dynamic thermal model is improved by analyzing the effect of several parameters on the performance of the model and finding an optimum set of values which ensures maximum accuracy. Then, the consistent operation of the dynamic model is verified through different seasons of the year.

The electric model is further developed by means of a sensitivity analysis of the parameters governing the model and the evaluation of the accuracy of the model through the normalized root mean square error (NRMSE) values calculated between the measured and simulated electrical characteristics. As a result, the accuracy of the model is improved at both high and low irradiance levels. Subsequently, the operation of the electric model for both a single PV module and a PV string is verified under static operating conditions.

Finally, the inclusive dynamic thermal and electric model is implemented for a single PV module and a PV string of six series-connected modules and its performance is verified under dynamic operating conditions during six to eight hours on twenty days.

The content of this Chapter has been already published in several journal and conference articles. Most of the Chapter is written based on the findings presented in (Torres Lobera and Valkealahti, 2013a), (Torres Lobera and Valkealahti, 2014a) and (Torres Lobera and Valkealahti, 2014b).

5.1 Dynamic Thermal Model

5.1.1 Overall Capability of the Initial Model

Most of the parameters used in the dynamic thermal model are measured atmospheric variables or parameters extracted from the manufacturer datasheet. They have been used as such for the model. However, some parameters and factors affecting the performance of the thermal model either cannot be measured or depend on the site-specific characteristics of the environment where the PV modules are located. These parameters were the absorptivity α and heat capacity C_{mod} of the PV module, fraction of diffuse

radiation defining clear sky condition k_{d}, wind speed adjustment coefficient w_{a} and roof absorptivity coefficient a_{r}.

The effect of parameters, which are not precisely known, to the PV module temperature have been analyzed by using two sets of measured data corresponding to three winter days (from March 13^{th} to 16^{th}, 2012) and three summer days (from June 13^{th} to 16^{th}, 2012). The winter and summer dates have been chosen in such way that the datasets contain data with clear sky, partially cloudy, and overcast conditions to ensure the accuracy of the thermal model for most of the climatic conditions. Preliminary studies indicated that the approach of analyzing three days is sufficient to evaluate the accuracy of the thermal model under, at least, two different environmental conditions (i.e. clear sky, overcast or partially cloudy sky). The root mean square error (RMSE) between the measured and simulated temperatures $RMSE_{\mathrm{T}}$ is used as an indicator of the precision of the model in this sensitivity analysis. It is calculated as:

$$RMSE_{\mathrm{T}} = \sqrt{\frac{1}{M}\sum_{\mathrm{i}=1}^{\mathrm{M}} \left(T_{\mathrm{m,i}} - T_{\mathrm{s,i}}\right)^2}, \tag{5.1}$$

where M is the number of time steps in the simulation, and $T_{\mathrm{m,i}}$ and $T_{\mathrm{s,i}}$ are the measured and simulated module temperatures at time step i, respectively. It must be noted that during the winter test period the roof and ground were covered by snow but the PV module was clean of snow. It is also important to mention that the PV module was in open circuit conditions during the simulation periods in order to ensure that no power is generated and all the energy absorbed by the module is either transmitted to the environment through the energy exchange mechanisms described previously, or stored in the module causing a temperature change according to Equation 4.1.

The starting point of the sensitivity analysis is the state of the art parameter values in the literature. Therefore, the initial values of the studied parameters are either based on previous work of other authors (α), calculated theoretically based on the material properties of the PV modules (C_{mod}) or considered to have minimum initial effect to the performance of the model (w_{a} and a_{r}). The fraction of diffuse radiation k_{d} is a particular case since it has not been used earlier for discerning between clear sky and overcast conditions. Yet, its contribution to the performance of the model cannot be omitted. The initial values of the studied parameters are shown in Table 5.1. The performance of the thermal model with these reference values is illustrated in Figures 5.1 and 5.2 for winter and summer test periods with $RMSE_{\mathrm{T}}$ values of 1.18 and 3.77 °C, respectively.

In Figures 5.1 and 5.2, a better performance of the model for the winter period is clearly shown than for the summer period, in which the simulated daytime module temperature is lower than the measured temperature. The main contributions to such a

Table 5.1: Initial reference values and optimal parameter values for the thermal simulation model of TUT solar PV power station research plant.

Parameter	Reference value	Optimal Value
α	0.95	0.95
C_{mod} (J/K)	18936.00	21000.00
k_{d}	0.70	0.85
w_{a}	1.00	0.50
a_{r} ($\mathrm{m^2K/W}$)	0.00	0.08

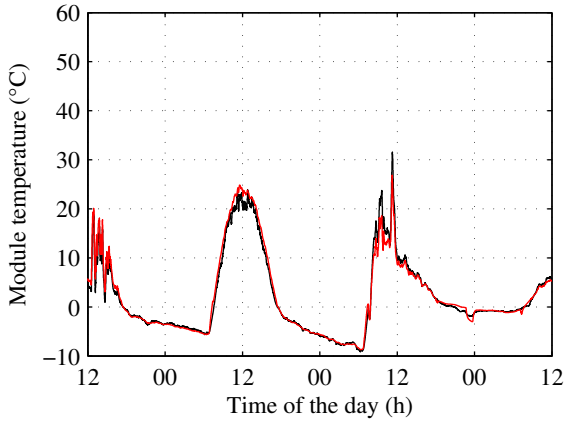

Figure 5.1: Measured module temperatures (black line) of PV module 20 during the three day winter period and simulated temperatures (red line) using the initial parameter values in Table 5.1.

large error ($RMSE_{\mathrm{T}} = 3.77$ °C) are that the roof temperature is considered to be the ambient temperature and the direction of the wind has not been taken into account in the convective losses. The effect of these factors and also the impact of the other three parameters α, C_{mod} and k_{d} on the dynamic thermal model performance are analyzed in the following sub-subsections.

Additionally, a systematic error in module temperature prediction occurs in the evenings during the summer period. The reason for this error is that after 18 o'clock the Sun starts to shine on the backside of the PV module heating it up. However, the sensor measuring the incoming solar radiation mounted with the same orientation and tilt as the PV module does not measure the incoming direct part of solar radiation to the backside. This incident radiation is a key input parameter for the simulation model and, therefore, leads to a systematic error in the predicted module temperature during the evenings. Actually Figure 5.3 demonstrates this matter even more explicitly. Just around 18 o'clock the solar radiation received by the tilted PV module drops sharply

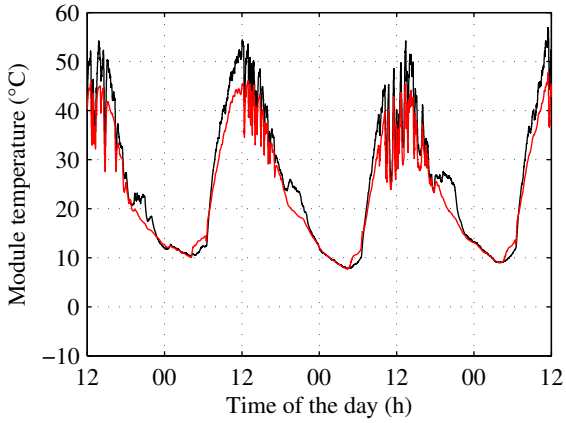

Figure 5.2: Measured module temperatures (black line) of PV module 20 during the three day summer period and simulated temperatures (red line) using the initial parameter values in Table 5.1.

but the solar radiation on a horizontal surface decreases more gradually until the sunset after 22 o'clock. This means that the Sun shines on the back of the PV modules during evening time heating them for several hours until sunset. This incidence occurs during late spring and summer in Finland. It is also important to remark that no self-shading issues are related to the PV module utilized in the simulations included in this Section.

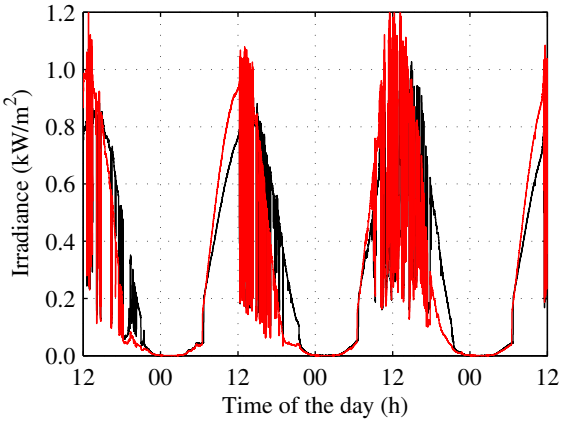

Figure 5.3: Measured incoming solar radiation on the horizontal plane (black line) and on the tilted PV module plane (red line) during the summer period.

Thus far the $RMSE_{\mathrm{T}}$ values calculated over 24 hours of a day have been presented as an indicator of the precision of the model for the winter and summer periods. However,

only the daytime from 6 o'clock to 18 o'clock is relevant from the power production point of view for fixed PV generator installations, such as in TUT. Furthermore, computing the evening hours in late spring and summer time does not seem to be a proper solution due to the aforementioned systematic error in module temperature prediction. Therefore, the input parameters have been optimized based on the daytime measurements to give the best PV module temperature prediction.

The set of best parameter values can be obtained by means of a sensitivity analysis by studying independently the effect of each parameter on the accuracy of the simulation model ($RMSE_{\mathrm{T}}$). The analysis also provides information about the importance of each parameter to the accuracy of the simulation model. The obtained optimal set of parameter values jointly with the initial set of reference values are presented in Table 5.1.

5.1.2 Sensitivity Analysis

This subsection includes the sensitivity analysis of the simulation model to provide a more complete understanding on different factors affecting to the PV module temperature. The sensitivity analysis is carried out by comparing the effect of each parameter at a time to the model accuracy. The daytime $RMSE_{\mathrm{T}}$ values between the simulated and measured temperatures are calculated for winter and summer periods by varying the value of the parameter under evaluation. The rest of the parameters are kept at their optimum values. In this way a parameter value was obtained corresponding to the minimum $RMSE_{\mathrm{T}}$.

Absorptivity of the PV module

The absorptivity of the PV module in Equation 4.1 determines the amount of energy absorbed by the module of the total incoming solar energy. It is a function of the orientation and configuration of the module, and absorptive and reflective properties of the PV module materials. In practice, the absorptivity also depends on the Sun position and the level of solar radiation but it is normally simplified as a constant value. The effect of the absorptivity on $RMSE_{\mathrm{T}}$ is illustrated in Figure 5.4 during the winter and summer test periods.

In Figure 5.4, it can be observed that the absorptivity would be slightly smaller during winter time than during summer time with minimum $RMSE_{\mathrm{T}}$ values being at 0.90 and 0.95, respectively. Adjustment of the PV module absorptivity to its optimum value for the winter period would improve the simulation accuracy by some 0.3 °C in winter time but it would also decrease the accuracy in summer time by some 0.6 °C. Therefore, 0.95 is considered to be the optimal overall annual absorptivity. One possible explanation for the slight differences in trends of $RMSE_{\mathrm{T}}$ for summer and winter could be the fact that the absorptivity is dependent on the Sun position and level of irradiance.

The average Sun position during winter is considerably lower than during summer in Finland. Moreover, the average irradiance received by the PV module during daytime for the winter and summer periods is 290.1 and 547.6 W/m^2, respectively. According to Schott (1985) absorptivity reduces with decreasing incident solar radiation (e.g., at dawn and dusk) in line with these findings.

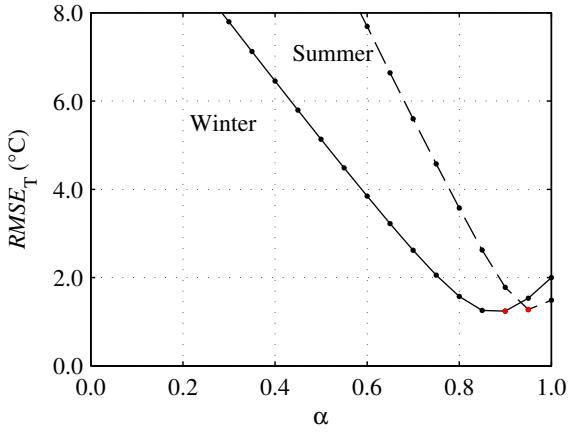

Figure 5.4: $RMSE_{\mathrm{T}}$ of the simulated module temperature with respect to the measured module temperature as a function of the absorptivity of the PV module during the winter and summer periods. The minimum values of $RMSE_{\mathrm{T}}$ are marked with red dots.

Heat capacity of the PV module

The heat capacity of a PV module characterizes the amount of energy needed for increasing the module temperature. A module with low heat capacity will experience higher temperature variations with changing atmospheric conditions than a module with high heat capacity. Heat capacity of PV modules is defined by the material properties compounding the module and has a fixed value. However, it was problematic to define heat capacity for the PV modules of TUT solar PV power station research plant due to lack of precise material properties since manufacturers do not typically provide this information for commercial reasons. Therefore, it seemed necessary to check the sensitivity of the module temperature also on this parameter. The accuracy of the predicted module temperature is shown in Figure 5.5 as a function of the C_{mod} for the winter and summer test periods.

PV module temperature does not seem to be very sensitive to the heat capacity (Figure 5.5) as far as it is of the right order of magnitude. In winter time the simulation models actually seem to be quite insensitive to the correct value of heat capacity, but in summer time substantial underestimation of the heat capacity will lead to major errors in

calculated module temperatures. The reason for this is the higher temperature difference $T_{\mathrm{mod}} - T_{\mathrm{air}}$ due to higher level of solar radiation in summer than in winter. Observing Figure 5.5, it can be stated that the initial heat capacity was slightly too small. The minimum $RMSE_{\mathrm{T}}$ values for the whole year are found between the heat capacities of 20 and 22 kJ/K.

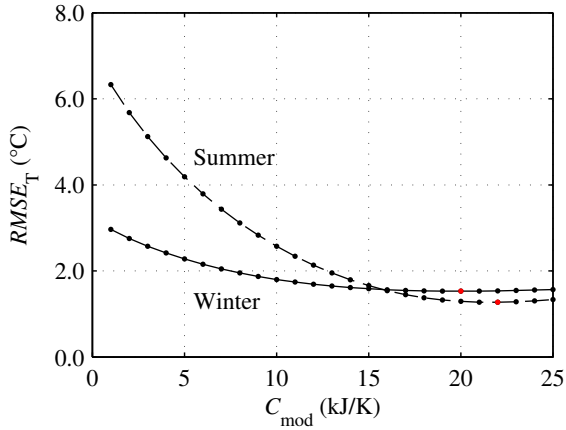

Figure 5.5: $RMSE_{\mathrm{T}}$ of the simulated module temperature with respect to the measured module temperature as a function of the heat capacity of the PV module during the winter and summer periods. The minimum values of $RMSE_{\mathrm{T}}$ are marked with red dots.

Fraction of diffuse radiation

The fraction of diffuse radiation k_{d} is an index that measures the amount of diffuse solar radiation from the total incoming solar radiation. As explained in Chapter 4, it can be used as a tool to discern between clear sky and overcast conditions to estimate the temperature of the sky. Low values of k_{d} indicate clear sky conditions ($T_{\mathrm{sky}} = T_{\mathrm{air}} - 20$ K), and high values indicate overcast conditions ($T_{\mathrm{sky}} = T_{\mathrm{air}}$). Somewhere in between there is a value of k_{d}, which can be used to separate between clear sky and overcast conditions. The effect of varying the limit value of k_{d} on the $RMSE_{\mathrm{T}}$ is depicted in Figure 5.6 for the winter and summer periods.

In Figure 5.6, $RMSE_{\mathrm{T}}$ increases when k_{d} limit decreases below 0.4 or increases above 0.9. This is plausible because at low k_{d} values only clear sky conditions occur and, therefore, the limit should be larger than 0.4. Accordingly, high k_{d} values correspond to overcast conditions and the limit should be below 0.9. The best fit between the simulated and measured temperatures takes place when k_{d} limit is 0.85. One should also note that the model accuracy improves considerably from 2.7 to 1.3 °C in summer time, when the sky temperature is taken into account correctly.

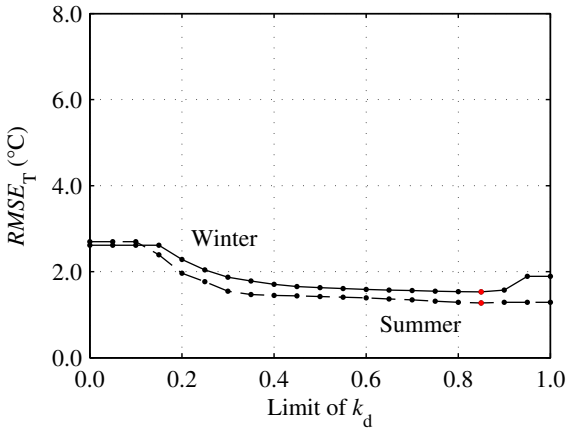

Figure 5.6: $RMSE_T$ of the simulated module temperature with respect to the measured module temperature as a function of the k_d limit for clear sky and overcast conditions during the winter and summer test periods. The minimum values of $RMSE_T$ are marked with red dots.

Wind speed adjustment coefficient

Wind sensors are typically placed to measure the local overall wind speed in the PV facility areas. The impact of the wind speed and direction on the forced convective losses depends on the mounting system of the PV modules (free standing on a rooftop, integrated in the facade of a building, etc) and the environment, and the use of a wind speed adjustment coefficient w_a has been considered in Equation 4.14.

The wind speed and direction are measured by an ultrasonic wind sensor at the highest point of the TUT solar PV power station research plant (Torres Lobera and Valkealahti, 2012). The PV modules are mounted with a tilted angle of 45° on mounting racks that cover the back plates of the modules, shielding them from north winds. Therefore, the wind speed adjustment coefficient is used to approximate the wind speed reduction caused by the mounting racks and Equation 4.14 turns into

$$Re = \frac{L}{\rho v} v_w w_a. \tag{5.2}$$

In this study, only a simple basic adjustment is applied for the wind speed. The wind speed adjustment coefficient w_a is set to be 1 for winds blowing towards north, north-east, north-west, east and west and a value between 0 and 1 has been set for winds blowing towards south, south-east and south-west providing the smallest $RMSE_T$ for the simulated temperature. The effect of the wind speed adjustment coefficient on the error between the predicted and measured module temperatures for the winter and summer periods is illustrated Figure 5.7.

During the winter period, the temperature of the PV module does not depend strongly on the speed of north winds and values of w_a from 0.4 to 1 provide almost the same $RMSE_T$ values. This is plausible because temperature rise of the PV module due to incident solar radiation is small in winter time with respect to ambient air temperature. However, the PV module temperature is quite sensitive to the adjustment coefficient value during summer time and the best simulation accuracy is obtained with $w_a = 0.5$. This indicates that the installation on the roof and the used mounting racks that cover the back plates of the PV modules considerably reduce forced convective losses on the backside.

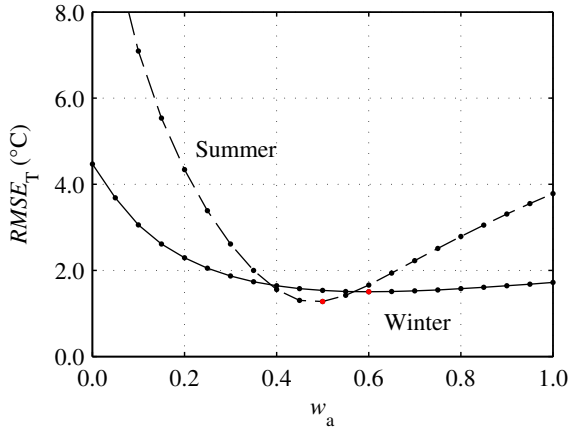

Figure 5.7: $RMSE_T$ of the simulated module temperature with respect to the measured module temperature as a function of the wind adjustment coefficient for clear sky and overcast conditions during the winter and summer test periods. The minimum values of $RMSE_T$ are marked with red dots.

Roof absorptivity coefficient

The roof temperature T_{roof} plays an important role in the long-wave radiative losses of the PV module in the same way as the sky temperature. During cloudy days the increase in the roof temperature with respect to the ambient temperature is not that large due to the low level of solar radiation and T_{roof} can be approximated to be equal to T_{air} with good accuracy. This approximation would also be acceptable for buildings designed with green roofs which do not absorb as much solar energy as black-surfaced rooftops. Therefore, the ambient air temperature T_{air} can serve as a reasonable approximation for ground temperature for open field PV power plant installations.

Generally speaking, the roof temperature is demanding to approximate accurately since it would require the same type of energy balance analysis as the temperature of

the PV modules. However, such accuracy is not required for the present work and a simpler approach has been taken. The temperature of the roof in steady-state can be approximated by the expression:

$$T_{\mathrm{roof}} = T_{\mathrm{air}} + a_{\mathrm{r}} G_{\mathrm{h}}, \tag{5.3}$$

where a_{r} is the roof absorptivity coefficient and G_{h} is the horizontal incoming total solar radiation. The effect of a_{r} on the accuracy of the predicted module temperature is depicted in Figure 5.8.

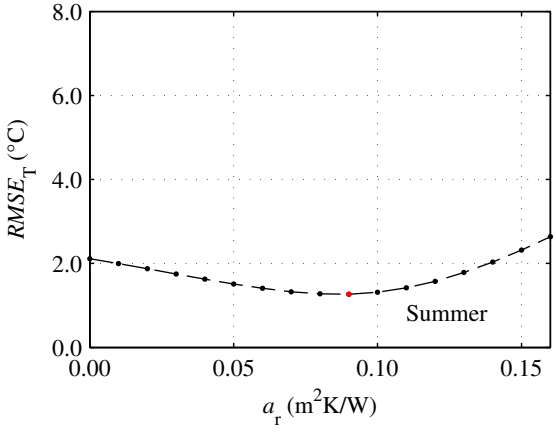

Figure 5.8: $RMSE_{\mathrm{T}}$ of the simulated module temperature with respect to the measured module temperature as a function of the roof absorptivity coefficient for clear sky and overcast conditions during the summer test period. The minimum value of $RMSE_{\mathrm{T}}$ is marked with a red dot.

During winter time and part of spring, the ground and roofs of buildings in the Nordic countries are covered by snow. The existence of snowpack keeps the snow temperature lower than the roof temperature would be under the solar radiation without snow coverage. The snow reflects most of the sunlight and all absorbed energy serves to melt the snow instead of increasing its temperature over 0 °C. Therefore, the roof temperature is considered to be 0 °C in the simulations during the existence of snow and the roof absorptivity coefficient has no effect on the predicted module temperature.

During the summer period, the roof absorptivity affects the long wavelength heat transfer between the PV module and the roof surface as shown in Figure 5.8. However, the module temperature does not depend strongly on the roof absorptivity, i.e., the shape of the curve around the minimum in Figure 5.8 is quite flat. The best simulation accuracy was obtained with $a_{\mathrm{r}} = 0.08$ m^{2}K/W, which corresponds to a roof temperature rise of the order of 60 to 70 °C for summer day radiation levels. However, the temperature prediction improves with around 1 °C in summer time by including the warming up of

the roof (by increasing a_r from 0 to 0.08 m^2K/W).

Overall capability of the final model

The performance of the thermal model using the optimal parameter values of Table 5.1 is illustrated in Figures 5.9 and 5.10 for the winter and summer periods. The new $RMSE_T$ values of the simulation model temperatures are 1.12 °C and 1.78 °C for the winter and summer periods, respectively. A major improvement has taken place compared to the $RMSE_T$ values of 1.18 °C and 3.77 °C obtained by the initial parameter values of Table 5.1.

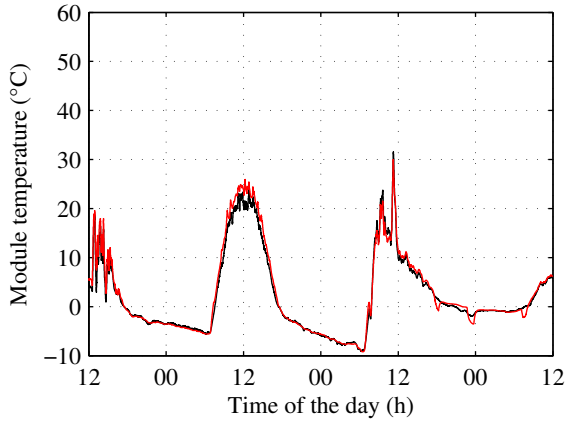

Figure 5.9: Measured module temperatures (black line) of PV module 20 during the three day winter period and simulated temperatures (red line) using the optimal parameter values in Table 5.1.

As can be seen in Figure 5.9, the agreement between the simulated and measured PV module temperatures is very good during the winter period. Only small deviations take place between the simulated and measured temperatures for short periods of time. Most of the time the two lines are on top of each other. During summer time the temperature deviations are larger partly due to the more volatile environment (climate) as illustrated in Figure 5.10. However, during the night and daytime the model seems to be in good agreement with measured temperatures. The only major deviations take place in evenings when the measured PV module temperatures are systematically higher than the simulated temperatures as explained in Section 5.1.1. The instantaneous error of the predicted module temperature during the summer period is shown in Figure 5.11. The error is stable and small during night time and more volatile and slightly larger in daytime. During evenings the error is considerably larger all the time in accord with Figure 5.10.

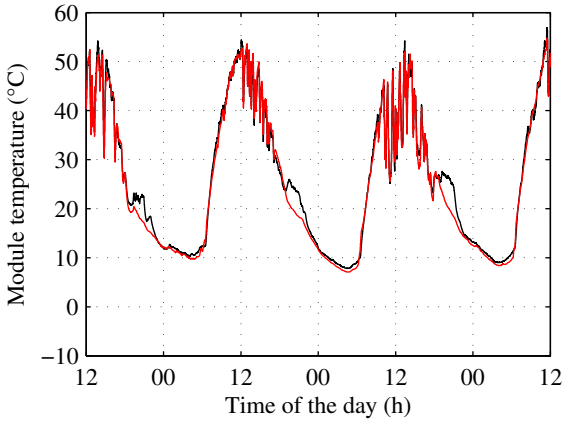

Figure 5.10: Measured module temperatures (black line) of PV module 20 during the three day summer period and simulated temperatures (red line) using the optimal parameter values in Table 5.1.

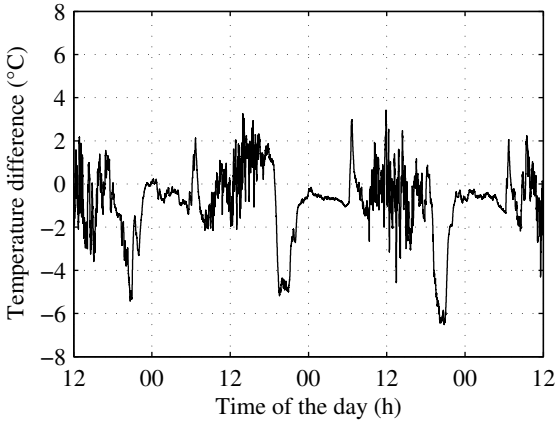

Figure 5.11: Difference between the predicted and measured module temperatures during the summer period.

The $RMSE_{\mathrm{T}}$ values calculated for different daily computing hours are included in Table 5.2 for the winter and summer periods to demonstrate the effect on model accuracy. It is evident that the optimised parameter values give more accurate PV module temperature predictions than the initial values for the test periods. This is, of course, a self-evident result for the test period, but the improvements are considerable, especially for the summer period. It is also notable that the daytime temperature prediction for summer period using optimized parameter values is almost as accurate as the prediction for the winter period.

Table 5.2: The error of simulated all-day and daytime module temperatures for the winter and summer test periods using the initial and optimised input parameter values.

Period	Computing hours	$RMSE_{\mathrm{T,Initial}}$	$RMSE_{\mathrm{T,Optimum}}$
Winter	0 - 24 h	1.18 °C	1.12 °C
Winter	6 - 18 h	1.63 °C	1.53 °C
Summer	0 - 24 h	3.77 °C	1.78 °C
Summer	6 - 18 h	4.76 °C	1.27 °C

5.1.3 Experimental Verification

It is actually self-evident that the optimized thermal model used for fitting the input parameter provides better results for the test periods than the initial theoretical values. Therefore, it is essential to test the performance of the model with different measurement data. For that reason, simulations have been performed for a new three-day period from May 20$^{\mathrm{th}}$ to 23$^{\mathrm{rd}}$, 2012 (spring period) and for a case of 91 consecutive days during summer 2012 to confirm the accuracy of the optimized thermal model (Table 5.1). The selected three day period includes datasets corresponding to non-homogenous atmospheric conditions in terms of sky conditions, irradiance, wind speed and direction, etc. It also serves as an easy way for comparing with earlier simulations (Figures 5.9 and 5.10). On top of that, the analysis of the whole measurement data of summer 2012 serves as the final proof for the model performance.

The performance of the optimized thermal model is illustrated in Figure 5.12 for the spring period obtaining an all-day $RMSE_{\mathrm{T}}$ of the simulated temperature of 1.39 °C. This error is well in line with the errors of the optimized thermal model for the winter and summer periods presented in Section 5.1.1 (Table 5.2). The instantaneous error between the predicted and measured module temperatures is depicted in Figure 5.13.

The major deviations between the simulated and measured PV module temperatures take place again in the evenings. The reason for this is the systematic error in the prediction of PV module evening temperature as explained already in Section 5.1.1. This is also a major reason for the bigger all-day $RMSE_{\mathrm{T}}$ of the simulated temperatures for summer than for spring and for spring than for winter. The daytime performance of the optimized thermal model for the spring period is better than the all-day performance, as expected, yielding a $RMSE_{\mathrm{T}}$ of 1.28 °C, which goes together with the summer accuracy. It seems to be evident, that the thermal model performs well around the year.

The calculated $RMSE_{\mathrm{T}}$ values are included in Table 5.3 for different computing times for the spring period as well as the fraction of time when the model accuracy (ΔT) is lower than 2 °C, between 2 and 3 °C and larger than 3 °C.

To ensure the accuracy and performance of the dynamic thermal model a set of

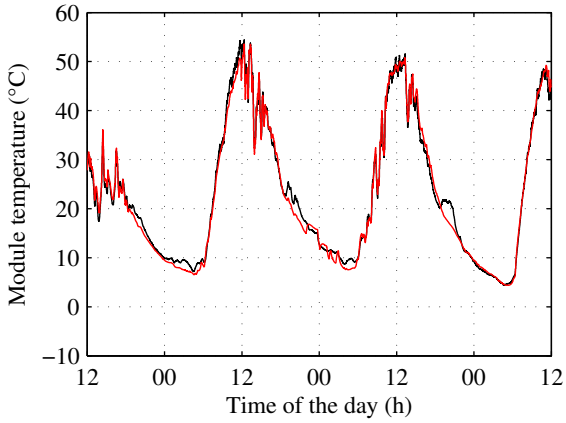

Figure 5.12: Measured (black line) and simulated (red line) module temperatures for the spring period using the optimal parameter values of Table 5.1.

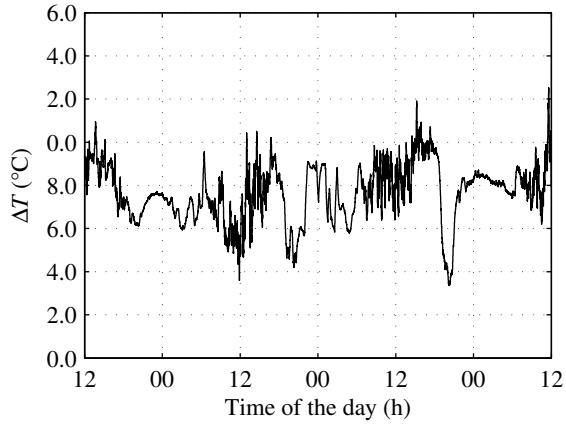

Figure 5.13: Difference between the predicted and measured module temperatures during the spring period.

atmospheric data corresponding to 91 consecutive days from May 23$^{\text{rd}}$ to August 23$^{\text{rd}}$, 2012 with a sampling frequency of 1 Hz is used as an input for the thermal model. The daily daytime $RMSE_{\text{T}}$ values for the summer 2012 are shown in Figure 5.14. During 77 days out of 91 the daily $RMSE_{\text{T}}$ is below 2 °C. This is well in line with the results for the spring period in Table 5.3. The all-day and daytime $RMSE_{\text{T}}$ of the simulated temperatures for the summer period are 1.61 and 1.63 °C, respectively, as shown in Table 5.4. These values are in line with the values for the test period presented in Tables 5.2 and 5.3. 80 % of the time the simulated PV module temperature differs less than 2 °C

from the measured temperature and only a small fraction of time the difference is larger than 3 °C.

Table 5.3: $RMSE_{\mathrm{T}}$ and the fraction of time when the error of predicted PV module temperature ΔT is within certain limits for the spring test period.

Computing hours	$RMSE_{\mathrm{T}}$	$\Delta T \leq 2°\mathrm{C}$	$2°\mathrm{C} \leq \Delta T \leq 3°\mathrm{C}$	$\Delta T \geq 3°\mathrm{C}$
0 - 24 h	1.39 °C	87.4 %	8.4 %	4.2 %
6 - 18 h	1.28 °C	88.8 %	9.7 %	1.5 %

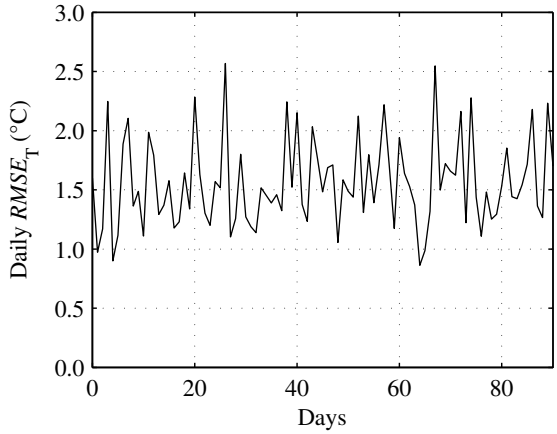

Figure 5.14: Daily daytime $RMSE_{\mathrm{T}}$ of the predicted module temperature for 91 days during summer 2012.

Table 5.4: $RMSE_{\mathrm{T}}$ and fraction of time when the error of predicted PV module temperature ΔT is within certain limits for 91 days during summer 2012.

Computing hours	$RMSE_{\mathrm{T}}$	$\Delta T \leq 2°\mathrm{C}$	$2°\mathrm{C} \leq \Delta T \leq 3°\mathrm{C}$	$\Delta T \geq 3°\mathrm{C}$
0 - 24 h	1.61 °C	82.0 %	12.5 %	5.5 %
6 - 18 h	1.63 °C	80.0 %	14.4 %	5.6 %

The PV modules are covered by snow for long periods during winter time. This prevents taking usable measurements and thus impedes comprehensive evaluation of the performance of the model during winter. However, the thermal model is expected to present similar accuracy in winter than in summer or spring.

The developed dynamic thermal simulation model of the PV module temperature seems to perform well. One must also note that the real temperature measurement accuracy in outdoor conditions is close to 1 °C so that the achieved accuracy is also the

practical achievable accuracy. On top of that, this dynamic thermal model will be used to simulate the TUT PV power plant electric power production capacity. An error of 2 °C in the predicted module temperature will lead to an error of less than 1 W in the available power. This accuracy is clearly enough for the foreseen research purposes.

5.2 Electric Model

The accuracy of the electric model is first improved for operation under non-ideal atmospheric conditions by analyzing the relative importance of the five parameters of the one-diode model through a sensitivity analysis. For that, a set of ten-day measurements has been utilized for PV module 19. Measurements of six to eight hours per day were conducted and contain clear sky, partially cloudy and cloudy overcast conditions. The solar radiation and module temperature measurements utilized as input for the electric simulation model have been taken at a sampling rate of 1 Hz. Accordingly, the *I-V* curves utilized to validate the accuracy of the model have been traced at a sampling rate of 1 curve per second. Each curve includes 1000 voltage and current points, which were registered in a time period of 200 ms.

The operation and accuracy of the electric model is then tested under static conditions for both a single PV module and a PV string of six series-connected modules. PV Module 19 and PV String 4 were selected from TUT solar PV power station research plant (Torres Lobera et al., 2013) for this evaluation. PV module 19 is tested under clear sky and cloudy overcast irradiance conditions. For the PV string, four partial shading conditions and one homogenous irradiance condition are exploited.

5.2.1 Sensitivity Analysis

The five parameters governing the one-diode model (Equation 4.26) are I_{ph}, I_{o}, R_{s}, R_{sh} and a. As explained in Section 4.3, these parameters can be extracted from the manufacturer's information by assuming a certain value of a. The parameter values obtained at STC are contained in Table 5.5 for the NAPS NP190GKg PV modules as well as the utilized temperature coefficients for current and voltage.

A lot of research has been conducted during the last years to model the electrical operation of PV cells and modules. However, the authors generally focus mainly on the accuracy of predicting the MPP current, voltage and power or of a few points of the *I-V* curves, mostly I_{SC} and V_{OC}. In this work, the accuracy of the whole forecasted *P-V* characteristic is evaluated by means of the normalized root mean square error calculated between the measured and simulated power curves ($NRMSE_{\mathrm{P}}$). The root mean square

Table 5.5: Parameter values of the simulation model for the NAPS NP190GKg PV modules under STC.

Parameter	Value
$I_{\mathrm{ph,STC}}$ (A)	8.01
$I_{\mathrm{o,STC}}$ (A)	9.07e-8
a	1.30
R_{s} (Ω)	0.33
R_{sh} (Ω)	353.12
K_{i} (A/K)	0.0047
K_{v} (V/K)	-0.124

error of the P-V curve is calculated as

$$RMSE_{\mathrm{P}} = \sqrt{\frac{1}{N}\sum_{\mathrm{i=1}}^{\mathrm{N}} \left(P_{\mathrm{m,i}} - P_{\mathrm{s,i}}\right)^2}, \tag{5.4}$$

where N is the number of measurement points in the P-V curves, and $P_{\mathrm{m,i}}$ and $P_{\mathrm{s,i}}$ are the measured and simulated powers in point i, respectively. Then, the $NRMSE_{\mathrm{P}}$ is calculated as

$$NRMSE_{\mathrm{P}} = \frac{RMSE_{\mathrm{P}}}{P_{\mathrm{max}}}, \tag{5.5}$$

where P_{max} is the measured maximum power in the P-V curve. This way of calculating the error between the simulated and measured curves permits to compare the accuracy of the model in the whole parameter range. This is essential, especially, in case of low irradiance levels or of non-ideal operating conditions such as partial shading caused by clouds and buildings.

A set of ten days of measurements is utilized to assess the overall capability of the electrical model. Accordingly, the measured irradiances and module temperatures have been used as input for the model and the I-V characteristics have been simulated by the second and compared to the measured curves to obtain the $RMSE_{\mathrm{P}}$ and $NRMSE_{\mathrm{P}}$. The calculated $RMSE_{\mathrm{P}}$ and $NRMSE_{\mathrm{P}}$ values for the electrical model implemented with the parameters included in Table 5.5 are shown in Figure 5.15 as a function of the measured irradiance. As can be observed in Figure 5.15(a), the $RMSE_{\mathrm{P}}$ between the measured and simulated P-V curves increases with irradiance. This is expected since the power produced by the PV module rises closely proportional to the absorbed solar radiation, leading to larger errors in the predicted curves. The $NRMSE_{\mathrm{P}}$ in Figure 5.15(b), in contrast, shows a slight increase with increasing irradiance at high irradiances but high increase with decreasing irradiance at low irradiances. This is in line with the hypothesis

that the simulation model performs more accurately near STC. The average values of $RMSE_{\mathrm{P}}$ and $NRMSE_{\mathrm{P}}$ are 2.27 W and 2.15 %, respectively.

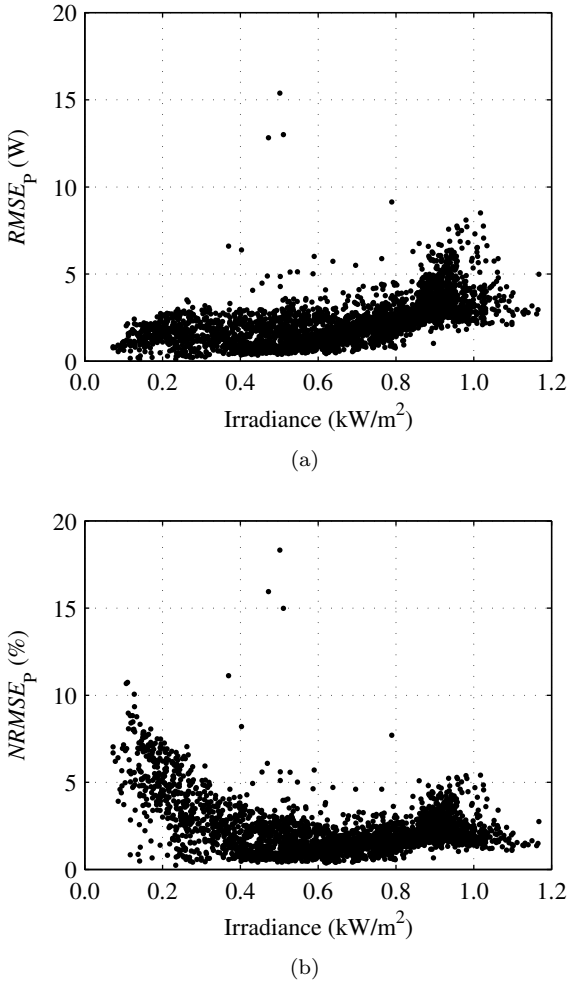

Figure 5.15: (a) $RMSE_{\mathrm{P}}$ and (b) $NRMSE_{\mathrm{P}}$ calculated between the measured and simulated P-V curves as a function of the absorbed irradiance for a single module during ten days in August, September and October, 2013. The results have been down-sampled to 1 sample per minute to facilitate the reader noticing the trends of variation of $RMSE_{\mathrm{P}}$ and $NRMSE_{\mathrm{P}}$ with respect to irradiance.

According to Siddiqui et al. (2013), a sensitivity analysis can be implemented to identify the relative importance of the five parameters on the error of the predicted I-V, or P-V, characteristics. Masi et al. (1999) described how the evaluation of the normalized sensitivity coefficients (NSC) allows comparing parameters whose order of magnitude may

be significantly different. This is precisely the case of the electrical model in which, e.g., I_{ph} and I_{o} differ by an order of 10^8 under STC. The normalized sensitivity coefficients for each parameter are calculated as

$$NSC_{\mathrm{P,i}} = \frac{\Delta P_{\mathrm{MPP}}}{P_{\mathrm{MPP}}\left(X_{\mathrm{i,nom}}\right)} \frac{X_{\mathrm{i,nom}}}{\Delta X_{\mathrm{i}}}, \tag{5.6}$$

where $X_{\mathrm{i,nom}}$ is the nominal value (i.e. under STC) and ΔX_{i} is the increment of the parameter i, respectively. P_{MPP} is the MPP power for $X_{\mathrm{i,nom}}$ and ΔP_{MPP} is the increment in MPP power experienced by changing the parameter i.

The obtained normalized sensitivity coefficients under STC conditions are included in Table 5.6 for increments of 50 % of the analyzed parameters, i.e. modifying the nominal value of the parameters by ±25 %. It is easy to notice that the predicted power is more sensitive to the ideality factor and the photocurrent under STC than to the rest of the parameters whose relative effect is minor.

Table 5.6: Normalized sensitivity coefficients for MPP power in STC. $P_{\mathrm{MPP}}(X_{\mathrm{nom}}) = 189.89$ W.

Parameter (X_{i})	$X_{\mathrm{i,nom}}$	ΔX_{i}	ΔP_{MPP} (W)	$NSC_{\mathrm{P,i}}$
$I_{\mathrm{ph,STC}}$ (A)	8.01	4.00	93.40	0.98
$I_{\mathrm{o,STC}}$ (A)	9.07e-08	4.53e-08	6.72	0.07
a	1.30	0.65	102.94	1.08
R_{s} (Ω)	0.33	0.17	8.96	0.09
R_{sh} (Ω)	353.12	176.56	0.99	0.01

As mentioned previously, the accuracy of the electrical model decreases with decreasing level of irradiance, i.e., when operating away from STC (Figure 5.15(b)). In order to verify whether the operating conditions affect the NCS_{P}, the sensitivity analysis is repeated for a range of irradiance and module temperature values. The NSC_{P} are calculated for the five parameters at different irradiance levels between 200 and 1000 W/m^2, and for different module temperatures between -20 and +60 °C. The variation of the normalized sensitivity coefficients is shown in Figure 5.16 as a function of the absorbed irradiance and module temperature.

As can be seen in Figure 5.16(a), the electrical model becomes more sensitive to changes in the photocurrent with decreasing irradiance, while the effect of the ideality factor becomes less important. The model is less sensitive to changes in the dark saturation current and series resistance and the sensitivity decreases with decreasing irradiances. On the contrary, the electrical model becomes considerably more sensitive to the shunt resistance with decreasing irradiances than in STC. The sensitivity of the electrical model to changes of the input parameter values is almost independent of the

module temperature as can be seen in Figure 5.16(b).

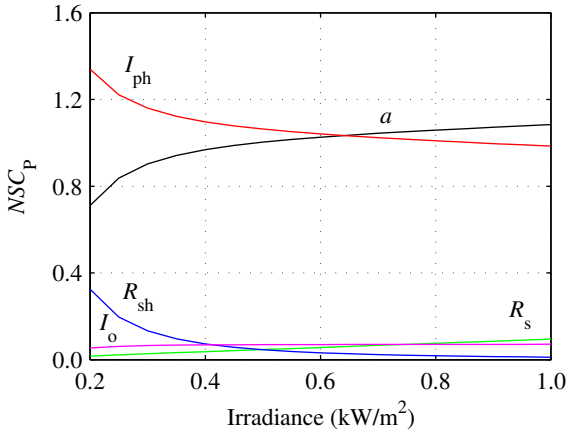

(a)

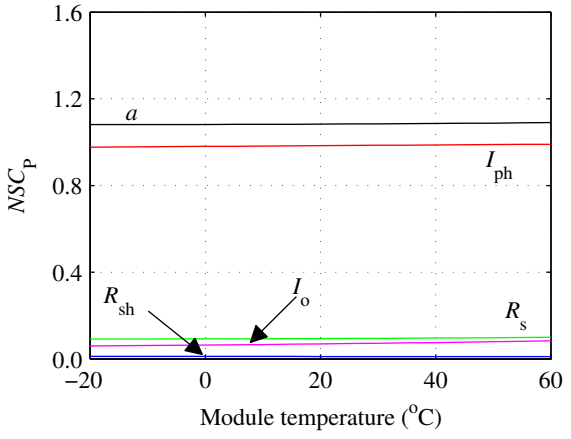

(b)

Figure 5.16: Variation of the normalized sensitivity coefficients, calculated for increments of 50 % of the analyzed parameters, as a function of (a) the absorbed irradiance and (b) the module temperature.

Based on these findings, it seems necessary to consider carefully the values of the ideality factor, photocurrent and shunt resistance to improve the accuracy of the electrical model at low irradiances. The photocurrent is, in fact, closely proportional to the solar radiation as explained in Section 4.3, thus its value already varies with irradiance. As pointed out also in Section 4.3, the ideality factor should be a constant value between 1 and 1.5 for Silicon PV cells according to Villalva et al. (2009a). A value of a of 1.3 has been found to provide accurate results for the PV modules used in this work based on

a comparison of simulation results with a large amount of measurements under different operating conditions. Any attempt to modify a as a function of the operating conditions has proven to increase the average $RMSE_{\mathrm{P}}$ and $NRMSE_{\mathrm{P}}$ obtained which implies that 1.3 is an adequate value for a regardless of the operating temperature and solar radiation absorbed. De Soto et al. (2006) notes that the shunt resistance seems to change with the absorbed solar radiation regardless of the PV material of the cell and Schroder (1998) specifies that it is approximately inversely proportional to I_{SC}, i.e. to the solar radiation absorbed, at low irradiance levels. Therefore the empirical equation proposed to adjust the shunt resistance is

$$R_{\mathrm{sh}} = R_{\mathrm{sh,STC}} \left(\frac{G_{\mathrm{STC}}}{G} \right). \tag{5.7}$$

The performance of the electric model after implementing Equation 5.7 is illustrated in Figure 5.17. In it, the calculated $RMSE_{\mathrm{P}}$ and $NRMSE_{\mathrm{P}}$ for a single PV module during the same simulation time as in Figure 5.15 are represented as function of the measured irradiance. As can be observed, there is a major improvement in the accuracy of the model at low irradiance levels. The $RMSE_{\mathrm{P}}$ values (Figure 5.17(a)) at irradiance levels below 600 W/m^2 are clearly lower than in the initial results shown in Figure 5.15(a). The improvement in the accuracy of the model is even easier to notice in Figure 5.17(b) where the $NRMSE_{\mathrm{P}}$ values at low irradiance levels are significantly smaller than in Figure 5.15(b). The new averages for $RMSE_{\mathrm{P}}$ and $NRMSE_{\mathrm{P}}$ are 2.12 W and 1.89 %, respectively. Compared to the initial values of 2.27 W and 2.15 %, the improvement in accuracy is considerable.

5.2.2 Experimental Verification

The operation and accuracy of the electric simulation model was tested under static environmental conditions both for a single PV module and a PV string of six series-connected modules.

PV module 19 was measured under natural balanced irradiance conditions on a clear sky and cloudy overcast day. The measured and simulated I-V and P-V characteristics of a single module operating under high and low irradiance conditions are show in Figure 5.18 to demonstrate the accuracy of the utilized model under different operation conditions for the whole voltage range. The agreement is excellent and actually perfect when the limitations of the used electric model are acknowledged.

For the PV string, four partial shading conditions and one homogenous irradiance condition have been exploited. PV modules were operating either under clear sky radiation conditions or under fully shaded conditions receiving only diffuse radiation. The partial shading was caused by a built structure during the measurements and, therefore,

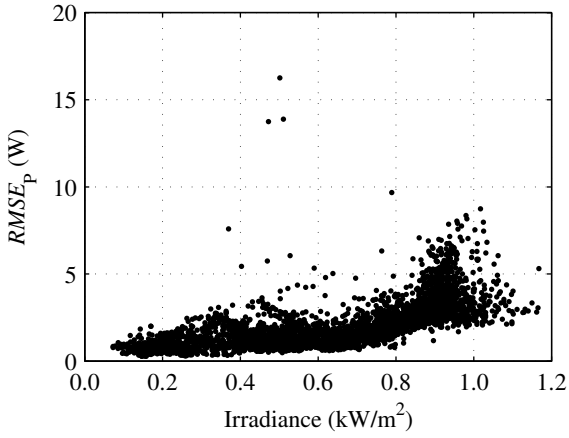

(a)

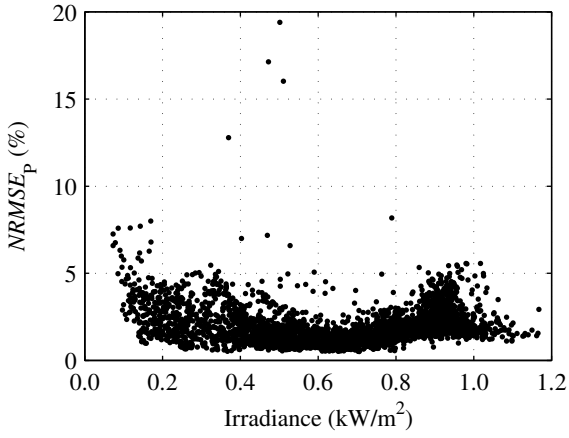

(b)

Figure 5.17: (a) $RMSE_P$ and (b) $NRMSE_P$ calculated between the measured and simulated P-V curves as a function of the absorbed irradiance for a single module during ten days in August, September and October, 2013. The results have been down-sampled to 1 sample per minute to facilitate the reader noticing the trends of variation of $RMSE_P$ and $NRMSE_P$ with respect to irradiance.

the PV modules can be considered to operate, in practice, under static conditions at the moments of the measurements.

To confirm that the electric model operates correctly for PV strings including the bypass diodes, the operation of String 4 was simulated under several partial shading conditions and compared with the measured electrical characteristics. The effect of partial shading on the I-V and P-V characteristics caused by a building structure is illustrated

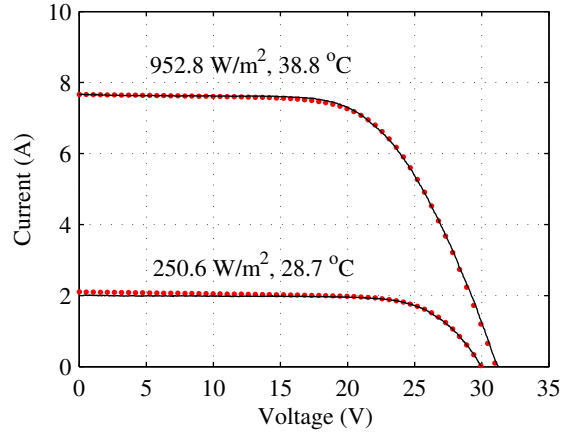

(a)

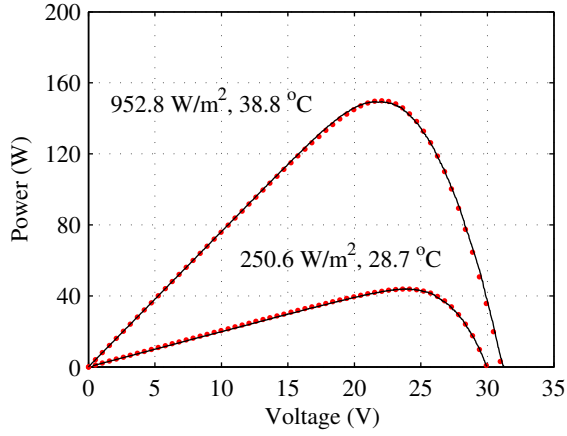

(b)

Figure 5.18: Measured (blue lines) and simulated (red dots) electrical (a) *I-V* and (b) *P-V* characteristics of a single PV module operating under high and low irradiance conditions.

in Figure 5.19 for four partial shading conditions along with one homogenous clear sky irradiance condition. The agreement between the simulated and measured curves is again excellent. The irradiances and module temperatures at both ends of String 4 measured by sensors S5 and S6 are comprised in Table 5.7 at the moments when the electrical measurements were taken. Measurements 1 to 4 correspond to the operation under partial shading conditions of the PV string with two, three, four, and five non-shaded modules, respectively. Measurement 5 shows the operation of the string under homogenous non-shaded irradiance conditions. The irradiances and temperatures of all the shaded modules were assumed to be equal during the simulations, and, correspondingly, the ir-

radiances and temperatures of all the non-shaded modules were assumed to be equal. This assumption may not be entirely correct, especially for the module temperatures. Irrespective of that, a good agreement exists between simulated and measured electrical characteristics.

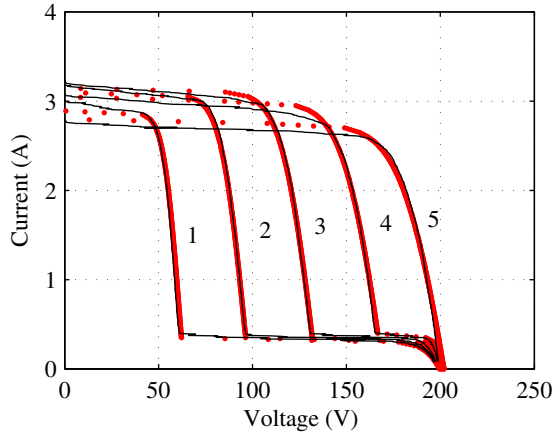

(a)

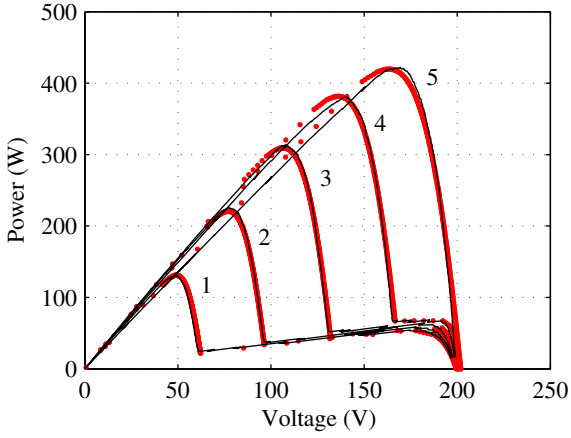

(b)

Figure 5.19: Measured (black lines) and simulated (red dots) electrical (a) *I-V* and (b) *P-V* characteristics of the String 4 of six series-connected PV modules operating under partial shading conditions on December 4$^{\text{th}}$, 2012. Irradiances and module temperatures measured with sensors S5 and S6 at the corresponding moments are presented in Table 5.7.

Under partial shading conditions caused by the building structure, each of the shaded *I-V* and *P-V* curves shown in Figure 5.19 can be divided into two different areas. In the first area, bypass diodes protecting groups of shaded cells conduct current and short

Table 5.7: Irradiances received by the PV modules and module temperatures during December 4^{th}, 2012 measured with sensors S5 and S6 located at both ends of String 4 at the instants when electrical characteristics in Figure 5.19 were measured.

Measurement	Sensor S5		Sensor S6	
	G (W/m^2)	T_{mod} (°C)	G (W/m^2)	T_{mod} (°C)
1	425.9	-1.58	30.5	-17.42
2	439.9	0.73	31.2	-17.37
3	438.4	3.71	32.5	-16.97
4	424.0	3.19	33.3	-16.48
5	386.6	1.93	353.8	-5.85

out the circuits of groups of 18 PV cells. In the second area, higher voltages appear since the bypass diodes protecting the groups of non-shaded cells are reverse biased and the characteristic of the string is dominated by the series-connected shaded cells. The simulations illustrated in Figure 5.19 endorse the correct operation of the electric model in case of series-connected PV modules since the model follows the measured electrical characteristics closely under all irradiance conditions. The small errors visible in Figure 5.19 are mostly due to the limitations of the measuring system.

5.3 Integrated Simulation Model

5.3.1 Implemented Model and Studied System

A complete inclusive simulation model has been built using Matlab Simulink software by combining together both electric and dynamic thermal models of the PV modules optimized and validated in Sections 5.1 and 5.2, respectively. The temperature of each module is calculated using an iteration time step of 1 second. A complete *I-V* curve is then calculated for each time step and each module and the MPP values are extracted from those curves. The environmental parameters needed as input to the integrated simulation method are the incident irradiance in the plane of the PV modules, the ambient temperature, the global and diffuse solar radiation on the horizontal plane, and the wind speed and direction. These parameters are measured by the TUT solar PV power station research plant detailed in Chapter 3.

The operation and accuracy of the implemented simulation model has been tested under dynamic operating conditions both for a single PV module and a PV string of six series-connected modules. PV Module 19 and PV String 4 were selected from TUT solar PV power station research plant (Torres Lobera et al., 2013) for this evaluation. Two sets of ten-day measurements have been utilized for the PV module 9 and for the PV string 4. Measurements ranging from six to eight hours per day were conducted during

20 days in the summer and autumn of 2013. They contain clear sky, partially cloudy and cloudy overcast conditions. The environmental measurements utilized as input for the integrated simulation model have been taken at a sampling rate of 1 Hz. Accordingly, the I-V curves utilized to validate the accuracy of the model have been traced at a sampling rate of 1 curve per second. Each curve includes 1000 voltage and current points, which were registered in a time period of 200 ms.

The accuracy of the simulated I-V and P-V curves is evaluated by means of RMSE and NRMSE values calculated between the measured and simulated P-V characteristics of the single PV module and the PV string. The $RMSE_P$ and $NRMSE_P$ are calculated according to Equations 5.4 and 5.5, respectively.

The accuracy of the simulated module temperatures is also evaluated by means of the RMSE analyzes. The $RMSE_T$ between the simulated and measured module temperature of the whole simulation time is defined as in Equation 5.1.

5.3.2 Experimental Verification with a Single PV Module

Two sets of measurements for PV module 19 were taken during seven hours on a clear sky and a partially cloudy day on August 27$^{\text{th}}$ and 23$^{\text{rd}}$, 2013, respectively. The objective of these measurement sets was to test and demonstrate the accuracy of the integrated dynamic simulation model for a single PV module with respect to measured electrical characteristics under homogeneous and highly fluctuating irradiance conditions.

The measured irradiance as well as the measured and simulated module temperatures during the seven hours for both days are shown in Figure 5.20. It can be seen from the irradiance measurements shown in Figure 5.20(a) how the sky was completely free of clouds during the morning hours. During the afternoon, however, the measurements indicate that a thin layer of clouds was covering the sky causing minor irradiance fluctuations. The simulated module temperature appears to be slightly higher in the morning and slightly smaller in the afternoon than the measured temperature. Nonetheless, the simulated module temperature presents a good agreement with the measured one for clear sky conditions with an $RMSE_{\text{T}}$ of 1.11 °C. For the partially cloudy day (Figure 5.20(b)), the irradiance measurement shows few periods of clear sky, but mostly large and fast irradiance fluctuations take place because of moving clouds. Under these conditions, the simulated temperature follows nicely the rapid changes in the measured temperature and only small errors are seen with respect to the measured one. The obtained $RMSE_{\text{T}}$ of 1.19 °C is well in line with the previous clear sky case. Errors of this order of magnitude in the simulated module temperature generate errors well below 1 % and 1 ‰ to the simulated voltages and currents, respectively. It seems that the dynamic thermal part of the simulation model works very well for the purposes of this study.

The MPP powers extracted from the measured and simulated I-V curves and the

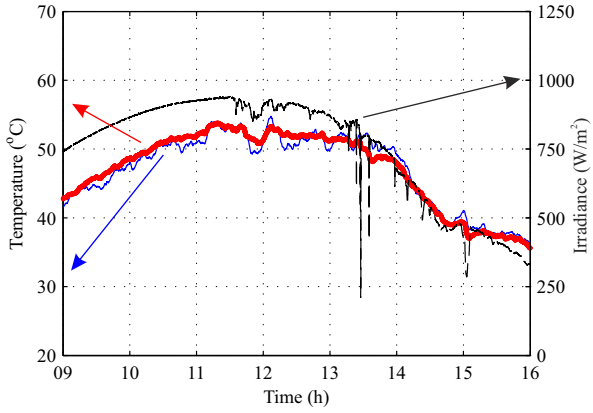

(a)

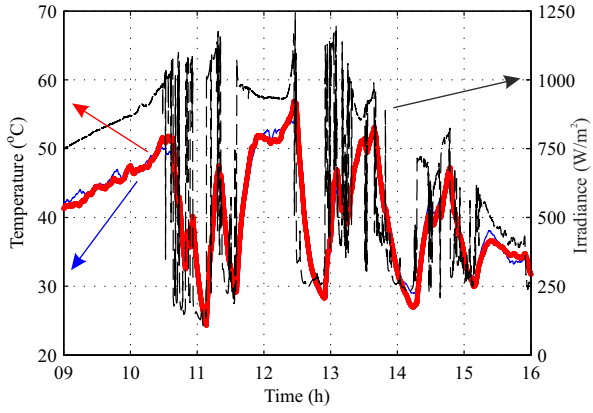

(b)

Figure 5.20: Measured irradiances (black dashed lines), measured module temperatures (blue lines) and simulated module temperatures (red dots) during seven hours on (a) a clear sky day on August 27$^{\text{th}}$, 2013 and (b) a partially cloudy day on August 23$^{\text{rd}}$, 2013. The arrows indicate the connections between the lines and the axes.

calculated $NRMSE_{\text{P}}$ values for both measurement days are shown in Figures 5.21 and 5.22. A good agreement exists between the MPP powers extracted from the simulations and measurements for both the clear sky and partially cloudy days shown in Figure 5.21, respectively. However, slightly bigger absolute errors are found during the periods of high irradiance than low irradiance. Furthermore, the predicted MPP powers are more accurate during steady periods than periods with fast and large irradiance fluctuations. This can also be seen in Figure 5.22 where the accuracy of the complete P-V curve is

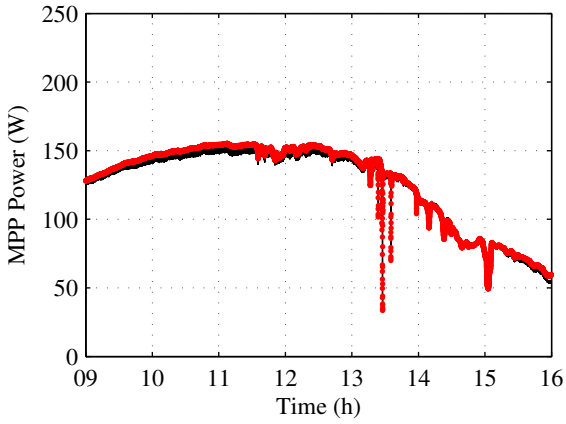

(a)

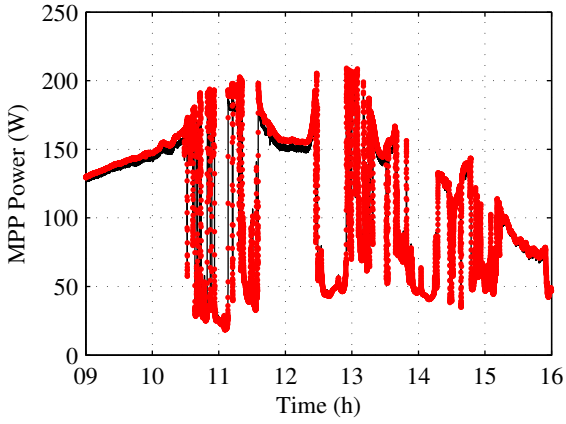

(b)

Figure 5.21: Measured (black lines) and simulated (red dots) MPP powers of PV Module 19 during seven hours (a) on a clear sky day on August 27$^{\text{th}}$, 2013 and (b) on a partially cloudy day on August 23$^{\text{rd}}$, 2013.

evaluated for both days. It can be observed that the simulation model predicts the P-V curve with average $NRMSE_{\text{P}}$ values of 1.76 % and 1.81 % during the clear sky and partially cloudy days, respectively. These results indicate that the electric part of the model is accurate throughout the whole range of irradiance conditions as a result of the improvements implemented in Section 4.3. The normalized error is, however, slightly larger for the partially cloudy day. This is an expected result because both thermal and electric models perform better when the PV module is not operating under fluctuating conditions. Figure 5.22(b) confirms this clearly by showing that the relative error is

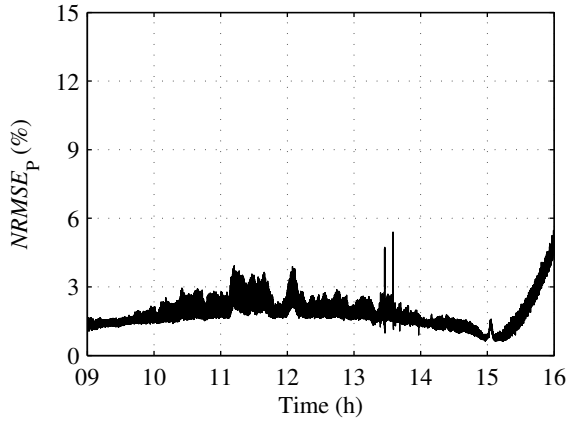

(a)

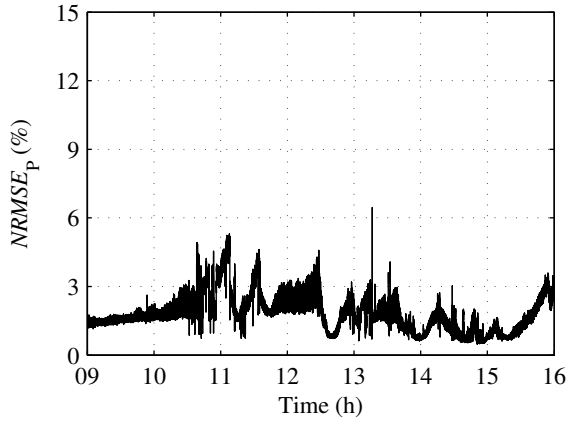

(b)

Figure 5.22: Calculated $NRMSE_P$ values between the measured and simulated P-V curves during the same time periods as in Figures 5.20 and 5.21.

largest when the operating conditions fluctuate fast. The absolute error, naturally, decreases with decreasing irradiance. The differences between the measured and calculated MPP powers may occur as a result of limitations in the integrated simulation model itself (both in electric and thermal models), as well as in the methods used to calculate model parameters such as the parasitic resistances. In addition, there are uncertainties inherent in the experimental data.

To prove that the simulation model operates as expected for longer periods of time, measurements of six to eight hours per day were taken during ten days between August 20$^{\text{th}}$ and October 16$^{\text{th}}$, 2013. As previously, the environmental measurements have been

utilized as input for the simulation model and the measured I-V curves serve as reference to calculate the errors in the predicted P-V curves by means of the $RMSE_{\mathrm{P}}$ and $NRMSE_{\mathrm{P}}$ parameters.

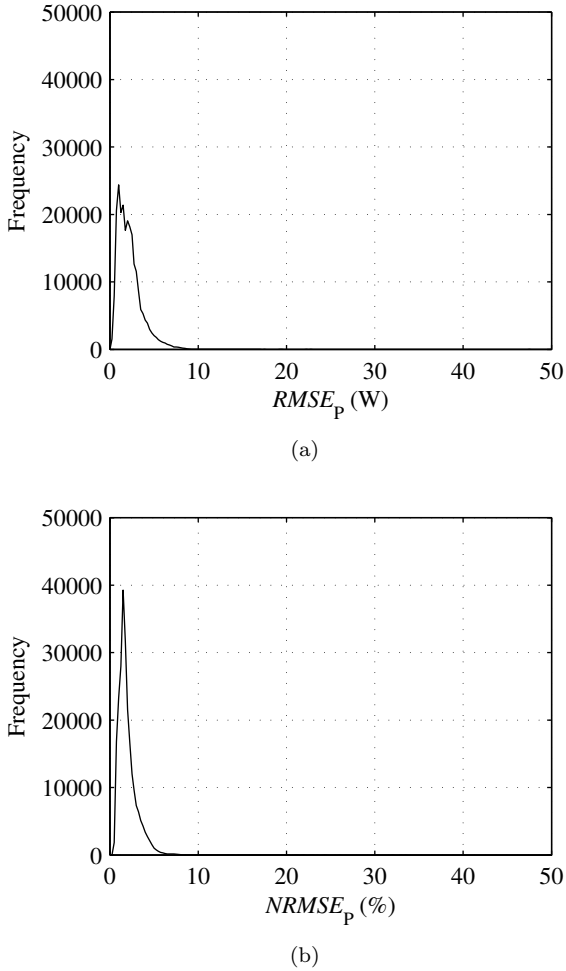

Figure 5.23: Distribution of calculated (a) $RMSE_{\mathrm{P}}$ and (b) $NRMSE_{\mathrm{P}}$ values between measured and simulated P-V curves of PV Module 19 during 10 days of measurements in August, September and October, 2013.

The histograms of the $RMSE_{\mathrm{P}}$ and $NRMSE_{\mathrm{P}}$ values obtained during the measurement period of 10 days for a single PV module are shown in Figure 5.23. As can be seen in Figure 5.23(a), around 99 % of the $RMSE_{\mathrm{P}}$ values are below 5 W, having the maximum frequency of around 1 W. It is about 0.6 % of the MPP power of 180 W under STC conditions for a single module. This is well in line with the histogram of $NRMSE_{\mathrm{P}}$

values illustrated in Figure 5.23(b) indicating that the maximum number of incidences in the normalized error of $NRMSE_{\mathrm{P}}$ is around 1.5 %, because the MPP power is smaller than 180 W during most of the studied periods and the average $NRMSE_{\mathrm{P}}$ value is 1.98 %. The simulation model provided slightly better results for the ten day period than for the single day measurements analyzed earlier. As a conclusion, we can state that the integrated simulation model provides a correct and accurate electrical behavior for a single PV module under varying real operating conditions.

5.3.3 Experimental Verification with a PV String

Along the same line as in the previous analysis with a single PV module, two sets of measurements were taken during six hours on a clear sky and a partially cloudy day on July 25$^{\mathrm{th}}$ and August 16$^{\mathrm{th}}$, 2013, respectively. The objective of these measurement sets was to test and demonstrate the accuracy of the integrated simulation model both in homogeneous irradiance conditions and in a day with high and fast irradiance fluctuations for a string composed of six series-connected PV modules. In this case, the irradiance reaching each PV module has been obtained by interpolating linearly between the measurements registered on the plane of the modules at both extremes of the string. The rest of the input parameters for each of the six modules are the global atmospheric conditions, i.e. the global and diffuse solar radiation on the horizontal plane, wind speed and direction and ambient temperature.

The measured irradiances as well as the measured and simulated temperatures of the PV module at one extreme of String 4 measured by sensors S6 during the measurement period of six hours are shown for both days in Figure 5.24. Measurements and simulations for the same time period conducted by sensors S5 gave almost identical results and, therefore, they are omitted here. Measured irradiance shown in Figure 5.24(a) indicates clear sky conditions for the whole measurement period apart from some minor irradiance fluctuations around 11:30 h. Simulated temperatures in both extremes of the PV string showed a good agreement with the measured temperatures as in the case of a single module. Average errors of the temperature predictions are small and the obtained $RMSE_{\mathrm{T}}$ values are 1.29 and 1.15 °C for sensors S5 and S6, respectively. Measurement and simulation results of sensors S6 on a half cloudy day of August 16$^{\mathrm{th}}$, 2013, are shown in Figure 5.24(b). The irradiance measurement shows clear sky conditions before 12:00 h, then in the afternoon three cloudy overcast periods covering the PV string fully and plenty of moving clouds that generate rapid and large irradiance fluctuations. The simulated temperatures for the modules located at both extremes of the string present accuracies in line with the previous results with $RMSE_{\mathrm{T}}$ of 1.83 °C and 1.46 °C for sensors S5 and S6, respectively.

The MPP powers extracted from the measured and simulated I-V curves and the

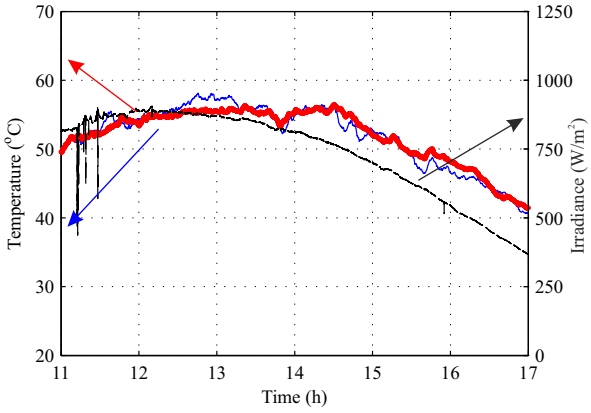

(a)

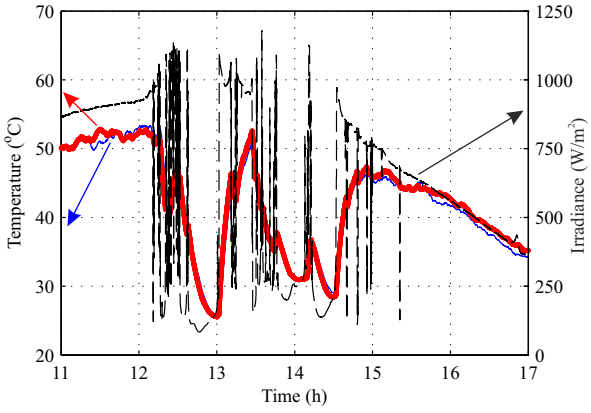

(b)

Figure 5.24: Measured irradiances (black dashed-lines), measured module temperatures (blue lines) and simulated module temperatures (red dots) during six hours (a) on a clear sky day on July 25$^{\text{th}}$, 2013 and (b) on a partially cloudy day on August 16$^{\text{th}}$, 2013 measured by sensors S6 located at one extreme of String 4. The arrows indicate the connections between the lines and the axes.

calculated $NRMSE_{\text{P}}$ for both days are shown in Figures 5.25 and 5.26. Along the same line as for the single PV module, the absolute error of the predicted MPP power is larger at high irradiances than during the rest of the measurement period (Figure 5.25). However, this error seems to be slightly larger for a string of PV modules than for a single PV module. The reason for this is that now six modules are being simulated and the error in each of them adds up and arises due to mismatch losses, etc. Also the irradiances affecting four of the PV modules in the middle of the string have been approximated by

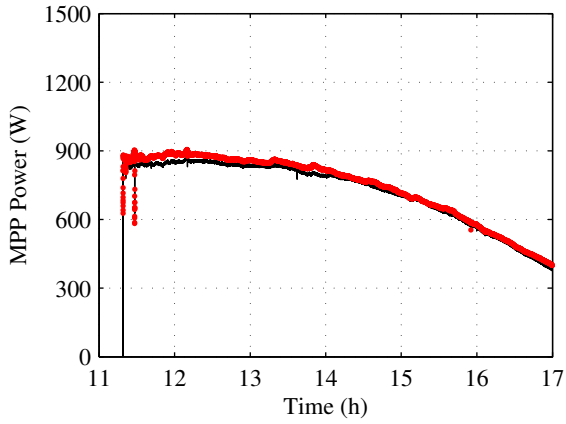

(a)

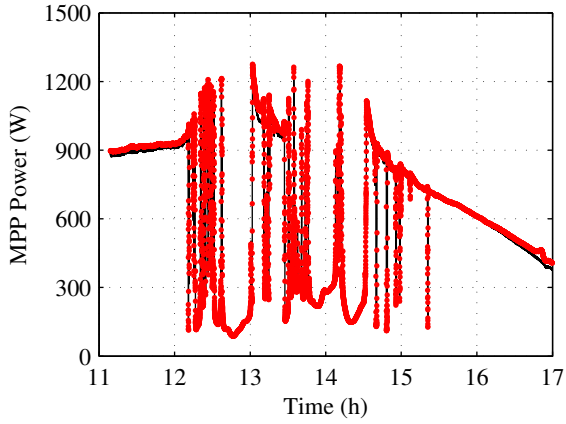

(b)

Figure 5.25: Measured (black lines) and simulated (red dots) MPP powers of String 4 during six hours (a) on a clear sky day on July 25$^{\text{th}}$, 2013 and (b) on a partially cloudy day on August 16$^{\text{th}}$, 2013.

interpolation, which may cause some errors. Nevertheless, the curves of the simulated MPP powers follow the measured MPP powers with fairly good precision.

The obtained $NRMSE_{\text{P}}$ values for the clear sky and partially cloudy day are illustrated in Figure 5.26. It can be noticed that the obtained $NRMSE_{\text{P}}$ values are marginally larger for the PV string than for the single PV module (Figure 5.22) during the periods of high irradiance. However, the largest values of $NRMSE_{\text{P}}$ are found during cloudy overcast periods and periods of moving clouds with high irradiance fluctuations, as expected. The average $NRMSE_{\text{P}}$ values for String 4 during the clear sky and par-

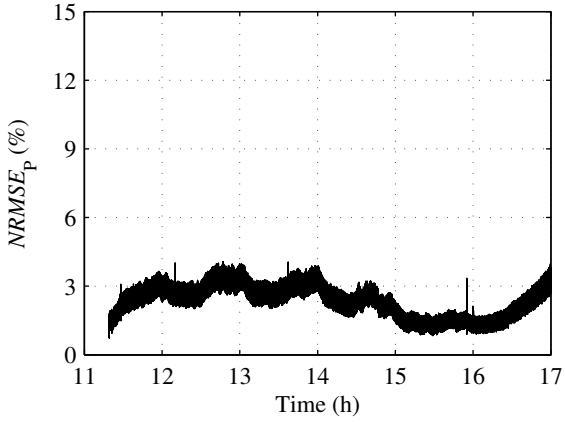

(a)

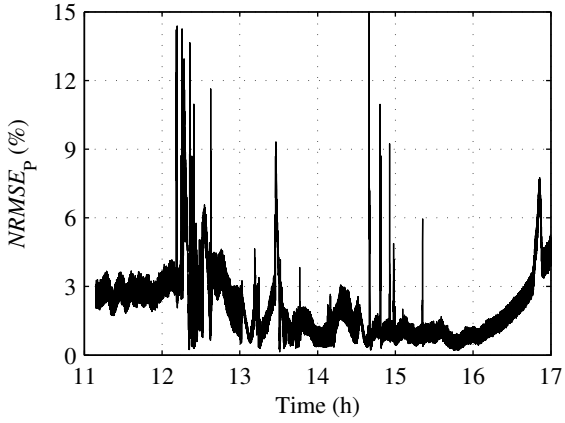

(b)

Figure 5.26: Calculated $NRMSE_P$ values between the measured and simulated P-V curves during the same time periods as in Figures 5.24 and 5.25.

tially cloudy days were 1.86 % and 2.02 %, respectively. These results are well in line with the ones obtained in the previous section for the single PV module.

To confirm the operation of the integrated simulation model for the PV string, also in this case, measurements of six to eight hours per day were taken during 10 days between July 12th and August 20th, 2013. The environmental measurements have been used as input for the simulation model while the traced I-V curves have been utilized to calculate the error in the predicted P-V curves by means of the $RMSE_P$ and $NRMSE_P$ values for each measurement time step. As explained before, the irradiances of the PV modules located in the middle of the string have been obtained by interpolation from irradiances

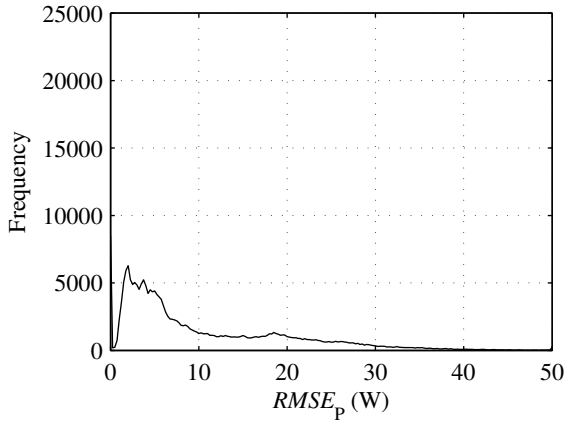

(a)

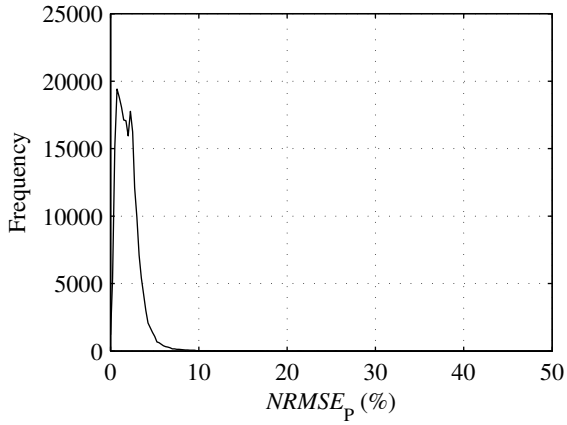

(b)

Figure 5.27: Distribution of calculated (a) $RMSE_{\mathrm{P}}$ and (b) $NRMSE_{\mathrm{P}}$ values between measured and simulated P-V characteristics of String 4 during 10 days of measurements in July and August, 2013.

measured by sensors S5 and S6.

The histograms of the $RMSE_{\mathrm{P}}$ and $NRMSE_{\mathrm{P}}$ values of the simulated P-V characteristics obtained during the measurement period of 10 days are shown in Figure 5.27 for the PV string of six series-connected modules. Most of the calculated $RMSE_{\mathrm{P}}$ values are below 30 W according to Figure 5.27(a), which was expected since most of the values were below 5 W for a single PV module. It can be concluded that the error seems to add up and is proportional to the number of modules connected in the string. The highest number of $RMSE_{\mathrm{P}}$ values during the test period was around 2 W for the PV

string. The histogram of the $NRMSE_{\mathrm{P}}$ values in Figure 5.27(b) presents a similar trend as earlier for a single PV module in Figure 5.23(b). This is also an expected result due to the normalization of the error. In this case, the histogram shows a bit wider range of values than for a single module, even though most of the errors are below 5 % and almost all are below 7 %. The maximum frequency of $NRMSE_{\mathrm{P}}$ values is at 0.75 % and the average value is 1.98 %. These results demonstrate that the dynamic thermal and electrical simulation model can be used to predict P-V characteristics also for PV strings with the same accuracy as for individual PV modules.

5.4 Conclusions

The Fifth Chapter discussed the experimental implementation and verification of the simulation models presented in the Fourth Chapter as well as the inclusive thermal and electric simulation model.

Firstly, the dynamic thermal model has been adapted and further developed from the previous work of other authors. For example a relatively straightforward and simple way has been developed to estimate the temperature of the sky by using diffuse fraction of solar radiation to discern between clear sky and overcast conditions. Another novelty of this work is the use of 1-second climatic and environmental measurements of the TUT PV power station research plant. In addition, a simple practical approach is provided to further improve the accuracy of the model with respect to site-specific environmental factors in the form of sensitivity analysis. Three day measurement periods on winter, spring and summer time were used to develop and verify the dynamic thermal model. The simulated daytime PV module temperature accuracies with respect to measured module temperatures were 1.53, 1.28 and 1.27 °C, respectively. Finally, the accuracy of the simulation model was tested with the measured data for 91 consecutive days during summer, 2012. The dynamic thermal model predicted the daytime module temperatures with an average accuracy of 1.63 °C and the difference between simulated and measured temperatures was less than 2 °C for 80 % of the time. The introduced dynamic thermal model is first of the kind without major compromises and, therefore, provides accurate estimates for PV module temperatures on a 1-second time scale.

Secondly, the electric model has been implemented and its operation assessed by the $RMSE$ and $NRMSE$ between the measured and simulated P-V curves. Subsequently, the simulation model has been further developed improving its accuracy during operation at low irradiance conditions. A sensitivity analysis was undertaken identifying the relative relevance of the parameters on the accuracy of prediction of the I-V characteristics. After adjusting the behavior of the shunt resistance as inversely proportional to the irradiance received by the PV module, the analysis of the $RMSE_{\mathrm{P}}$ and $NRMSE_{\mathrm{P}}$ showed a remarkable improvement in the accuracy under operation at low and medium irradiance

conditions. Finally, the electric simulation model has been tested under static operating conditions for a single PV module and a PV string of six series-connected modules. The PV module was measured under natural balanced irradiance conditions on a clear sky and an overcast day and the measured and simulated P-V curves demonstrate the accuracy of the utilized model under different operation conditions for the whole voltage range. For the PV string, four partial shading conditions caused by a built structure and one homogenous irradiance conditions were exploited. Despite the assumptions made during the simulations, a good agreement exists between simulated and measured electrical characteristics and the results endorse the correct operation of the electric model in case of series-connected PV modules since the model.

Lastly, the operation of the integrated dynamic simulation model has been tested and validated with climatic and I-V curve measurements conducted in the TUT solar PV power station research plant. Sampling frequency of 1 Hz was used for measured climatic and electric quantities (I-V curve was traced within 200 ms once a second). Measurements of six to eight hours per day have been done during ten days both for a single PV module and for a string of six series-connected PV modules to verify the operation of the simulation model under varying environmental conditions. The accuracy of the thermal simulation model has been analyzed by means of the root mean square error analyses between the simulated and measured PV module temperatures. Accordingly, the accuracy of the integrated dynamic thermal and electric simulation model has been analyzed by means of the normalized root mean square error analyses between the simulated and measured P-V characteristics both for the single PV module and the string of PV modules. The results show a good agreement between the predicted and measured module temperatures, as well as the P-V curves and maximum power points both for the PV module and the string of PV modules during clear sky and partially cloudy days. The predicted module temperatures gained an average $RMSE_{\mathrm{T}}$ of 1.34 °C. Accordingly, the average $NRMSE_{\mathrm{P}}$ of the simulated P-V curves was 1.98 % for both the single PV module and the string of PV modules. As a conclusion, it can be stated that the developed model is the state of the art dynamic thermal and electric simulation model for PV systems.

6 EFFECT OF PARTIAL SHADING CAUSED BY CLOUDS ON PV GENERATORS

One barrier against high PV penetration is the variability of the output power (Bosch et al., 2013). Previous authors' work proved that hourly solar radiation measurements are insufficient to properly analyze the operation of PV power generators and, therefore, cannot be used to improve the design of the power electronic components and devices interfacing generators to the grid. As the utilized sampling frequency increases, fluctuations and variability in solar radiation measurements increase. In addition, high sampling frequency allows analyzing the gradients of irradiance profiles, which are important for optimizing the inverter performance and maximum power point tracking techniques. There is a demand for improvement because today's PV inverters are non-ideal and do not continuously reach their best performance.

Clouds cause spatial and temporal variability of solar radiation which is the main cause of fluctuating photovoltaic power feed into the grid (Bosch et al., 2013). The changes in power production due to clouds have been noticed to be large and fast (Mäki and Valkealahti, 2012a). Studies indicate that long strings of series connected PV modules are affected more severely by partial shading caused by moving clouds than parallel connections of PV modules. Different configurations of PV power generators require different characteristics from the power electronics interfacing them to the grid (i.e. centralized technology, string and multi-string technology or AC-module technology). Precise information of the instantaneous irradiance conditions affecting the generator is needed to pursue systematic and comprehensive studies to understand the effects of clouds on the operation of PV generators from the electrical grid perspective.

The sixth Chapter discusses the effect of partial shading caused by clouds on various configurations of PV generators. First, a method to generate a spatial irradiance map derived from an array of solar radiation measurements is proposed. Subsequently, the dynamic nature of partial shading caused by moving clouds is studied, as well as the mismatch losses caused by them in the operation of different PV generator configurations. For this purpose, measurements from TUT solar PV power station research plant are utilized to create a spatial irradiance map by the second during the summer months in 2012. Besides of the incoming irradiance affecting the modules, the measured

module temperatures have been taken into account and used as input in the simulation model implemented in Matlab. The content of this Chapter has been presented earlier in (Torres Lobera and Valkealahti, 2013b).

6.1 Spatial Irradiance Distribution Map

Hourly solar radiation measurement values have traditionally been used to estimate the power generated by a PV generator. However, to analyze the effects of non-homogenous irradiance conditions and of the dynamic behavior of solar radiation on the performance of PV generators during periods of shading caused by moving clouds requires an increased sampling rate of the irradiance measurements from hourly values to seconds or tenths of seconds (Burger and Rüther, 2006). These resolutions permit, additionally, studying the irradiance gradients which can be used to discern between periods of homogeneous irradiance conditions and periods of shading caused by moving clouds or buildings. Furthermore, there is a need of a dense grid of irradiance values, i.e. a spatial irradiance map, to evaluate the effects of non-homogenous irradiance conditions on the operation of different PV generator configurations.

In previous studies, different approaches have been presented and discussed to generate spatial irradiance maps based on interpolation methods, e.g. linear, nearest neighbor or bi-harmonic interpolation (Feliciano-Cruz and Ortiz-Rivera, 2012). A different approach was presented in (Weigl et al., 2012) where the cloud velocity vector was calculated from irradiance measurements of a set of sensors and used to predict the irradiance levels received in every part of the map. Similarly, in (Torres Lobera and Valkealahti, 2013c), a method was developed to generate a spatial irradiance map from an array of solar radiation measurements during shading events caused by moving clouds by analyzing their speed and direction of movement. For the present study, the natural neighbor interpolation method was the most suitable and simple approach for generating the spatial irradiance map with sufficient accuracy, because the mesh of irradiance sensors is dense with short distances between sensors. The basic two dimensional equation of the natural neighbor interpolation is

$$G\left(x,y\right)=\sum_{\mathrm{i}=1}^{\mathrm{n}} w_{\mathrm{i}} f\left(x_{\mathrm{i}},y_{\mathrm{i}}\right), \tag{6.1}$$

where $G\left(x,y\right)$ is the estimated irradiance at point (x,y) and n the number of measurement points. w_{i} and $f\left(x_{\mathrm{i}},y_{\mathrm{i}}\right)$ are the weight and the known irradiance at the measurement point $(x_{\mathrm{i}},y_{\mathrm{i}})$, respectively. The weights are calculated based on the Voronoi diagram which is a technique to divide the space into a number or regions corresponding to a set of known points (Aurenhammer, 1991).

For the current study, the spatial irradiance map has been developed based on the measurements of 17 photodiode-based SpLite2 irradiance sensors marked from S1 to S17 in Figure 3.2. The generated spatial irradiance distribution map for an instant during a shading event caused by a cloud is illustrated in Figure 6.1. In it, the edge of the cloud can be observed to cause a transition from high to low irradiance values.

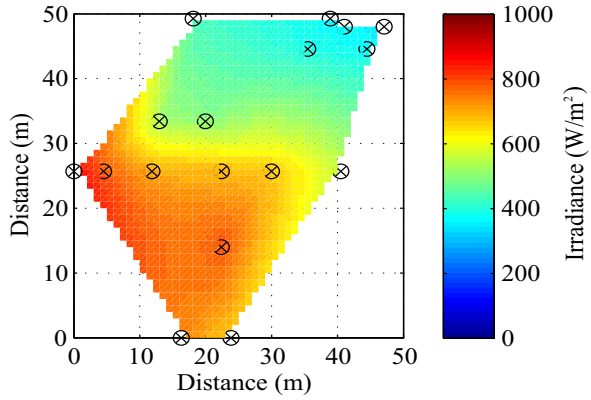

Figure 6.1: Spatial irradiance distribution map generated by interpolating the solar radiation measurements around the TUT solar PV power station research plant during a shading event caused by a cloud. The location of the irradiance sensors utilized for generating the spatial irradiance map are marked with circled crosses.

6.2 Studied Systems

PV power generators consist of interconnected modules to achieve certain power requirements in terms of voltage and current. In the present work, two types of electrical interconnections of PV generators are studied: series-connected string of PV modules and parallel-connected PV modules. Series-connected PV modules lead to generators which generate a common current flowing through all the modules, while the total voltage of the generator results from adding up the separate voltages produced by each module. Parallel-connected PV modules, on the contrary, constitute generators in which the output voltage is common to all the modules and the current of the generator results from adding up the currents of separate modules.

Four different PV power generators composed of 24 modules with different physical layouts have been studied in this Chapter. The size of the generators has been limited due to the high computing power required to analyze the extensive climatic data. The studied generator layouts: the short-vertical (SV), short-horizontal (SH), long-vertical (LV) and long-horizontal (LH) layout are illustrated in Figure 6.2 . The horizontal direction is along the west-east direction of the TUT solar PV power station research plant and

the vertical direction along the south-north direction. Self-shading related issues have been avoided by considering large enough distance of 3 m between equivalent points of consecutive rows of PV modules. The dimensions of the modules are 1.5 m times 1.0 m and the tilt angle is 45°.

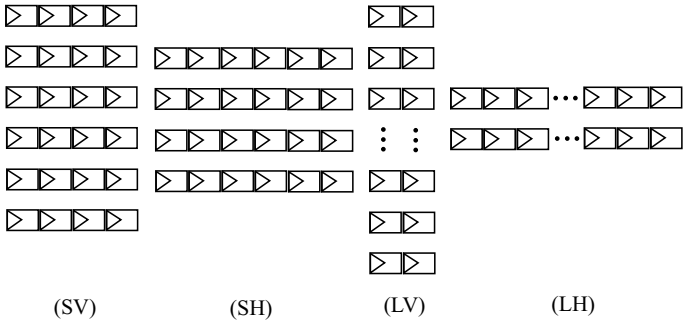

Figure 6.2: Physical layouts of the studied PV power generators.

The technical characteristics of the PV modules have been extracted from the modules installed in TUT solar PV power station research plant, i.e. NAPS NP190GKg modules, shown in Table 3.1.

The irradiances and module temperatures utilized in this study were measured during 92 days during the months of June, July and August, 2012 with a sampling frequency of 10 Hz by the measuring systems of the TUT solar PV power research plant. Subsequently, the data was down-sampled to one measurement per second per sensor which still permits to analyze even the fastest irradiance changes affecting the PV modules. The studied period of time has been chosen so that no partial shading of the facility is caused by building structures. Moreover, the data has been selected daily only from 9 to 19 h to ensure that the irradiance changes during sunrise and sunset do not affect the analyses.

6.3 Extraction of Mismatch Losses

Mismatch losses are defined as the power losses in a PV power generator caused by the mismatch operating conditions affecting its interconnected modules. In other words, a PV generator operating at its own maximum power point forces its modules to operate at points different from their individual MPPs during non-homogenous operating conditions. The power that is lost in this way is known as mismatch losses and can be calculated as:

$$ML = \sum_{\mathrm{i}=1}^{\mathrm{N}} P_{\mathrm{MPP,i}} - P_{\mathrm{MPP,Gen}}, \tag{6.2}$$

where N is the number of modules forming the PV generator, $P_{\mathrm{MPP,i}}$ is the MPP power of an individual module i and $P_{\mathrm{MPP,Gen}}$ is the MPP power of the generator.

Evaluation of the ML requires precise knowledge of the instantaneous operating conditions of each module forming the PV generator. The spatial irradiance distribution map method presented in Section 6.1 has been used for obtaining the operating irradiance conditions of each module of the generator. Additionally, the same natural neighbor interpolation method was utilized to obtain the operating module temperatures.

Moving clouds progressively cover the area where the PV modules are located during transition periods from clear sky to shading conditions. This can be seen in Figure 6.3 where the irradiances measured by sensors S1, S13 and S16 (see Figure 3.2) are shown, as an example, within a 10 minute period during a shading event on 27$^{\mathrm{th}}$ of July, 2012. These three sensors have been chosen to detect non-homogenous conditions due to moving clouds since they are far from each other. The irradiance drop from 1000 to 250 W/m^2 in Figure 6.3 measured by the three sensors is obviously caused by the same cloud because the irradiance drops are concurrent, only delayed in time between sensors. However, the irradiance curves are not fully identical and the delays in time are not quite systematic, presumably due to an irregular cloud edge.

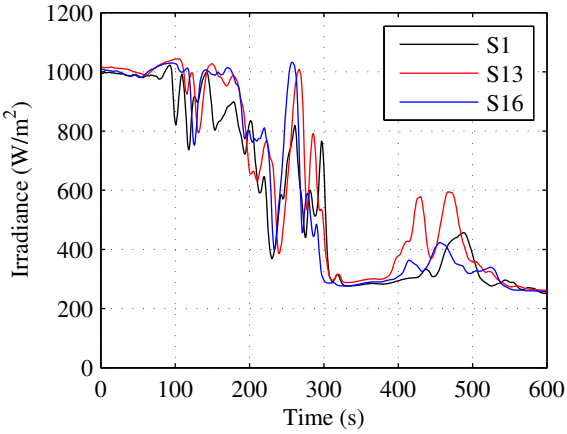

Figure 6.3: Measured irradiances by sensors S1, S13 and S16 during a shading event caused by a cloud on 27$^{\mathrm{th}}$ of July, 2012.

The calculated instantaneous mismatch power losses are illustrated in Figure 6.4 for the series-connected SH and LH generators during the 10 minute period shown in Figure 6.3. It can be easily noticed that the mismatch power losses are considerably larger for the LH generator compared to the SH generator. Reason for this is that all modules in the SH generator are located closer to each other than in the LH generator. Therefore, irradiance differences between PV modules are smaller in the SH generator than in the

LH generator leading to smaller mismatch power losses. During periods of homogenous operating conditions before 100 s, between 300 and 400 s, and after 550 s, the mismatch power losses are small as expected for homogeneous irradiance conditions.

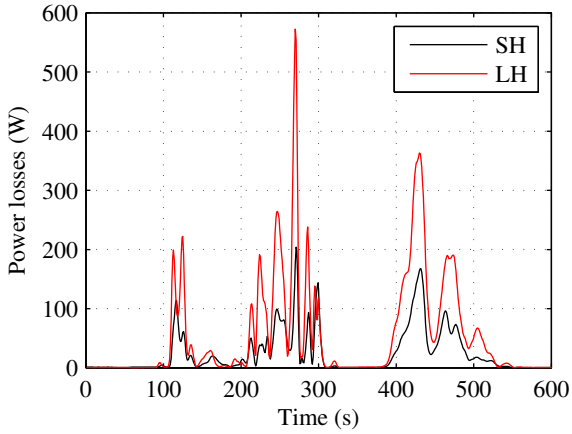

Figure 6.4: Mismatch power losses of the series-connected generators SH and LH during the shading event illustrated in Figure 6.3.

A straightforward crude force method to calculate the mismatch power losses over a period of interest would be to simply calculate the irradiance maps for the whole period and then the ML, accordingly. However, that would require enormous computer resources to analyze a relevant time period of the order of months. Therefore, a method is needed to recognize changing irradiance conditions causing ML to avoid useless calculations. A possible solution to detect the changing irradiance conditions, e.g. caused by a moving cloud, is to use the derivative of the irradiance as an indicator of changing environmental conditions. Changes in irradiance are continuous due to the dynamic nature of solar radiation and the rotation of the Earth around its axis. However, changes during the transition periods of shading caused by clouds are much larger and steeper.

The absolute values of the calculated irradiance gradient with respect to time are shown in Figure 6.5 for the measurement period illustrated in Figure 6.3. The derivative of irradiance appears to change constantly, partially due to noise in the measurements. However, it is possible to define a limit value for the rate of irradiance change which permits to discern between homogenous and non-homogenous irradiance conditions caused by clouds. One can become convinced of that just by comparing Figures 6.3 and 6.5. A limit of 5 W/m^{2}s was selected for the summer months, at which time the levels of irradiance are the highest during the year. The limit is marked in Figure 6.5 with a horizontal black line.

For the analyses of the next sections, the data was first processed according to the

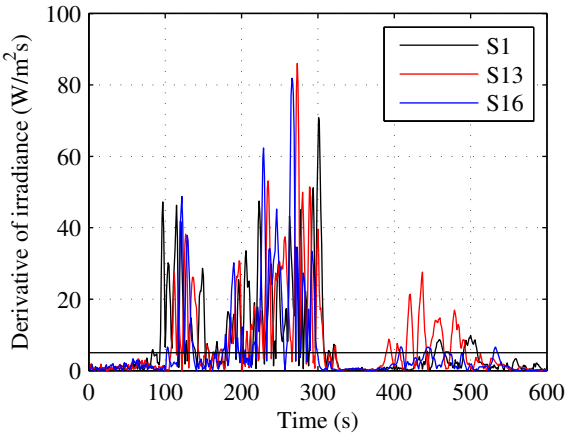

Figure 6.5: Absolute values of the time derivative of irradiances measured by sensors S1, S13 and S16 during the shading event shown in Figure 6.3. The limit value of 5 W/m^{2}s for changing irradiance conditions is indicated with a horizontal black solid line.

procedure described above, i.e., by selecting only the periods of time when irradiance measured by sensors S1, S13 and S16 changed faster than 5 W/m^{2}s. This way new sets of data were constituted involving only periods of non-uniform irradiance conditions due to clouds affecting the PV modules. These sets of data were then utilized to analyze the effects of moving clouds on the mismatch losses for different PV power generator configurations.

6.4 Characteristics of Partial Shading Caused by Clouds

It is obvious that the effects of changing irradiance conditions due to moving clouds on the operation of PV generators depend on generator size. Important factors are the magnitude and frequency of irradiance differences within the generator area. To illustrate these effects, the cumulative instantaneous maximum irradiance difference distributions are shown in Figure 6.6 for several square plant areas of generators during 92 days in June, July and August, 2012. The analyzed areas are comprised within the vicinity of the solar radiation measurement mesh illustrated in Figure 3.2. They are selected to be from 25 to 2500 m^2 corresponding to generators from 8 to 528 modules, when using the same module installation and placing as in Figure 6.2. The dimensions of the sides of the area increase from 5 to 50 m, correspondingly. The studied SH generator occupies quite closely a square of 100 m^2.

The dynamic nature of the effect of moving clouds on the irradiance on a generator plant area is visible in Figure 6.6. For small areas, i.e. small maximum distances between modules, the maximum irradiance differences are considerably smaller than for large

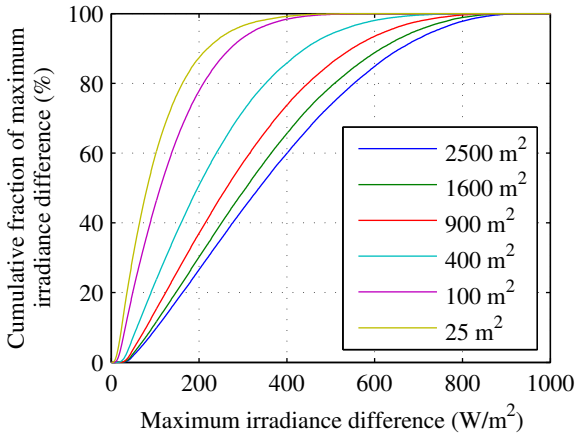

Figure 6.6: Cumulative distributions of the instantaneous maximum irradiance difference for different power plant areas measured by the grid of irradiance sensors illustrated in Figure 3.2 during non-homogenous irradiance conditions in June, July and August, 2012.

areas. 90 % of the maximum irradiance differences are smaller than 220 and 659 W/m^2 for areas of 25 and 2500 m^2, respectively. It is evident that the amount of high maximum irradiance differences received between PV modules increases with increasing area of the generators. Majority of the irradiance differences for 25 and 100 m^2 areas are below 200 W/m^2 demonstrating that the width of the shadow transition strip due to the edge of a cloud is typically larger than the dimension of the area. For larger surface areas from 900 to 2500 m^2 the cumulative maximum irradiance difference distribution starts to saturate and the 90 % limit is around 600 W/m^2. This high irradiance differences take place typically between clear sky and fully shaded conditions. A conclusion from this is that the width of the shadow transition strip caused by the edge of a cloud is typically below 30 m.

The power losses of PV generators operating under partial shading conditions are highly affected by the level of attenuation of solar radiation caused by the shading object, e.g. clouds (Mäki and Valkealahti, 2012b). This level of attenuation can be defined as the shading strength as:

$$SS = \frac{|\Delta G|}{G_{\max}}, \tag{6.3}$$

where ΔG is the irradiance difference between two measurements and $G_{\max}$ is the maximum of the two irradiance measurements.

The cumulative distributions of the maximum shading strengths observed for several PV generator plant areas are shown in Figure 6.7 during the measurement period. The

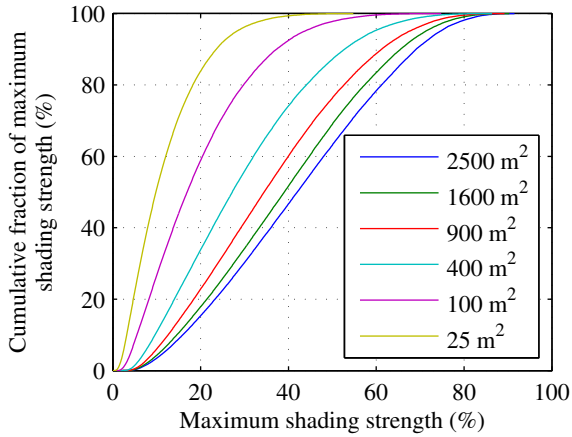

Figure 6.7: Cumulative distributions of the instantaneous maximum shading strengths for several generator plant areas measured by the grid of irradiance sensors illustrated in Figure 3.2 during non-homogenous irradiance conditions in June, July and August, 2012.

maximum shading strenghts have been calculated considering the maximum irradiance differences within the generator area. It is evident that irradiance difference and shading strength are closely related quantities as can be seen by comparing Figures 6.6 and 6.7. Along the same line as for the maximum irradiance differences, the relative amount of high maximum shading strengths increases with increasing area of the generator. 90 % of the maximum shading strengths are smaller than 23.6 % and 69.1 % for generator plant areas of 25 and 2500 m^2, respectively. The cumulative maximum shading strength distribution for 100 m^2 differ more from the 25 m^2 distribution than in the case of irradiance difference distributions. The reason for this is that both areas are typically within the transition area of shading, but shading strength is a relative quantity with respect to the highest irradiance within the generator plant area at each moment. As was in the case of maximum irradiance differences, the cumulative distributions of maximum shading strengths do not move towards higher shading strengths with increasing generator plant area at large areas any more. The simple explanation for this is that the transition region from clear sky to fully shaded conditions is smaller than the dimension of the generator area.

6.5 Missmatch Losses Caused by Clouds

The operation of an interconnected group of PV modules, i.e. a PV generator, is affected by the non-uniform irradiance operating conditions causing mismatch losses. Partial shading caused by moving clouds generates such non-uniform conditions as is shown in Figures 6.6 and 6.7 and leads to mismatch losses.

The physical PV generator layouts shown in Figure 6.2 having both series- and parallel electrical connection of PV modules have been studied during non-homogenous irradiance conditions in June, July and August, 2012. The total ML for the four different generators have been presented in Table 6.1. The results indicate that parallel connection of PV modules in generators produces consistently smaller mismatch losses than series connection.

Table 6.1: Mismatch losses due to partial shading conditions in June, July and August, 2012 for four generator configurations.

Gen.	Mismatch Losses			
	Series connection		Parallel connection	
	(Wh)	(%)	(Wh)	(%)
SH	1428	1.068	26	0.020
SV	1391	1.043	30	0.023
LH	1928	1.461	27	0.021
LV	2051	1.538	52	0.039

The four generators evaluated in this Section have the same amount of PV modules and are located through areas of the same size, but with different layout distributions. The ML caused by moving clouds are actually dependent on the speed, direction and shape of the clouds. It is evident based on Table 6.1 that series connection of PV modules is much more prone to ML due to partial shading caused by clouds than parallel connection. It is also clear that the long string-like layout of PV modules present higher ML than the square shaped layout both for series and parallel connection. LH layout had the smallest ML values and is closest to the shape of a square and LV layout had the largest ML values and has the shape farthest from a square.

6.6 Conclusions

A method to generate a spatial irradiance map from a set of 17 irradiance measurements by using the natural neighbor interpolation method is proposed in this Chapter. Additionally, a technique to discern non-homogenous irradiance conditions caused by moving clouds has been presented. It is based on analyzing the derivate of irradiance with respect to time. These tools have been used to analyze the effect of moving clouds on the irradiance conditions and mismatch losses on several PV generator configurations and layouts.

The dynamic nature of the partial shading caused by moving clouds has been studied by analyzing the cumulative distributions of maximum irradiance differences and maximum shading strengths for different power plant areas during a three month measurement period. The results show that both maximum irradiance differences and maximum shad-

ing strengths increase with increasing area of the PV generator. Furthermore, the effect of PV generator layout on mismatch losses was studied. PV generators having PV modules located with square shape have lower mismatch losses than if modules were located as long straight strings. This is due to the increasing irradiance differences with increasing dimension of the PV generator.

Based on the findings of this work, power losses caused by mismatch operating conditions due to moving clouds can be reduced by locating PV modules of the generator as close to each other as possible.

7 CONCLUSIONS

This Chapter contains the final concluding discussion of the thesis. The most important findings are summarized jointly with the scientific contribution of the work. In addition, a brief discussion on possible future topics related to the research will be presented.

7.1 Final Conclusions

This thesis provided a comprehensive study on the modeling of the thermal and electric operation of PV power generators under varying atmospheric conditions. Their operation has been modeled theoretically and, subsequently, verified with experimental measurements utilizing a systematic approach. Additionally, the effects of partial shading caused by moving clouds on the operation of PV generators have been studied.

The atmospheric and electric measurement systems required to analyze the operation of PV systems under non-uniform and rapidly varying weather conditions have been designed and implemented. These measurement systems include an I-V curve tracer based on IGBT technology that permits measuring and recording the I-V characteristics of PV modules and PV strings continuously. A sampling frequency of 10 Hz has been found to be sufficient to detect even the fastest phenomena related to power generation with PV power plants.

A dynamic thermal model of a PV module which considers its thermal mass and all relevant heat transfer mechanisms involved has been implemented based on previous authors' work. The accuracy of this thermal model has been improved by including necessary site-specific parameters. Additionally, a sensitivity analysis of the key parameters has been conducted to analyze their effect on the predicted module temperatures and to obtain the best set of parameter values. The performance of the thermal model has been evaluated continuously during several months by comparing the predicted and measured module temperatures at a 1-second time scale. The average $RMSE_{\mathrm{T}}$ was 1.63 °C and the difference between simulated and measured temperatures was less than 2 °C for 80 % of the time.

An electric model of a PV module which considers the parasitic effects and bypass diodes has been implemented. The relevance of the five parameters governing the model on the accuracy of the predicted power has been identified carrying out a sensitivity analysis of the parameters. The electric model has been further developed to improve its

performance under low and medium irradiance conditions. Furthermore, a method has been developed to assess the electric model performance by calculating the $RMSE_{\mathrm{P}}$ and $NRMSE_{\mathrm{P}}$ of measured and simulated P-V curves continuously by the second. This is noteworthy compared to earlier approaches where typically some characteristic points of separately measured P-V curves were utilized.

A state of the art comprehensive dynamic thermal and electric simulation model has been implemented by combining the separate previously presented thermal and electric models. This inclusive simulation model has been tested for a single PV module and a PV string of six series-connected PV modules. The validation has been carried out by studying the deviation of the predicted module temperatures and P-V characteristics with respect to measured module temperatures and P-V characteristics for a set of measurements of six to eight hours per day during twenty days at a 1-second time scale. The predicted module temperatures gained an average $RMSE_{\mathrm{T}}$ of 1.34 °C. Accordingly, the average $NRMSE_{\mathrm{P}}$ of the simulated P-V curves was 1.98 % for both the single PV module and the string of PV modules. As a conclusion, it can be stated that the developed model is the state of the art inclusive dynamic thermal and electric simulation model for PV systems.

Additionally, a method has been proposed to generate a spatial irradiance distribution map from a set of irradiance measurements by using the natural neighbor interpolation method. Thereafter, the irradiance distribution map has been utilized to analyze the effect of moving clouds on the irradiance conditions and mismatch power losses on several PV generator configurations and layouts. The effect of PV generator layout on mismatch losses was studied for series- and parallel-connected PV modules. PV generators having PV modules located in a square shape have lower mismatch losses than if modules were located as long straight strings. Moreover, the mismatch power losses in series-connected PV generators were over forty times higher than in parallel-connected generators. Mismatch losses alone can be up to 1.5 % of the total energy production in case of poor generator layout design.

7.2 Future Research Topics

This thesis provided a comprehensive study on analyzing and modeling the operation of PV generators under varying atmospheric conditions and verified the accuracy of a proposed inclusive thermal and electrical simulation model with experimental measurements. Additionally, the effects of partial shading caused by moving clouds on different PV generator configurations were studied as well. However, the outcome of this thesis raises the following interesting topics for future research:

- This thesis proposed the one-diode model presented by Villalva et al. (2009b) to model the electrical operation of PV modules and detailed a method to obtain the

five unknown parameters governing the model. This approach served well to the purposes of the research as it provided good accuracy for the PV modules installed in TUT solar PV power research plant. However, there are several alternatives in the literature to obtain the five parameters of the model (De Soto et al., 2006; Laudani et al., 2013; Lo Brano et al., 2010; Mermoud and Lejeune, 2010). For further work, it would be interesting to perform a comparison study of the efficiency and performance of these approaches.

- In this thesis, the accuracy and correct operation of the proposed inclusive simulation model has been assessed and verified. In the future, the proposed model could be utilized to asses and verify the operation of commercial inverters interfacing PV strings to the grid. In (Torres Lobera and Valkealahti, 2014c), the authors have undertaken a pre-study along this line that indicates that the model is suitable for the task. However, a more systematic and comprehensive approach should be considered.

- It would be very interesting to study if the proposed inclusive simulation model can be implemented to assist in developing different MPPT algorithms. One approach could be to utilize the simulation model to provide a range of voltages around the MPP voltage helping the algorithms to converge faster. Another alternative could be to utilize the simulation model to ensure that the MPPT algorithm indeed reached the global MPP and not some other local MPP.

- In line with the previous point, it would be most interesting to study the suitability of the simulation model to be utilized as a substitute of MPPT algorithms. The power converters implementing the MPPT algorithms generally modify the DC voltage and measure the DC current continuously, thus perturbing the voltage and current supplied by the PV generator. If the simulation model was proved to be reliable in a continuous way, it could be used to detect the MPP which could be then reached without introducing continuous disturbances in the DC currents and voltages.

- The Sixth Chapter introduced the analysis of the effect of partial shading caused by clouds on various configurations of PV generators as an additional topic of this thesis. However, it would be most interesting to undertake further research in this line and, for instance, compare the results obtained with the mismatch loses caused by shadows created by static objects to benchmark the edge effects of the moving clouds.

REFERENCES

Abbott, D. (2010). Keeping the energy debate clean: How do we supply the world's energy needs?, *Proceedings of the IEEE* **98**(1): 42–66.

Alonso-García, M. C., Ruíz, J. M. and Chenlo, F. (2006). Experimental study of mismatch and shading effects in the I-V characteristic of a photovoltaic module, *Solar Energy Materials and Solar Cells* **90**(3): 329–340.

Armstrong, S. and Hurley, W. (2010). A thermal model for photovoltaic panels under varying atmospheric conditions, *Applied Thermal Engineering* **30**(11-12): 1488–1495.

Aurenhammer, F. (1991). Voronoi diagrams - a survey of a fundamental geometric data structure, *ACM Comput. Surv.* **23**(3): 345–405.

Balog, R., Kuai, Y. and Uhrhan, G. (2009). A photovoltaic module thermal model using observed insolation and meteorological data to support a long life, highly reliable module-integrated inverter design by predicting expected operating temperature, *IEEE Energy Conversion Congress and Exposition, 2009. ECCE 2009*, pp. 3343–3349.

Barroso, L.-A., Rudnick, H., Sensfuss, F. and Linares, P. (2010). The green effect, *IEEE Power and Energy Magazine* **8**(5): 22–35.

Blair, N. J. and Dobos, A. P. (2013). Comparison of photovoltaic models in the system advisor model, *Solar 2013*, National Renewable Energy Laboratory, Baltimore, Maryland.

Bosch, J. L., Zheng, Y. and Kleissl, J. (2013). Deriving cloud velocity from an array of solar radiation measurements, *Solar Energy* **87**: 196–203.

Bose, B. (2010). Global warming: Energy, environmental pollution, and the impact of power electronics, *IEEE Industrial Electronics Magazine* **4**(1): 6–17.

Bull, S. (2001). Renewable energy today and tomorrow, *Proceedings of the IEEE* **89**(8): 1216–1226.

Burger, B. and Rüther, R. (2006). Inverter sizing of grid-connected photovoltaic systems in the light of local solar resource distribution characteristics and temperature, *Solar Energy* **80**(1): 32–45.

Carrero, C., Amador, J. and Arnaltes, S. (2007). A single procedure for helping PV designers to select silicon PV modules and evaluate the loss resistances, *Renewable Energy* **32**(15): 2579–2589.

Chamberlin, C. E., Lehman, P., Zoellick, J. and Pauletto, G. (1995). Effects of mismatch losses in photovoltaic arrays, *Solar Energy* **54**(3): 165–171.

Chapin, D. M., Fuller, C. S. and Pearson, G. L. (1954). A new silicon p-n junction photocell for converting solar radiation into electrical power, *Journal of Applied Physics* **25**(5): 676–677.

Chenni, R., Makhlouf, M., Kerbache, T. and Bouzid, A. (2007). A detailed modeling method for photovoltaic cells, *Energy* **32**(9): 1724–1730.

Cubas, J., Pindado, S. and Victoria, M. (2014). On the analytical approach for modeling photovoltaic systems behavior, *Journal of Power Sources* **247**: 467–474.

De Soto, W., Klein, S. A. and Beckman, W. A. (2006). Improvement and validation of a model for photovoltaic array performance, *Solar Energy* **80**(1): 78–88.

Dobos, A. P. (2012). An improved coefficient calculator for the california energy commission 6 parameter photovoltaic module model, *Journal of Solar Energy Engineering* **134**(2): 1–6.

Durisch, W., Bitnar, B., Mayor, J.-C., Kiess, H., Lam, K.-h. and Close, J. (2007). Efficiency model for photovoltaic modules and demonstration of its application to energy yield estimation, *Solar Energy Materials and Solar Cells* **91**(1): 79–84.

Eltawil, M. A. and Zhao, Z. (2010). Grid-connected photovoltaic power systems: technical and potential problems - a review, *Renewable and Sustainable Energy Reviews* **14**(1): 112–129.

Esram, T. and Chapman, P. (2007). Comparison of photovoltaic array maximum power point tracking techniques, *IEEE Transactions on Energy Conversion* **22**(2): 439–449.

European Photovoltaic Industry Association (2013). Global Market Outlook for Photovoltaics 2013-2017, *Technical report*, European Photovoltaic Industry Association (EPIA).

European Wind Energy Association (2013). Wind in power - European statistics 2012, *Technical report*, European Wind Energy Association (EWEA).

Feliciano-Cruz, L. and Ortiz-Rivera, E. (2012). Biharmonic spline interpolation for solar radiation mapping using puerto rico as a case of study, *2012 38th IEEE Photovoltaic Specialists Conference (PVSC)*, pp. 002913–002915.

Franghiadakis, Y. and Tzanetakis, P. (2006). Explicit empirical relation for the monthly average cell-temperature performance ratio of photovoltaic arrays, *Progress in Photovoltaics: Research and Applications* **14**(6): 541–551.

Fritts, C. (1883). On a new form of selenium photocell, *Proceedings of the American Association for the Advancement of Science*, p. 97.

Frost & Sullivan (2009). Global Solar Power Market, *Technical report*, Frost & Sullivan.

Galiana, B., Algora, C. and Rey-Stolle, I. (2008). Explanation for the dark i-v curve of III-V concentrator solar cells, *Progress in Photovoltaics* **16**(4): 331–338.

Gosh, K., Fishman, C. and Feng, T. (1980). Theory of the electrical and photovoltaic properties of polycrystalline silicon, *Journal of Applied Physics* **51**(1): 446–454.

Gow, J. and Manning, C. (1999). Development of a photovoltaic array model for use in power-electronics simulation studies, *Electric Power Applications, IEE Proceedings* **146**(2): 193–200.

Green, M., Emery, K., Hishikawa, Y., Warta, W. and Dunlop, E. (2013). Solar cell efficiency tables (version 41), *Progress in Photovoltaics: Research and Applications* **21**(1): 1–11.

Gueymard, C. A. (2004). The suns total and spectral irradiance for solar energy applications and solar radiation models, *Solar Energy* **1**(4): 423–453.

Häberlin, H. (2012). *Photovoltaics system design and practice*, John Wiley & Sons.

Hegazy, A. (2000). Comparative study of the performances of four photovoltaic/thermal solar air collectors, *Energy Conversion and Management* **41**(8): 861–881.

Holman, J. P. (2002). *Heat transfer*, McGraw-Hill, New York.

Incropera, F. P. (2007). *Fundamentals of heat and mass transfer*, John Wiley.

International Energy Agency (2013). Key World Energy Statistics 2013, *Technical report*, International Energy Agency (IEA).

International Panel of Climate Change (2013). Climate Change 2013: The Physical Science Basis, *Technical report*, International Panel of Climate Change (IPCC).

Jones, A. D. and Underwood, C. P. (2001). A thermal model for photovoltaic systems, *Solar Energy* **70**(4): 349–359.

Kazmerski, L. L. (2006). Solar photovoltaics R&D at the tipping point: A 2005 technology overview, *Journal of Electron Spectroscopy and Related Phenomena* **150**(23): 105–135.

Kjaer, S., Pedersen, J. and Blaabjerg, F. (2005). A review of single-phase grid-connected inverters for photovoltaic modules, *IEEE Transactions on Industry Applications* **41**(5): 1292–1306.

Kopp, G. and Lean, J. L. (2011). A new, lower value of total solar irradiance: Evidence and climate significance, *Geophysical Research Letters* **38**(1): 1.

Krauter, S. C. W. (2004). Development of an integrated solar home system, *Solar Energy Materials and Solar Cells* **82**(1): 119–130.

Kroposki, B. and Margolis, R. (2009). Harnessing the sun: An overview of solar technologies, *IEEE Power and Energy Magazine* **7**(3, May/June 2009).

Kudish, A. I., Evseev, E. G., Walter, G. and Leukefeld, T. (2002). Simulation study of a solar collector with a selectively coated polymeric double walled absorber plate, *Energy Conversion and Management* **43**(5): 651–671.

Lashway, C. (1988). Photovoltaic system testing techniques and results, *IEEE Transactions on Energy Conversion* **3**(3): 503–506.

Laudani, A., Mancilla-David, F., Riganti-Fulginei, F. and Salvini, A. (2013). Reduced-form of the photovoltaic five-parameter model for efficient computation of parameters, *Solar Energy* **97**: 122–127.

Li, Y., Huang, W., Huang, H., Hewitt, C., Chen, Y., Fang, G. and Carroll, D. L. (2013). Evaluation of methods to extract parameters from current-voltage characteristics of solar cells, *Solar Energy* **90**: 51–57.

Liserre, M. and Sauter, T. (2010). Future energy systems: Integrating renewable energy sources into the smart power grid through industrial electronics, *Industrial Electronics Magazine, IEEE* **1**(1): 18 – 37.

Liu, S. and Dougal, R. (2002). Dynamic multiphysics model for solar array, *IEEE Transactions on Energy Conversion* **17**(2): 285–294.

Lo Brano, V., Orioli, A., Ciulla, G. and Di Gangi, A. (2010). An improved five-parameter model for photovoltaic modules, *Solar Energy Materials and Solar Cells* **94**(8): 1358–1370.

Luque, A. and Hegedus, S. (2011). *Handbook of photovoltaic science and engineering*, Wiley, Chichester, West Sussex, U.K.

Malik, A. Q. and Damit, S. J. B. H. (2003). Outdoor testing of single crystal silicon solar cells, *Renewable Energy* **28**(9): 1433–1445.

Masi, M., Fogliani, S. and Carra, S. (1999). Sensitivity analysis on indium phosphide liquid encapsulated czochralski growth, *Crystal Research and Technology* **34**(9): 1157–1167.

Mattei, M., Notton, G., Cristofari, C., Muselli, M. and Poggi, P. (2006). Calculation of the polycrystalline PV module temperature using a simple method of energy balance, *Renewable Energy* **31**(4): 553–567.

Mattick, C., Williams, E. and Allenby, B. (2010). Historical trends in global energy consumption, *IEEE Technology and Society Magazine* **29**(3): 22–30.

Mendoza, B. (2005). Total solar irradiance and climate, *Advances in Space Research* **35**(5): 882–890.

Mermoud, A. and Lejeune, T. (2010). Performance assessment of a simulation model for PV modules of any available technology, *2010 25th European Photovoltaic Solar Energy Conference (EUPVSEC)*, pp. 4786 – 4791.

Messenger, R. A. and Ventre, J. (2003). *Photovoltaic Systems Engineering, Second Edition*, CRC Press.

Mäki, A. (2013). *Effects of Partial Shading Conditions on Maximum Power Points and Mismatch Losses in Silicon-Based Photovoltaic Power Generators*, PhD thesis, Tampere University of Technology.

Mäki, A. and Valkealahti, S. (2012a). Mismatch losses in photovoltaic power generators due to partial shading caused by moving clouds, *Proceedings of 27th European Photovoltaic Solar Energy Conference and Exhibition*, Frankfurt, pp. 3911 – 3915.

Mäki, A. and Valkealahti, S. (2012b). Power losses in long string and parallel-connected short strings of series-connected silicon-based photovoltaic modules due to partial shading conditions, *IEEE Transactions on Energy Conversion* **27**(1): 173–183.

Mäki, A., Valkealahti, S. and Leppäaho, J. (2012). Operation of series-connected silicon-based photovoltaic modules under partial shading conditions, *Progress in Photovoltaics: Research and Applications* **20**(3): 298–309.

Nagae, S., Toda, M., Minemoto, T., Takakura, H. and Hamakawa, Y. (2006). Evaluation of the impact of solar spectrum and temperature variations on output power of silicon-based photovoltaic modules, *Solar Energy Materials and Solar Cells* **90**(20): 3568–3575.

National Renewable Energy Laboratory (2012). 2012 Renewable Energy Data Book, *Technical report*, National Renewable Energy Laboratory (NREL).

National Renewable Energy Laboratory (2013). Best research cell efficiencies (accessed on 7.2.2014).
URL: *http://www.nrel.gov/ncpv/images/efficiency_chart.jpg*

Nema, R., Nema, S. and Agnihotri, G. (2009). Computer simulation based study of photovoltaic Cells/Modules and their experimental verification, *International Journal of Recent Trends in Engineering (IJRTE)* **1**(Issue on Electrical & Electronics): 151–156.

Newton, J. (1989). *Uncommon Friends: Life with Thomas Edison, Henry Ford, Harvey Firestone, Alexis Carrel, and Charles Lindbergh*, 1st Harvest/HBJ edn, Mariner Books, San Diego, California, p. 31.

Nishioka, K., Sakitani, N., Uraoka, Y. and Fuyuki, T. (2007). Analysis of multicrystalline silicon solar cells by modified 3-diode equivalent circuit model taking leakage current through periphery into consideration, *Solar Energy Materials and Solar Cells* **91**(13): 1222–1227.

Nordmann, T. and Clavadetscher, L. (2003). Understanding temperature effects on PV system performance, *Proceedings of 3rd World Conference on Photovoltaic Energy Conversion, 2003*, Vol. 3, pp. 2243–2246 Vol.3.

Notton, G., Cristofari, C., Mattei, M. and Poggi, P. (2005). Modelling of a double-glass photovoltaic module using finite differences, *Applied Thermal Engineering* **25**(17-18): 2854–2877.

Nousiainen, L., Puukko, J., Mäki, A., Messo, T., Huusari, J., Jokipii, J., Viinamaäki, J., Torres Lobera, D., Valkealahti, S. and Suntio, T. (2013). Photovoltaic generator as an input source for power electronic converters, *IEEE Transactions on Power Electronics* **28**(6): 3028–3038.

Petrone, G., Spagnuolo, G., Teodorescu, R., Veerachary, M. and Vitelli, M. (2008). Reliability issues in photovoltaic power processing systems, *IEEE Transactions on Industrial Electronics* **55**(7): 2569–2580.

Renewable Energy Policy Network for the 21st Century (2013). Renewables 2013: Global status report, *Technical report*, Renewable Energy Policy Network for the 21st Century (REN21).

Sandrolini, L., Artioli, M. and Reggiani, U. (2010). Numerical method for the extraction of photovoltaic module double-diode model parameters through cluster analysis, *Applied Energy* **87**(2): 442–451.

Schott, T. (1985). Operation temperatures of PV modules, *Proceedings of 6th European Photovoltaic Energy Conference*, London, pp. 392–396.

Schroder, D. K. (1998). *Semiconductor Material and Device Characterization*, John Wiley & Sons Inc.

Servant, J. (1985). Calculation of the cell temperature for photovoltaic modules from climatic data, *Proceedings of the 9th biennal congress of ISES-Intersol*, Vol. 370, Montreal.

Shmilovitz, D. and Singer, S. (2002). Interfacing photovoltaic panels via a capacitive converter, *The 22nd Convention of Electrical and Electronics Engineers in Israel, 2002*, pp. 160–162.

Shockley, W. (1949). The theory of p-n junctions in semiconductors and p-n junction transistors, *Bell System Technical Journal* **28**(3): 435–489.

Shockley, W., Sparks, M. and Teal, G. (1951). p-n junction transistors, *Physical Review* **83**(1): 151–162.

Siddiqui, M. U., Arif, A. F. M., Bilton, A. M., Dubowsky, S. and Elshafei, M. (2013). An improved electric circuit model for photovoltaic modules based on sensitivity analysis, *Solar Energy* **90**: 29–42.

Silvestre, S., Boronat, A. and Chouder, A. (2009). Study of bypass diodes configuration on PV modules, *Applied Energy* **86**(9): 1632–1640.

Skoplaki, E., Boudouvis, A. G. and Palyvos, J. A. (2008). A simple correlation for the operating temperature of photovoltaic modules of arbitrary mounting, *Solar Energy Materials and Solar Cells* **92**(11): 1393–1402.

Skoplaki, E. and Palyvos, J. A. (2009). Operating temperature of photovoltaic modules: A survey of pertinent correlations, *Renewable Energy* **34**(1): 23–29.

Sparrow, E. M. and Tien, K. K. (1977). Forced convection heat transfer at an inclined and yawed square plate-application to solar collectors, *Journal of Heat Transfer* **99**(4): 507–512.

Swinbank, W. C. (1963). Long-wave radiation from clear skies, *Quarterly Journal of the Royal Meteorological Society* **89**(381): 339–348.

Teodorescu, R., Liserre, M. and Rodríguez, P. (2011). *Grid converters for photovoltaic and wind power systems*, Wiley & Sons.

Topic, M., Brecl, K. and Sites, J. (2007). Effective efficiency of PV modules under field conditions, *Progress in Photovoltaics: Research and Applications* **15**(1): 19–26.

Torres Lobera, D. (2011). *Measuring actual operating conditions of a photovoltaic power generator*, Master's thesis, Tampere University of Technology.

Torres Lobera, D., Mäki, A., Huusari, J., Lappalainen, K., Suntio, T. and Valkealahti, S. (2013). Operation of TUT solar PV power station research plant under partial shading caused by snow and buildings, *International Journal of Photoenergy* **2013**.

Torres Lobera, D. and Valkealahti, S. (2012). Operation of TUT solar photovoltaic power station research plant equipped with climatic and electric measuring systems, *Proceedings of 27th European Photovoltaic Solar Energy Conference and Exhibition*, Frankfurt, Germany, pp. 3905 – 3910.

Torres Lobera, D. and Valkealahti, S. (2013a). Dynamic thermal model of solar PV systems under varying climatic conditions, *Solar Energy* **93**: 183–194.

Torres Lobera, D. and Valkealahti, S. (2013b). Mismatch losses in PV power generators caused by partial shading due to clouds, *Proceedings of 4th IEEE International Symposium on Power Electronics for Distributed Generation Systems (PEDG)*, Rogers, Ar, USA, pp. 1–7.

Torres Lobera, D. and Valkealahti, S. (2013c). Spatial irradiance distribution map for a PV power plant derived from solar radiation measurements, *Proceedings of 28th European Photovoltaic Solar Energy Conference and Exhibition*, Paris, France, pp. 3666 – 3672.

Torres Lobera, D. and Valkealahti, S. (2014a). Inclusive dynamic thermal and electric simulation model of solar pv systems under varying atmospheric conditions, *Solar Energy* **105**: 632–647.

Torres Lobera, D. and Valkealahti, S. (2014b). Optimizing the accuracy of electrical models of pv systems operating under non-ideal conditions, *Proceedings of 16th Conference on Power Electronics and Applications, (EPE'14-ECCE Europe)*, Lappeenranta, Finland. In press.

Torres Lobera, D. and Valkealahti, S. (2014c). Validation of an inclusive dynamic-thermal and electric simulation model for PV systems with measurements from a commercial grid-connected PV inverter, *Proceedings of 29th European Photovoltaic Solar Energy Conference and Exhibition*, Amsterdam, Netherlands. Accepted.

Tsai, H.-F. and Tsai, H.-L. (2012). Implementation and verification of integrated thermal and electrical models for commercial PV modules, *Solar Energy* **86**(1): 654–665.

Ubisse, A. and Sebitosi, A. (2009). A new topology to mitigate the effect of shading for small photovoltaic installations in rural sub-saharan africa, *Energy Conversion and Management* **50**(7): 1797–1801.

U.S. Energy Information Administration (2013). International Energy Outlook 2013, *Technical report*, U.S. Energy Information Administration (EIA).

Valkealahti, S. (2011). Forecasting the future of renewables, *in* H. Kheradmand (ed.), *Climate Change - Socioeconomic Effects*, InTech.

Villalva, M., Gazoli, J. and Filho, E. (2009a). Comprehensive approach to modeling and simulation of photovoltaic arrays, *IEEE Transactions on Power Electronics* **24**(5): 1198–1208.

Villalva, M., Gazoli, J. and Filho, E. (2009b). Modeling and circuit-based simulation of photovoltaic arrays, *Power Electronics Conference, 2009. COBEP '09. Brazilian*, pp. 1244–1254.

Walker, G. R. (2001). Evaluating MPPT converter topologies using a matlab PV model, *Journal of Electrical & Electronics Engineering, Australia* **21**(1): 49–55.

Weast (1984). *Handbook of Chemistry and Physics {64th Edition - 1983-1984}*, 64$^{\text{th}}$ edn, CRC Press.

Weigl, T., Nagl, L., Weizenbeck, J., Zehner, M., Augel, M., Giesler, B., Becker, G., Mayer, O., Betts, T. and Gottschalg, R. (2012). Modelling and validation of spatial irradiance characteristics for localised irradiance fluctuations and enhancements, *Proceedings of 27th European Photovoltaic Solar Energy Conference and Exhibition*, Frankfurt, pp. 3801 – 3804.

Wenham, S. R. (2007). *Applied photovoltaics*, Earthscan, London.

Wenham, S. R. and Green, M. A. (1996). Silicon solar cells, *Progress in Photovoltaics: Research and Applications* **4**(1): 3–33.

Wong, L. T. and Chow, W. K. (2001). Solar radiation model, *Applied Energy* **69**(3): 191–224.

World Energy Council (2013). World Energy Resources - 2013 Survey, *Technical report*, World Energy Council (WEC).

World Meteorological Organization (2008). *WMO-8 (Guide to Meteorological Instruments and Methods of Observation)*.

Tampereen teknillinen yliopisto
PL 527
33101 Tampere

Tampere University of Technology
P.O.B. 527
FI-33101 Tampere, Finland

ISBN 978-952-15-3366-2
ISSN 1459-2045